NUMERICAL MODELING OF DIRECT CARBON SOLID OXIDE CELLS

HAORAN XU

PhD

The Hong Kong Polytechnic University

2018

The Hong Kong Polytechnic University

Department of Building and Real Estate

Numerical Modeling of Direct Carbon Solid Oxide Cells

Haoran XU

A thesis submitted in partial fulfillment of the requirements for the degree of

Doctor of Philosophy

February 2018

CERTIFICATE OF ORGINALITY

I hereby declare that this thesis is my own work and that, to the best of my knowledge and belief, it reproduces no material previously published or written, nor material that has been accepted for the award of any other degree or diploma, except where due acknowledgement has been made in the text.

_____   __________ (Signed)

_________Haoran XU__________ (Name of student)

ABSTRACT

Solid oxide cells (SOCs) are promising devices for clean energy utilization with high efficiency. A solid oxide cell has a good reversible working mode characteristic. It can work either as a solid oxide fuel cell (SOFC) to generate electrical power from fuels or as a solid oxide electrolysis cell (SOEC) for utilizing excessive renewable power to generate fuels. The SOC is environmentally friendly and has high efficiency in converting energy between fuels and electrical power, which makes it a promising next-generation device in utilizing traditional fossil fuels such as solid carbon.

In this work, 2D numerical models are developed for CO and electricity co-generation in direct carbon solid oxide fuel cells (DC-SOFCs). The model is validated by comparing the simulation results with experimental data from the literature. Parametric simulations are conducted to understand the physical/chemical processes in DC-SOFCs. Good performance of DC-SOFC is achievable even at a large distance between the carbon bed and the porous anode, indicating the feasibility of large-scale DC-SOFC applications. The DC-SOFC performance is found to decrease with decreasing temperature due to the decreased Boudouard reaction kinetics. The molar fraction of CO at the anode can be well controlled by adjusting the operating conditions of DC-SOFC, enabling electricity and CO co-generation. Another finding is that the current density in the DC-SOFC increases slightly along the cell length, which is different from that in the H_2-fueled SOFC. The anode-supported configuration is found to be beneficial in improving the electrical output of the DC-SOFC but is unfavorable for CO generation.

By considering heat transfer effects, parametric simulations are also conducted to investigate the effects of various operating and structural parameters on the thermal behaviors of DC-SOFCs. It is found that the operating parameters greatly influence the DC-SOFC thermal behaviors and the temperature field in DC-SOFC is highly non-uniform. The position of peak temperature in the cell is highly dependent on the operating potential. In addition, it is found that a smaller distance between the carbon bed and the anode electrode is beneficial for improving the temperature uniformity in the DC-SOFC. The breakdown of heat generation/consumption in DC-SOFC shows that the anode processes contribute the most to the temperature variation in the cell.

Different from conventional DC-SOFC with CO_2 as gasification agent, a new DC-SOFC using H_2O as gasification agent is proposed and studied systematically by both experiment and simulation. The performance of DC-SOFCs with two agents are compared at different operating potential, temperature and anode inlet gas flow rate. It is found that the H_2O-assisted DC-SOFC significantly outperform the CO_2-assisted DC-SOFC. The higher performance of H_2O-assisted DC-SOFC comes from: (1) higher H_2O-carbon gasification kinetics and (2) lower activation loss of H_2 electrochemical oxidation. It is also found that a higher temperature could greatly improve the performance of both kinds of DC-SOFCs. At a temperature of 1000K and operating voltage of 0.5 V, the current density from the CO_2-assisted DC-SOFC is close to 0 while it is still above 1000 A m^{-2} from the H_2O-assisted DC-SOFC, allowing the operation of H_2O assisted DC-SOFC at reduced temperature. It is found that the anode gas flow rate does not significantly affect the performance of DC-SOFC.

To further improve the performance of H_2O assisted DC-SOFCs, Na_2CO_3 is added in solid carbon for enhancing carbon gasification kinetics. The performance of DC-SOFCs with and without catalyst are compared at different operating potential, anode inlet gas flow rate and operating temperature. It is found that adding suitable catalyst can significantly speed up the in-situ steam-carbon gasification reaction and improve the performance of DC-SOFC. The potential of syngas and electricity co-generation from the fuel cell is also evaluated, where the composition of H_2 and CO in syngas can be adjusted by controlling the anode inlet gas flow rate. In addition, the performance DC-SOFCs and the percentage of fuel in the outlet gas are both increased with increasing operating temperature.

Lastly, carbon assisted solid oxide electrolysis cell (CA-SOEC) for H_2O electrolysis is proposed for syngas production with easy control of H_2/CO ratio. 2D numerical models are developed to study the effects of operating and design parameters on the CA-SOEC performance. One important finding is that the carbon assisting is effective in lowering the equilibrium potential of SOEC, thus greatly reduces the electrical power consumption for H_2O electrolysis. The CA-SOEC can generate electrical power, CO and H_2 simultaneously at a low current density and sufficiently high temperature. Compared with conventional SOEC for H_2O/CO_2 co-electrolysis, CA-SOEC is advantageous as CO and H_2 are produced in the anode and cathode, respectively. This enables easy control of H_2/CO ratio, which is helpful for subsequent processes to synthesis other chemicals or fuels from syngas. Besides, CA-SOEC can produce electricity rather than consuming it. The model can be used for subsequent design optimization of CA-SOEC for effective energy storage and conversion.

The results of this study form a solid foundation for better understanding the chemical/physical processes in DC-SOFCs and CA-SOECs with different kinds of operating conditions. The models can be used for subsequent design optimization of DC-SOFCs and CA-SOECs at a system level for thermal management and effective energy storage and conversion.

PUBLICATIONS

[1] **Xu H**, Chen B, Irvine J, Ni M. Modeling of CH4-assisted SOEC for H2O/CO2 co-electrolysis. International Journal of Hydrogen Energy. 2016;41:21839-49.

[2] **Xu H**, Chen B, Liu J, Ni M. Modeling of direct carbon solid oxide fuel cell for CO and electricity cogeneration. Applied Energy. 2016;178:353-62.

[3] **Xu H**, Chen B, Ni M. Modeling of Direct Carbon-Assisted Solid Oxide Electrolysis Cell (SOEC) for Syngas Production at Two Different Electrodes. J Electrochem Soc. 2016;163:F3029-F35.

[4] **Xu H**, Chen B, Zhang H, Kong W, Liang B, Ni M. The thermal effect in direct carbon solid oxide fuel cells. Applied Thermal Engineering. 2017;118:652-62.

[5] **Xu H**, Chen B, Zhang H, Sun Q, Yang G, Ni M. Modeling of direct carbon solid oxide fuel cells with H2O and CO2 as gasification agents. International Journal of Hydrogen Energy. 2017;42:15641-51.

[6] **Xu H**, Chen B, Zhang H, Tan P, Yang G, Irvine JTS, et al. Experimental and modeling study of high performance direct carbon solid oxide fuel cell with in situ catalytic steam-carbon gasification reaction. Journal of Power Sources. 2018;382:135-43.

[7] **Xu H**, Chen B, Tan P, Cai W, He W, Farrusseng D, et al. Modeling of all porous solid oxide fuel cells. Applied Energy. 2018;219:105-13.

[8] **Xu H**, Chen B, Tan P, Zhang H, Yuan J, Liu J, et al. Performance improvement of a direct carbon solid oxide fuel cell system by combining with a Stirling cycle. Energy. 2017;140:979-87.

[9] **Xu H**, Chen B, Tan P, Zhang H, Yuan J, Irvine JTS, et al. Performance improvement of a direct carbon solid oxide fuel cell through integrating an Otto heat engine. Energy Conversion and Management. 2018;165:761-70.

[10] Chen B, **Xu H**, Chen L, Li Y, Xia C, Ni M. Modelling of One-Step Methanation Process Combining SOECs and Fischer-Tropsch-like Reactor. J Electrochem Soc. 2016;163:F3001-F8.

[11] Chen B, **Xu H**, Ni M. Modelling of finger-like channelled anode support for SOFCs application. Science Bulletin. 2016:1-9.

[12] Chen B, **Xu H**, Ni M. Modelling of SOEC-FT reactor: Pressure effects on methanation process. Applied Energy. 2017;185, Part 1:814-24.

[13] Chen B, **Xu H**, Zhang H, Tan P, Cai W, Ni M. A novel design of solid oxide electrolyser integrated with magnesium hydride bed for hydrogen generation and storage – A dynamic simulation study. Applied Energy. 2017;200:260-72.

[14] Tan P, Chen B, **Xu H**, Zhang H, Cai W, Ni M, et al. Flexible Zn- and Li-Air Batteries: Recent Advances, Challenges, and Future Perspectives. Energy & Environmental Science. 2017.

[15] Zhang H, Chen B, **Xu H**, Ni M. Thermodynamic assessment of an integrated molten carbonate fuel cell and absorption refrigerator hybrid system for combined power and cooling applications. International Journal of Refrigeration. 2016;70:1-12.

[16] Zhang H, Kong W, Dong F, **Xu H**, Chen B, Ni M. Application of cascading thermoelectric generator and cooler for waste heat recovery from solid oxide fuel cells. Energy Conversion and Management. 2017;148:1382-90.

[17] Zhang H, **Xu H**, Chen B, Dong F, Ni M. Two-stage thermoelectric generators for waste heat recovery from solid oxide fuel cells. Energy. 2017;132:280-8.

[18] Zhang X, Ni M, Dong F, He W, Chen B, **Xu H**. Thermodynamic analysis and performance optimization of solid oxide fuel cell and refrigerator hybrid system based on H2 and CO. Applied Thermal Engineering. 2016;108:347-52.

[19] Tan P, Chen B, **Xu H**, Cai W, He W, Liu M, et al. Co3O4 Nanosheets as Active Material for Hybrid Zn Batteries. Small.(accepted)

[20] Cai W, Liu J, Liu P, Liu Z, **Xu H**, Chen B, et al. A direct carbon solid oxide fuel cell fueled with char from wheat straw. International Journal of Energy Research. (accepted)

ACKNOWLEDGEMENTS

First and foremost, I would like to express my special appreciation and thanks to my PhD supervisor Prof. Meng NI for his guidance, encouragement, and patience. Throughout my time at The Hong Kong Polytechnic University, his immense and extensive knowledge amazed me and his enthusiasm on scientific research, rigorous scholarship, and genial personality deeply infected and inspired me. I do appreciate that he has offered countless helpful suggestions for my research work and instructed and helped me on writing papers and this thesis. I am extremely fortune and grateful to have Prof. NI as my supervisor.

Furthermore, my sincere gratitude goes to our university, our department and Research Office for their generous and consistent support during my PhD study.

I would also like to thank all our group members, Feifei DONG, Wei HE, Qiong SUN, Keqing ZHENG, Meiling LI, Bin CHEN, Ruixiaoxiao ZHANG, Houcheng ZHANG, Peng TAN, Weizi CAI, Wei Kong, Zhen WU and Ronghua YUAN. The discussion with them is full of wisdom and inspiration.

Thanks to Prof. Yixiang SHI, Dr. Yu LUO, Dr. Yuqing WANG, Dr. Wenyin LI, Dr. Yi YANG, Dr. Tianyu CAO, Dr. Xi WANG in Tsinghua University, their kind help leaves me a nice memory in Beijing.

Thanks to Prof. Jiang LIU in South China University of Technology, her suggestions on my research topic give me a lot of help.

Thanks to Prof. Zongping SHAO, Prof. Wei ZHOU, Dr. Guangming YANG, Dr. Jifa QU, Dr. Qian LIN, Mr. Ye HU, Mr. Yufei SONG, Mr Chuan ZHOU, Miss Yuan ZHANG, Mr. Shiyong CHU, and Miss Jie YU in Nanjing Tech University. My experiments on direct carbon solid oxide fuel cells would not be finished so successfully without them.

Thanks to Prof. John TS Irvine in University of St Andrews, his kind help offers me a great chance to enjoy a beautiful and fruitful summer in year 2017.

Thanks to Prof. David Farrusseng in IRCELYON and Prof. Youmin GUO in Anhui University, their kind suggestions on the modeling of all porous solid oxide fuel cells helps me a lot.

In my time at PolyU, I met a lot of new friends and I am grateful to their help and support. Thank Xiaopu LV, Shang GAO, Xin ZHOU, Yuhao XIONG, Ming LUO, Ke FAN, Junjie ZENG, Xiao YANG, Yangzong ZEREN, Sandra and Qingyang ZHAO.

Also thank my old friends Yujing LUO, Rui CHENG, Han YU, Xuemei LING, Yunshang SONG, Cheng ZHANG, Enjie YU, Yanye CHEN, Zixuan LI, Yichen LIU, Dan HAN, Chengnan LIU, Xuanyu HE, Zhoujie FU, Bingbing CHEN, Miaoming ZHOU and Qiuyu SHI, your support and company is always important to me.

Special thanks to Zhen YAO, thank you for your effort on polishing my manuscripts and your understanding and company for all the time. I hope you will enjoy writing your PhD dissertation in the future.

Last but not the least, I would like to express my deepest gratitude to my parents Caiping WANG and Yinlong XU, my sister Miaoyi XU for their unconditional and unselfish love, constant concern, and persistent support. I do appreciate that my family always offers me helpful advices, positive energy, and courage to overcome obstacles. This thesis is dedicated to my family.

TABLE OF CONTENTS

LIST OF FIGURES

LIST OF TABLES

LIST OF ABBREVIATIONS

Ag-GDC	The mixture of silver and GDC
CA-SOEC	Carbon assisted solid oxide electrolysis cell
CHP	Combined heat and power
DC-SOFC	Solid oxide fuel cell direct using carbon as fuel
FA-SOEC	Fuel assisted solid oxide electrolysis cell
GDC	Gadolinium doped ceria, $Ce_{0.8}Gd_{0.2}O_{1.9}$
GD-SOFC	Gasification-driven direct carbon fuel cell
H_2-SOFC	Solid oxide fuel cell using H_2 as fuel
LSCF	Lanthanum strontium cobalt ferrite
N-S	Navier-Stokes
Ni-YSZ	mixture of YSZ (yttrium stabilized zirconium) and nickel
PEN	Positive Electrode-Electrolyte-Negative electrode assembly
SCCM	Standard cubic centime per minute
SDC	Samaria-doped ceria
SOEC	Solid oxide electrolysis cell
SOFC	Solid oxide fuel cell
TPB	Triple phase boundary
WGSR	Water gas shift reaction
YSZ	Yttrium stabilized zirconium

Roman

$\boldsymbol{B_0}$	Permeability coefficient, m^2
$\boldsymbol{c_{CO_2}}$	Molar concentration of carbon dioxide, $mol \cdot m^{-3}$

c_{H_2O}	Mole concentration of water, mol·m^{-3}
C_p	Heat capacity, J·K^{-1}
D_{ce}	Distance between carbon and anode electrode
D_i^{eff}	Effective diffusivity of species i , m^2·s^{-1}
D_{ik}^{eff}	Knudsen diffusion coefficient of i , m^2·s^{-1}
D_{im}^{eff}	Molecular diffusion coefficient of i, m^2·s^{-1}
E_{act}	Activation energy, J·mol^{-1}
E_{br}	Active energy of reversed Boudouard reaction, J·mol^{-1}
E_{CO}	Equilibrium potential for carbon monoxide oxidization, V
E_{CO}^0	Standard equilibrium potential for carbon monoxide oxidization, V
E_{eq}	Equilibrium Nernst potential, V
E_{H_2}	Equilibrium potential for hydrogen oxidization, V
$E_{H_2}^0$	Standard equilibrium potential for hydrogen oxidization, V
E_{OCV}	Reversible open circuit voltage, V
F	Faraday constant, 96485 C·mol^{-1}
i	Current density, A·m^{-2}
I	Current, A
i_o	Exchange current density, A·m^{-2}
k	Reaction rate constant, in terms of m, mol, Pa and s
K_{br}	Equilibrium constant of Boudouard reaction
L_{cell}	Length of the cell, mm
n	Number of electrons transferred per electrochemical reaction
N_i	Flux of mass transport, kg·m^{-3}·s^{-1}
p	(partial) Pressure, Pa

Q	Heat source, J
$\boldsymbol{R}$	Gas constant, 8.314 J·mol^{-1}·K^{-1}
$\boldsymbol{R_{C\_CO2}}$	Reaction rate of Boudouard reaction, mol·m^{-3}·s^{-1}
$\boldsymbol{R_{C\_H2O}}$	Reaction rate of steam-carbon gasification, mol·m^{-3}·s^{-1}
$\boldsymbol{R_{ce}}$	Ratio of D_{ce} to cell length
$\boldsymbol{R_{WGSR}}$	Reaction rate of water gas shift reaction, mol·m^{-3}·s^{-1}
T	Temperature, K
$\mathbf{u}$	Velocity field, m^3·s^{-1}
v	Volume fraction
V	Voltage, V
$\boldsymbol{y_i}$	Molar fraction of component i

Greek letters

$\boldsymbol{\alpha}$	Charge transfer coefficient
$\boldsymbol{\beta_{H_2}}$	Electrochemical kinetics parameter for H_2
$\boldsymbol{\varepsilon}$	Porosity
$\boldsymbol{\eta_{act}}$	Anode activation polarization, V
$\boldsymbol{\eta_{act,an}}$	Anode activation polarization, V
$\boldsymbol{\eta_{act,ca}}$	Cathode activation polarization, V
$\boldsymbol{\eta_{con}}$	Concentration overpotential, V
$\boldsymbol{\eta_{ohmic}}$	Ohmic polarization, V
$\boldsymbol{\kappa}$	Permeability, m^2
$\boldsymbol{\lambda}$	Thermal conductivity, W·m^{-1}K^{-1}
$\boldsymbol{\mu}$	Dynamic viscosity of fluid, Pa·s

ρ	Fluid density, kg·m^{-3}
σ	Conductivity, S/m
τ	Tortuosity
$\emptyset$	Potential, V

Subscripts

an	Anode
ca	Cathode
co	Carbon monoxide
H_2	Hydrogen
l	Ionic phase
s	Electronic phase

Superscripts

0	Parameter at equilibrium conditions
eff	Effective
L	Local

1. CHAPTER 1 INTRODUCTION

1.1 Background

Growing concern on energy crisis and environmental problems has driven worldwide research attention into clean and high efficiency energy technologies. Although the contribution from renewable solar and wind energy is increasing, fossil fuels are still the major energy source and will continue to be the dominating energy source for the coming decades[1-6].

Solid carbon is the major component of fossil fuels. It can also be obtained easily from cheap and renewable biomasses such as waste wood and leaves. Compared with other fossil fuels, solid carbon such as coal has the characteristics of high energy density, abundant in storage and cheap price. However, solid carbon fuels are usually used in conventional thermal power plants which will produce significant amount of pollutants and hazardous gases such as CO_2, SO_x and NO_x as byproduct [7-9]. In addition, the efficiency of power generation by thermal power plant is typically below 40% due to the Carnot cycle limitation or even about 30% if carbon capture and storage is adopted to reduce the pollutant emission [10]. As carbon-based fuel will continue to be the major energy source for a long time, more efficient and environmentally friendly strategy using solid carbon fuel for power generation is of practical importance, such as solid oxide fuel cells (SOFCs) [11-15].

The SOFC is an electrochemical device which can convert the chemical energy of a fuel into electrical energy at an efficiency higher than that of a conventional thermal power plant[16-18]. It is a whole solid-state device with an oxygen-ion-conducting electrolyte being sandwiched between two porous electrodes. As the fuel and oxidant are separated by the dense electrolyte, emission control in SOFCs is relatively easy. As the operating temperature of SOFC is high (about 800°C), electrochemical reaction kinetics are fast, thus low-cost catalyst such as Ni can be used[19-25]. For comparison, low temperature fuel cells such as proton exchange membrane fuel cells (PEMFCs) usually need expensive noble-metal catalyst (i.e. Pt). In addition, SOFCs are fuel flexible and can use not only H_2, but also various hydrocarbon fuels, solid carbon, and ammonia for power generation [26-29].

Renewable energy such as solar energy or wind energy is also a promising solution to the energy crisis in the future. However, they are discrete in time and space, thus not reliable for continuous energy supply[30-36]. Therefore, effective energy storage and conversion technologies are critical for renewable energy applications to mitigate the mismatch between energy supply and demand. Moreover, the development of smart grid also needs effective energy storage and conversion devices, such as solid oxide electrolysis cells (SOECs)[37-39].

An SOEC is the solid oxide cell (SOC) working in a reversed mode of SOFC[40-42]. The SOEC is therefore a high temperature electrochemical cell suitable for converting excessive renewable power to fuels. The produced fuel can be stored and converted back into electrical power via fuel cells when the renewable power is insufficient[43-

47]. Compared with low temperature electrolyzers, the electricity requirement of SOEC is relatively lower as a significant part of total energy needed for SOEC is in the form of heat. In addition, the high operating temperature of SOEC enables the use of non-noble metal catalyst, leading to lower cost than low temperature electrolyzer systems[48-52].

1.2 Characteristics of SOCs

A typical fuel cell has two electrodes and one electrolyte as shown in Fig. 1.1(a). Fuels (H_2, CO) lose electrons to be oxidized in the anode. The electrons transfer through outside circuit to the cathode, where oxidants (O_2) are reduced. In this process, the chemical energy is converted to electrical energy directly with high efficiency. The produced gas (CO_2 and H_2O) are easy to be collected and post-processed, which also eases the environmental problems.

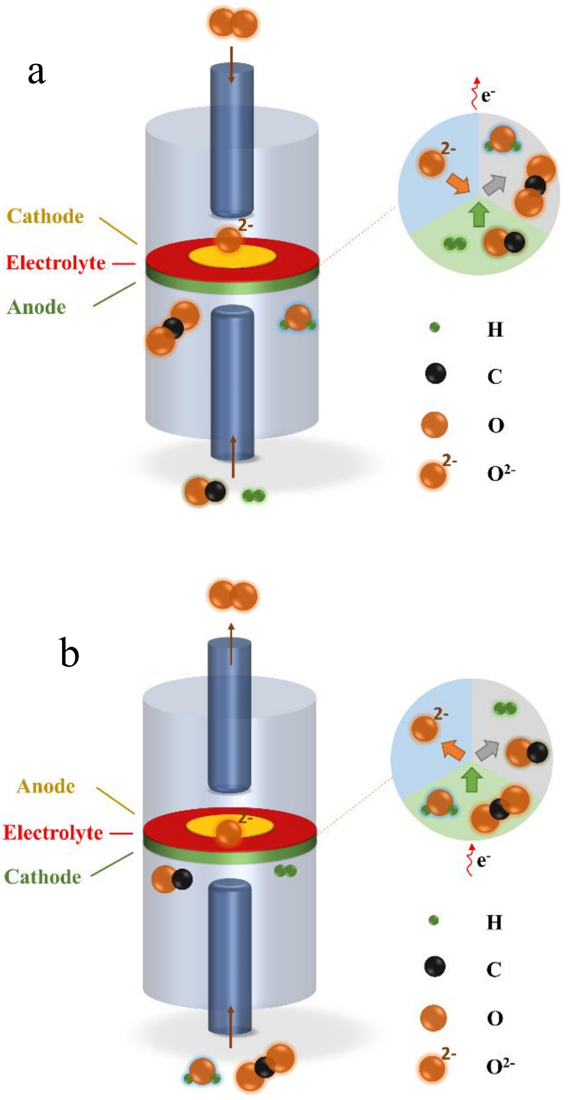

Figure 1.1 Schematic of a typical SOFC (a) and SOEC (b)

Fuel cells can be roughly separated into six kinds according to their different electrolytes as shown in Table 1.1. Different kinds of fuel cells have different operating temperature and transfers different kinds of ionic in electrolyte.

Table 1.1 Major types of fuel cells currently under development

	Operating Temperature (°C)	**Electrolyte**
PEMFC	60 – 120	PEM
DMFC	60 – 120	PEM
AFC	< 100	KOH
PAFC	160 – 220	H_3PO_4
MCFC	600 – 800	Molten Carbonate
SOFC	800 - 1000	O^{2-} conducting ceramic

Like an SOFC, an SOEC usually consists of two porous electrodes and one dense electrolyte. Porous electrodes provide transport paths (for ions, electrons and gases) and reaction sites for the electrochemical reactions, while the dense electrolyte separates the gases in different electrodes and allows oxygen ions transport from cathode to anode.

In a typical SOEC as shown in Fig. 1.1(b), cathode gas (H_2O/CO_2) transports from channel to triple phase boundary (TPB) reaction sites where they receive electrons to be reduced to H_2 and generate O^{2-} , which then transports from the cathode TPB sites to the anode TPB sites through the electrolyte to form O_2 and release electrons. The generated O_2 transport from anode TPB sites to anode gas channel, and the released electrons transport from anode TPB sites to cathode reaction sites through external electric circuit to form a complete circuit cycle.

1.2.1 Characteristics of SOFCs

An SOFC is a kind of fuel cell characterized by its solid electrolyte and high operating temperature. Compared with other kinds of fuel cells, SOFC has following characteristics [53-64]:

1) SOFC works at high temperature (commonly 1073 K~1273 K), which improves its electrochemical reaction rates, ion/electron conductivities and gas transport rates.

2) The high electrochemical reaction rate of SOFC allows the use of non-noble metal catalysts like Ni, which greatly decreases its cost.

3) CO is a poison to low temperature fuel cells but can be used as fuel in SOFC, which means hydrocarbon fuels and solid carbon can be used in SOFC. The use of hydrocarbon fuels and solid carbon separates SOFC from the hydrogen economy and makes it possible to be used in very near future with a low fuel cost.

4) The high-quality waste heat in SOFC can be used by combining other industry systems (such as combined heat and power system: CHP) with greatly enhanced system efficiency.

5) The whole solid structure makes the cell to be highly reliable, long life and quiet.

6) Emission control in SOFCs is relatively easy as the fuel and oxidant are separated by the dense electrolyte.

1.2.2 Characteristics of SOECs

Due to its excellent reversible working mode characteristic, an SOC can also be used to electrolyze oxidants like H_2O and CO_2 to generate H_2 and CO. The SOEC is a high temperature electrochemical cell suitable for converting excessive renewable power to fuels with following characteristics [65-72]:

1) Compared with traditional low temperature electrolysis methods, the electricity requirement of SOEC is relatively lower as a significant part of total energy needed for SOEC is in the form of heat.

2) The high operating temperature of SOEC enables the use of non-noble metal catalyst, leading to lower cost than low temperature electrolysis systems.

3) SOECs are capable of co-electrolyzing CO_2 and H_2O to produce syngas (H_2 and CO mixture), which can be further processed to gaseous or liquid fuels using Fischer-Tropsch reactor. This offers an alternative way of utilizing the captured CO_2 for fuel synthesis using excessive renewable power.

1.3 Principles of SOFCs

1.3.1 Thermodynamic mechanism

The output energy of an SOFC comes from the fuel chemical energy. The total amount of energy released from a reaction equals to the enthalpy change of the reaction. However, only part of the chemical energy can be converted into electric energy in an SOFC while the remaining part is released in the form of heat. For a reversible electrochemical reaction, the maximum electric power output is determined by the Gibbs free energy change of the reaction[73-77]. Therefore, the maximum conversion efficiency of fuel chemical energy to electric energy (i.e. thermodynamic efficiency) in an SOFC is:

$$\eta_{therom} = \frac{\Delta G}{\Delta H} \tag{1.1}$$

where ΔG and ΔH are the Gibbs free energy (J) change and enthalpy (J) change of a chemical reaction, respectively. The reversible open circuit voltage (OCV) of a fuel cell can be calculated as:

$$E_{ocv} = \frac{\Delta G}{nF} \tag{1.2}$$

where, E_{ocv} is the reversible open circuit voltage (V); n is the number of electrons transfers in one electrochemical reaction. F is the Faraday constant (96,485 C/mol). E_{ocv} of some typical reactions in fuel cells can be seen in Table 1.2.

Table 1.2 E_{ocv} of typical reactions at 25 °C and 980 °C

Reaction	$-\Delta G^0 (kJ\ mol^{-1})$	E_{ocv}	
		25 °C	980 °C
$H_2 + 0.5O_2 = H_2O$	55.64	1.19	0.97
$C + 0.5O_2 = CO$	32,81	0.71	1.16
$C + O_2 = CO_2$	94.26	1.02	1.03

$\boldsymbol{CO + 0.5O_2 = CO_2}$	61.45	1.33	0.90
$\boldsymbol{CH_4 + 2O_2 = CO_2 + 2H_2O}$	195.6	1.06	1.06

1.3.2 Electrochemical performance

The actual cell output voltage of the SOFC is usually lower than E_{OCV} due to various overpotential losses including activation overpotential, ohmic overpotential and concentration overpotential. The activation overpotential (η_{act}) is caused by the local activation reaction barriers for electrochemical reactions. Ohmic overpotential (η_{ohmic}) is caused by electron and ion transport in fuel cell.

Due to the transport resistance, the concentrations of the reactants/products at the reaction sites can differ significantly from those at the electrode surface, causing concentration overpotential (η_{con}) in fuel cell operation process. When a fuel cell operates at a very high current density, the concentration overpotential could be so high that the cell faces the problem of fuel starvation and the performance of the fuel cell would decrease quickly. Thus, in model simulation, local gas concentration is used to show the real local gas activity in fuel cell electrodes.

The actual output voltage of a fuel cell can be obtained by subtracting all the above-mentioned overpotentials from the E_{OCV}, as shown in Eq. (1.3) [78-81].

$$\mathrm{V} = E_{ocv} - \eta_{act} - \eta_{ohmic} - \eta_{con} \tag{1.3}$$

1.3.2.1 Equilibrium potential

In the porous cathode, O_2 molecules diffuse through the porous cathode to the TPB, where they are reduced to oxygen ions (O^{2-}) via reactions (1.4) [82-84].

$$O_2 + 4e^- \rightarrow 2O^{2-} \tag{1.4}$$

The oxygen ions transport through the dense electrolyte to TPB in the anode, where they electrochemically react with gaseous fuel molecules to generate electrons and oxidants. For H_2 and CO molecules, the electrochemical oxidization reactions are shown as reactions (1.5) and (1.6) [85-87].

$$\mathrm{H}_2 + O^{2-} \rightarrow H_2\mathrm{O} + 2e^- \tag{1.5}$$

$$CO + O^{2-} \rightarrow CO_2 + 2e^- \tag{1.6}$$

The overall electrochemical reaction for H_2 and CO can thus be expressed as:

$$H_2 + 0.5O_2 \rightarrow H_2O \tag{1.7}$$

$$CO + 0.5O_2 \rightarrow CO_2 \tag{1.8}$$

The equilibrium potential for reactions (1.7) and (1.8) can be determined by Eq. (1.9) and Eq. (1.10) [49, 88-92]. The concentration overpotentials are included in the equilibrium potential as the gas partial pressures at the reaction sites are used in the calculation.

$$E_{H_2} = E_{H_2}^0 + \frac{RT}{2F} \ln \left[\frac{P_{H_2}^L (P_{O_2}^L)^{1/2}}{P_{H_2O}^L} \right] \tag{1.9}$$

$$E_{CO} = E_{CO}^0 + \frac{RT}{2F} \ln \left[\frac{P_{CO}^L (P_{O_2}^L)^{1/2}}{P_{CO_2}^L} \right] \tag{1.10}$$

E^0 is the potential under standard conditions. R is the universal gas constant. T is the operating temperature (K). F is the Faraday constant. P^L is the local gas partial pressure at the reaction sites. The value of E^0 for H_2 and CO fuel at a temperature between 600K and 1200K can be calculated by Eqs. (1.11) and (1.12)[47, 93, 94]:

$$E_{H_2}^0 = 1.253 - 0.00024516T \text{ (V)} \tag{1.11}$$

$$E_{CO}^0 = 1.46713 - 0.0004527T \text{ (V)} \tag{1.12}$$

Thus, the Nernst potential using H_2 and CO as fuel can be calculated by Eqs. (1.13) and (1.14), respectively.

$$E_{co} = 1.253 - 0.00024516T + \frac{RT}{2F} \ln \left[\frac{P_{H_2}^L (P_{O_2}^L)^{1/2}}{P_{H_2O}^L} \right] \tag{1.13}$$

$$E_{co} = 1.46713 - 0.0004527T + \frac{RT}{2F} \ln \left[\frac{P_{CO}^L (P_{O_2}^L)^{1/2}}{P_{CO_2}^L} \right] \tag{1.14}$$

As concentration overpotential is already included in calculation of equilibrium potential, the calculation of operating potential (Eq. (1.3)) can be reduced to Eq. (1.15) as:

$$V = E_{ocv} - \eta_{act} - \eta_{ohmic} \tag{1.15}$$

1.3.2.2 Activation overpotential

Activation overpotential is the energy loss involved in the electrochemical reaction, which is related to the electrode kinetics at the reaction site. The Butler-Volmer equation (Eq. (1.16)) is widely used for determining the relationship between the activation overpotential and the current density for different kinds of fuels like H_2/H_2O and CO/CO_2 [95-97].

$$i = i_0 \left\{ \exp\left(\frac{\alpha n F \eta_{act}}{RT}\right) - \exp\left(\frac{(1-\alpha) n F \eta_{act}}{RT}\right) \right\} \quad (1.16)$$

Here i_0 is the exchange current density representing the activity of the electrode, α is the electronic transfer coefficient and n is the number of electrons transferred per electrochemical reaction.

1.3.2.3 Ohmic overpotential

The ohmic overpotential in the DC-SOFC is caused by electron/ion conduction. The ionic conductivity of the electrolyte and the ionic/electronic conductivities of the electrodes are the dominate factors for ohmic overpotential. The ohmic overpotential can be calculated with the Ohm's law as shown in Eqs. (1.17) and (1.18) [98, 99]:

$$i_l = -{\sigma_l}^{eff} \nabla(\emptyset_l) \quad (1.17)$$

$$i_s = -\sigma_{s.eff} \nabla(\emptyset_s) \quad (1.18)$$

Here $\sigma_{l.eff}$ and $\sigma_{s.eff}$ are the effective ionic and electronic conductivities. $\emptyset_l$ and $\emptyset_s$ are the ion conducting and electron conducting electric potentials, respectively. In the porous electrodes, the effective conductivities are related to the structural parameters including volume fraction and tortuosity as shown in Eqs. (1.19) and (1.20).

$${\sigma_l}^{eff} = \sigma_l \cdot \frac{V_l}{\tau_l} \quad (1.19)$$

$${\sigma_s}^{eff} = \sigma_s \cdot \frac{V_s}{\tau_s} \quad (1.20)$$

Here σ_l and σ_s are the intrinsic ionic and electronic conductivities

1.3.3 Chemical reactions

Apart from electrochemical reaction, chemical reaction is another key factor affecting the performance of SOCs. In different kinds of SOCs, the key chemical reactions are different. Overall, there are mainly three important chemical reactions in the following studies.

1.3.3.1 Boudouard reaction

Boudouard reaction is the key chemical reaction in DC-SOFCs. It occurs between solid carbon and CO_2 in anode chamber, which is described as shown in reaction (1.21) [100-102].

$$C + CO_2 \leftrightarrow 2CO \tag{1.21}$$

It should be noted that the initial CO_2 comes from the oxidation of carbon by the initial O_2 in the anode chamber. When the SOFC is in operation, CO_2 can be continuously provided from the electrochemical reaction.

1.3.3.2 Carbon steam gasification

When H_2O is used as the gasification agent in DC-SOFCs, the main chemical reaction rate in anode chamber is the water gasification reaction as shown in Eq. $C + H_2O \leftrightarrow CO + H_2$ (1.22) [103-105].

$$C + H_2O \leftrightarrow CO + H_2 \tag{1.22}$$

1.3.3.3 Water gas shift reaction

Water gas shift reaction (WGSR) catalyzed by nickel in anode electrode also plays an important role as shown in Eq. $CO + H_2O \leftrightarrow CO_2 + H_2$ (1.23). This reaction converts CO into H_2 and ensures H_2 to mainly participate in electrochemical reaction [106].

$$CO + H_2O \leftrightarrow CO_2 + H_2 \tag{1.23}$$

1.3.4 Mass transport

In the gas channel and porous electrodes, both free molecular diffusion and Knudsen diffusion are considered in this mass transport model. Free molecular diffusion dominates in gas channel and large pores while Knudsen diffusion becomes significant when pore sizes are comparable or smaller than molecular mean-free path. The extended Fick's model is used to describe gas transport in the channel and porous electrodes as shown in Eq. $N_i = -\frac{1}{RT}\left(\frac{B_0 y_i P}{\mu}\frac{\partial \mathrm{P}}{\partial \mathrm{z}} - D_i^{eff}\frac{\partial (y_i \mathrm{P})}{\partial \mathrm{z}}\right)\ (i = 1, \dots, n)$ (1.24):

$$N_i = -\frac{1}{RT}\left(\frac{B_0 y_i P}{\mu}\frac{\partial \mathrm{P}}{\partial \mathrm{z}} - D_i^{eff}\frac{\partial (y_i \mathrm{P})}{\partial \mathrm{z}}\right) \ (i = 1, \ldots, n) \quad (1.24)$$

Where N_i represents the flux of mass transport, B_0 is the permeability coefficient, y_i is the mole fraction of component i, μ is the dynamic viscosity of the gas mixture and D_i^{eff} is the effective diffusivity of species i. The effective diffusion coefficient (D_i^{eff}) considering both molecular diffusion coefficient (D_{im}^{eff}) and Knudsen diffusion coefficient (D_{ik}^{eff}) and can be calculate as Eq. (1.25) [107-111]:

$$D_i^{eff} = \frac{\varepsilon}{\tau}\left(\frac{1}{D_{im}^{eff}} + \frac{1}{D_{ik}^{eff}}\right)^{-1} \quad (1.25)$$

Here ε is the volume fraction of the pores, τ is the tortuosity factor. D_{im}^{eff} and D_{ik}^{eff} depend on the micro-structure of the porous electrode and operating conditions. More detailed calculation procedures of these two parameters can be found in reference [112-114].

1.3.5 Momentum transport

The general Navier-Stokes (N-S) equation is used to describe the momentum conservation. For momentum conservation in channels, the N-S equation can be described as shown in Eq. (1.26) [115-118]:

$$\rho\frac{\partial u}{\partial t} + \rho u \nabla u = -\nabla p + \nabla[\mu\left(\nabla u + (\nabla u)^T\right) - \frac{2}{3}\mu \nabla u\right] \quad (1.26)$$

For momentum conservation in porous electrodes and the anode chamber, the N-S equation is modified by including the Darcy's term for momentum conservation:

$$\rho\frac{\partial u}{\partial t} + \rho u \nabla u = -\nabla p + \nabla[\mu\left(\nabla u + (\nabla u)^T\right) - \frac{2}{3}\mu \nabla u\right] - \frac{\varepsilon \mu u}{k} \quad (1.27)$$

Here ρ is the gas density, u is the velocity vector, p is pressure and ε is the porosity of the electrode.

1.3.6 Heat transfer model

In DC-SOFCs, electrochemical reactions in TPB sites generates heat while the chemical reaction (Boudouard reaction) in anode chamber consumes heat. This will not only result in the gradient of temperature along the cell length, but also along the cell width. General heat balance equation is used to describe the heat transfer in the cell as [119-121]:

$$\rho C_p u \cdot \nabla T + \nabla \cdot \left(-\lambda_{eff} \nabla T\right) = Q \tag{1.28}$$

Here C_p is the fluid heat capacity at constant pressure, u is the fluid velocity field, λ_{eff} is the effective thermal conductivity and Q is the heat source. In the porous structure of electrodes, λ_{eff} can be calculated as:

$$\lambda_{eff} = (1 - \varepsilon)\lambda_s + \varepsilon\lambda_l \tag{1.29}$$

where λ_s and λ_l are heat conductivity of solid and liquid phase, respectively.

1.4 Recent research on direct carbon solid oxide fuel cells (DC-SOFCs)

The direct use of solid carbon as a fuel in SOFCs offers a new strategy for efficient and environmental friendly power generation. Due to its high efficiency and easy emission control, the DC-SOFC has received more and more attention since Nakagawa and Ishida's first experimental study [122]. Lee et al. [123] performed system exergy analyses of DC-SOFCs and found that the conversion efficiency of DC-SOFCs was much higher than a carbon fueled SOFC system with separate carbon gasification unit and SOFC unit. They also demonstrated a power density of 220 mW cm^{-2} at 0.68 V at 1178 K. Li et al. [124] combined fluidized bed and DC-SOFC to convert solid carbon into electricity for the first time. Based on GC analysis of the reaction products, they proposed the CO_2 shuttling mechanisms in DC-SOFC: the electrochemically produced CO_2 from CO at the TPB of SOFC diffuses to the C bed for CO production from C through carbon gasification.

The gasification reaction between solid carbon and CO_2 is called as reversible Boudouard reaction, which is a key reaction affecting the performance of DC-SOFC. As reported by Wu et al.[125], adopting Fe_mO_n-alkaline metal oxide catalyst greatly enhanced CO formation rate in graphite (e.g. 19 times improvement at 800 ºC) and activated carbon (e.g. 6 to 155 times improvement at 800 ºC depending on the surface area). Benefited from the largely enhanced Boudouard reaction, they successfully obtained a peak power density of 286 mW cm^{-2} at 1123 K even without external CO_2 feeding. Similarly, Tang et al. [126] significantly improved the performance of DC-SOFC (10 times higher output power density at 1073K) by loading Fe-based catalyst on the carbon fuel. Considering the importance of catalyst for Boudouard reaction in DC-SOFCs, Li et al.[127] compared Ni, K and Ca additives in carbon black and found that the catalytic effects were: K>Ni>Ca. Borja et al. [128] further studied the synergistic effect of the carbonate catalysts and Li-K carbonate system displayed the highest power densities compared with Li-Na, Li-Na-K, Li-Ba and Na-K carbonate mixtures. Apart from the use of catalysts, the carbon structure also affects the Boudouard reaction rate. Jiao et al. [129] treated coal char with alkali for structure modification to enlarge its specific surface. The output power density of DC-SOFCs was increased significantly from 62 mW cm^{-2} to 220 mW cm^{-2} at 1123K.

In addition, some researchers recently proposed using H_2O instead of CO_2 as agent for carbon gasification. Ong and Ghoniem [130] developed a 1D model to compare H_2O and CO_2 as gasification agent for the indirect carbon fuel cell. The performance of the carbon fuel cell with external carbon gasification was improved by 3-5 times with H_2O recycling from anode to the gasifier instead of CO_2 between 700 ºC and 800 ºC. In addition, the thermal coupling between the carbon gasifier and the SOFC significantly raises efficiency. More recently, experimental and modeling works on DC-SOFC with internal carbon gasification by CO_2 and H_2O were conducted by Xu et al. [131]. Benefited from a much faster carbon gasification rate with H_2O as agent, a significant improvement of peak power density was found from 158 mW cm^{-2} (with CO_2 as agent) to 385 mW cm^{-2} (with H_2O as agent) at 1123K.

Apart from being utilized in the SOFC, solid carbon can also be used in the SOEC. For practical application of an SOEC, its electricity consumption needs to be further reduced as the quality of electricity (i.e. exergy) is high. Recent studies have demonstrated that by supplying low cost fuel (such as CH_4 and solid carbon) to the anode of SOEC (termed as fuel-assisted SOEC: FA-SOEC) for steam electrolysis could significantly reduce the operating potential of SOEC, thus greatly reduce the electrical power consumption [132, 133]. When fuel is supplied to the SOEC anode to consume the oxygen ions to reduce the oxygen partial pressure, the equilibrium potential can be greatly reduced. If the fuel concentration in anode is sufficiently high and the operating current is relatively low, the required potential for electrolysis could become negative. This means that the FA-SOEC can generate electrical power rather than consume it [134]. Therefore, the FA-SOEC can also be considered as an SOFC whose oxygen ions come from H_2O, instead of from O_2 molecules.

1.5 Research gaps and main contents

The above-mentioned studies demonstrated the high efficiency and gas-electricity cogeneration of DC-SOFC. However, most of them are experimental research and only some preliminary modeling studies are available.

Firstly, the current literature is lacking a detailed analysis on the physical/chemical processes of a DC-SOFC. In practice, the carbon fuel may be located at a certain distance from the DC-SOFC anode. The effect of this distance on the DC-SOFC performance is still unknown but it is an important factor for practical and large-scale application of DC-SOFC. The previous studies on DC-SOFC employed the electrolyte-supported configuration. It is unknown whether the anode-supported configuration is favorable or not, as the chemical and electrochemical reactions in the porous anode of a DC-SOFC are more complicated than a conventional SOFC running on gaseous fuels. In addition, the characteristics of CO generation from the DC-SOFC have not been well studied and understood yet.

Secondly, although the use of CO_2 as a gasification agent has been demonstrated to be feasible for DC-SOFC, the operating temperature of CO_2-assisted DC-SOFC is usually quite high, typically $\geq$1123K, due to the relatively low gasification kinetics even with catalyst. The high operating temperature limits the choice of materials for the interconnect and causes coarsening of catalyst particles in the long-term operation, which in turn causes high cost and poor durability of DC-SOFC.

To fill the above-mentioned research gap, 2D mathematical models are developed for an axisymmetric-tubular DC-SOFC. The models are validated with the experimental data and parametric simulations are conducted to understand the physical/chemical processes in the SOCs.

In Chapter 2, the model is focused on the CO and electricity cogeneration characteristics in DC-SOFCs. In Chapter 3, thermal effects on the DC-SOFC temperature distribution are detailed studied. In Chapter 4, the effects of different gasification agent (H_2O/CO_2) on DC-SOFC performance are compared based on experiments and numerical simulation. In Chapter 5, experiments are conducted to investigate the performance improvement brought by catalytical in-situ steam-carbon gasification reaction. Numerical models are also developed to study the detailed chemical/physical processes. In Chapter 6 the concept of carbon assisted solid oxide electrolysis cell (CA-SOEC) is proposed and a 2D mathematical model is developed for H_2O electrolysis and syngas production.

2. CHAPTER 2 MODELING OF DIRECT CARBON SOLID OXIDE FUEL CELL FOR ELECTRICITY AND CO CO-GENERATION

2.1 Introduction

SOFCs can offer a high efficiency to the energy conversion from solid carbons to electricity power. On the other hand, solid carbons can significantly decrease the fuel cost of SOFCs and providing a high volumetric energy density simultaneously. These great benefits brought by the combination of solid carbons and SOFCs attracts a lot of research interest from all over the world. Although a lot of experimental studies have been conducted, the related theoretic analysis is quite limited and it is urgent to understand the detailed physical/chemical processes in the DC-SOFC.

In this chapter, a 2D mathematical model is developed for an axisymmetric-tubular DC-SOFC. The model is validated with the experimental data on DC-SOFC. Parametric simulations are conducted to understand the physical/chemical processes in the DC-SOFC with a focus on the CO and electricity cogeneration characteristics.

2.2 Model development

2.2.1 Model assumption and calculation domain

A 2D numerical model is developed to describe the electrochemical reaction, chemical reactions, ion/electronic charge transport, mass transport and momentum transport in a tubular DC-SOFC. In the literature, Liu et al.'s work on DC-SOFC provided detailed experimental setup and operating conditions, such as the materials used, the operating temperature, the thickness of cell components, etc. In their study, the current-potential (I-V) characteristics of an electrolyte-supported tubular SOFC were measured. Thus, their cell configuration is used for the present model and their experimental data are used for model validation.

The schematic of the electrolyte supported tubular DC-SOFC is shown in Fig. 2.1(a). Activated carbon is supplied to the anode chamber and air is supplied to the cathode channel. The initial O_2 in the anode chamber reacts with the activated carbon to produce CO_2, which reacts with carbon through the Boudouard reaction to form CO. The produced CO molecules diffuse into the porous anode and reacts with O^{2-} at the

TPB to form CO_2 molecules, which subsequently diffuse back from the TPB to the anode chamber to react with the carbon fuel for CO generation. These processes repeat between the anode chamber and the porous anode to produce CO and generate electricity as shown in Eqs. (2.1, 2.3-2.5).

The electrochemical part of the cell has a length of 9mm, an inner diameter of 11.518mm and an outer diameter of 12mm. The thicknesses of the anode, electrolyte and cathode are 20μm, 201μm and 20μm, respectively. The thicknesses of anode and electrolyte are exchanged when the anode-supported configuration is considered. The modeled tubular DC-SOFC uses Ag-GDC composites (mixture of GDC (gadolinium doped ceria, Ce0.8Gd0.2O1.9) and silver) as both electrodes and YSZ (yttrium stabilized zirconium) as electrolyte. The two electrodes are porous enough for gas transport and the electrolyte is dense enough to be gas-tight. The current density is measured at operating potentials ranging from 0.2 V to 0.9 V.

The main assumptions are shown below.

(1) The electrochemical reactions spatially take place along the electrode thickness within the porous electrode. The electrochemical reaction active sites are assumed to be uniformly distributed in the porous electrodes. The two conducting phases (electronic and ionic) in the porous electrodes are continuous and homogeneous.
(2) The ionic and electronic charge transport processes take place in the PEN (Positive Electrode-Electrolyte-Negative electrode assembly). The charge transfer reaction can take place at TPB throughout the porous electrode.
(3) All gases (CO, CO_2, H_2, H_2O, O_2 and N_2) are ideal gases. The gas flow is incompressible.
(4) Temperature distribution in the DC-SOFC is uniform due to the small size of the modeled cell.
(5) The volume of activated carbon fuel in the anode chamber does not change with time.

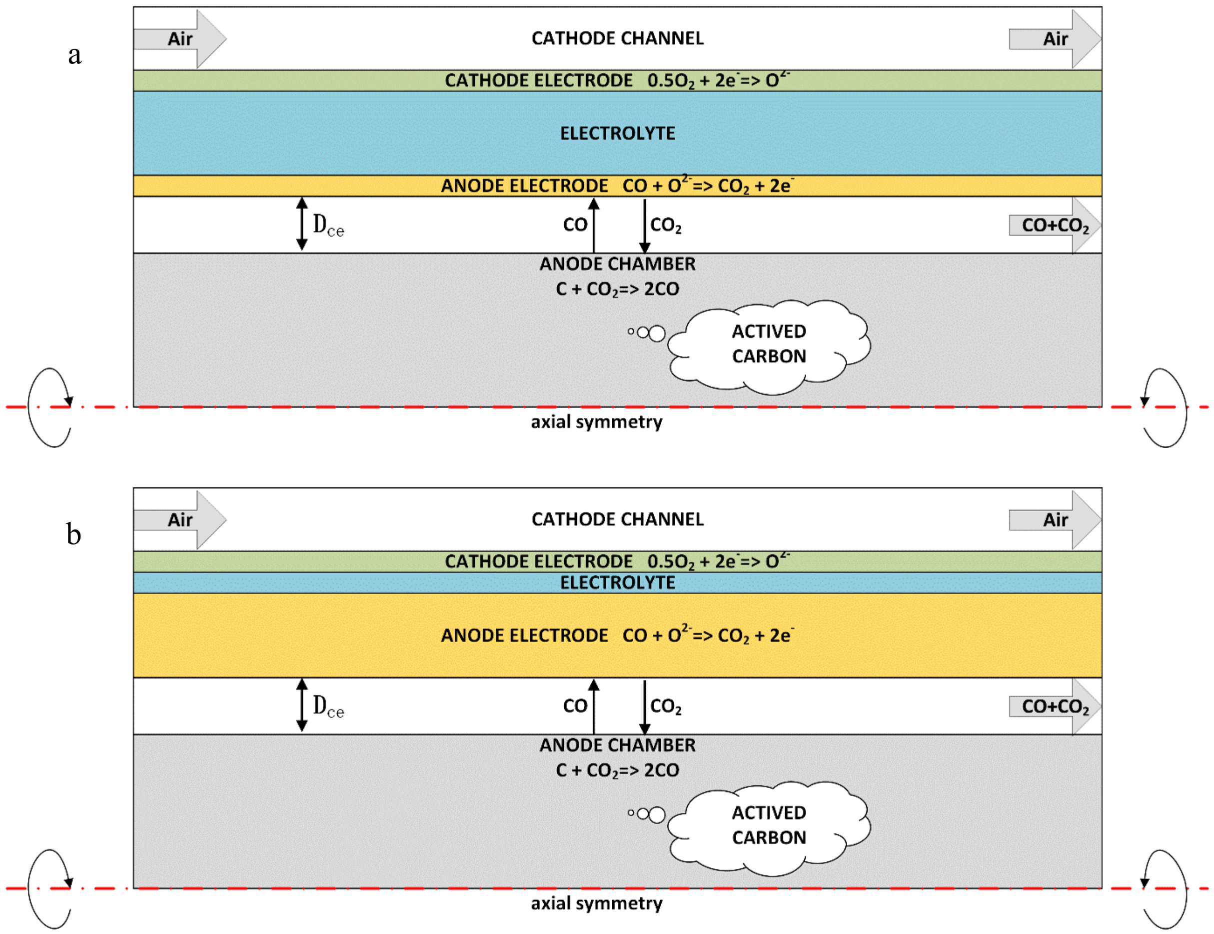

Figure 2.1 Schematic of (a) electrolyte supported DC-SOFC, (b) anode supported DC-SOFC

2.2.2 Governing equations

The 2D model consists of the following sub-models: chemical reaction model, electrochemical reaction model, mass transport model and momentum transport model.

2.2.2.1 Chemical reaction model

The chemical reaction model is used to calculate the reaction rate of the reversed Boudouard reaction in the anode chamber:

$$C + CO_2 \leftrightarrow 2CO \tag{2.1}$$

It should be noted that the initial CO_2 comes from the oxidation of carbon by the initial O_2 in the anode. When the DC-SOFC is in operation, CO_2 is continuously produced from the electrochemical reaction. The rate of reversed Boudouard reaction (R_{C_CO2}) can be obtained as [135]:

$$R_{C\_CO2} = K_{br}\exp(-E_{br}/RT)c_{CO_2} \tag{2.2}$$

2.2.2.2 Electrochemical reaction model

The electrochemical reaction model is developed to compute the electrochemical reaction rate (related to current density) at given operating potential. As shown in Fig. 2.1, the gas mixture of CO/CO_2 flows in the anode while air is supplied to the cathode. In the porous cathode, O_2 molecules diffuse through the porous cathode to the TPB, where they are reduced to oxygen ions (O^{2-}) via reactions (2.3).

$$O_2 + 4e^- \rightarrow 2O^{2-} \tag{2.3}$$

The oxygen ions transport through the dense electrolyte to TPB in the anode, where they electrochemically react with CO molecules to generate electrons and CO_2:

$$2CO + 2O^{2-} \rightarrow 2CO_2 + 4e^- \tag{2.4}$$

The overall electrochemical reaction can be obtained by combining Eq. (2.3) and Eq. (2.4) as:

$$2CO + O_2 \rightarrow 2CO_2 \tag{2.5}$$

The operating potential from the DC-SOFC can be determined using the equilibrium potential and the various overpotential losses:

$$V = E + \eta_{act,an} + \eta_{act,ca} + \eta_{ohmic} \tag{2.6}$$

E is the equilibrium potential (Nernst potential) when the current density is 0. η_{act} is the activation overpotential reflecting the energy barrier needed for the electrochemical reaction to proceed. η_{ohmic} is the ohmic overpotential related to the ionic/electronic conduction. The concentration overpotentials are not explicitly included in Eq. 2.6 as they are included in the equilibrium potential calculation.

In the DC-SOFC, the equilibrium potential including concentration overpotential for reactions (2.5) can be determined by Eq. (2.7).

$$E_{co} = 1.46713 - 0.0004527T + \frac{RT}{2F}\ln\left[\frac{P_{CO}^{L}(P_{O_2}^{L})^{1/2}}{P_{CO_2}^{L}}\right] \tag{2.7}$$

Activation overpotential is calculated by the Butler-Volmer equation as shown in Eq. (2.8).

$$i = i_0 \left\{ \exp\left(\frac{\alpha n F \eta_{act}}{RT}\right) - \exp\left(\frac{(1-\alpha) n F \eta_{act}}{RT}\right) \right\} \quad (2.8)$$

The ohmic overpotential can be calculated with the Ohm’s law:

$$i_l = -\sigma_l{}^{eff} \nabla(\emptyset_l) \quad (2.9)$$

$$i_s = -\sigma_{s.eff} \nabla(\emptyset_s) \quad (2.10)$$

$$\sigma_l{}^{eff} = \sigma_l \cdot \frac{V_l}{\tau_l} \quad (2.11)$$

$$\sigma_s{}^{eff} = \sigma_s \cdot \frac{V_s}{\tau_s} \quad (2.12)$$

The conductivities, porosities and volume fractions of ionic/electronic phases are summarized in Table 2.1 Model parameters. The tortuosity can be found in Table 2.4 Model tuning parameters, and it is a tuning parameter for model validation.

Table 2.1 Model parameters[136, 137]

Parameters	**Value or expression**	**Unit**
Ionic conductivity		
GDC	$\frac{100}{T} \times 10^{(6.66071 - \frac{5322.92}{T})}$	Sm^{-1}
YSZ	$3.34 \times 10^4 e^{\frac{-10300}{T}}$	Sm^{-1}
Electronic conductivity		
Ag	$\frac{1.59e^8}{(0.0038T-0.1134))}$	Sm^{-1}
Porosity		
Cathode	0.46	
Anode	0.46	
Electrode volume fraction		
GDC	0.21	
Ag	0.79	

S_{TPB}		
Cathode layer	2.14×10^5	m^2m^{-3}
Anode layer	2.14×10^5	m^2m^{-3}

2.2.2.3 Mass transport model

In the porous electrodes of DC-SOFC, both free molecular diffusion and Knudsen diffusion are considered. Free molecular diffusion dominates in large pores and Knudsen diffusion becomes significant when pore sizes are comparable or smaller than molecular mean-free path. The extended Fick's model is used to describe gas transport in the porous electrodes as:

$$N_i = -\frac{1}{RT}\left(\frac{B_0 y_i P}{\mu}\frac{\partial \mathrm{P}}{\partial \mathrm{z}} - D_i^{eff}\frac{\partial(y_i \mathrm{P})}{\partial \mathrm{z}}\right) \quad (i = 1, \ldots, n) \qquad (2.13)$$

$$D_i^{eff} = \left(\frac{1}{D_{im}^{eff}} + \frac{1}{D_{ik}^{eff}}\right) \qquad (2.14)$$

D_{im}^{eff} and D_{ik}^{eff} depend on the micro-structure of the porous electrode and operating conditions.

2.2.2.4 Fluid flow model

The general N-S equation is used to describe the momentum conservation. In the gas channels, the N-S equation can be described as:

$$\rho\frac{\partial u}{\partial t} + \rho u\nabla u = -\nabla p + \nabla\Big[\mu\Big(\nabla u + (\nabla u)^T\Big) - \frac{2}{3}\mu\nabla u\Big] \qquad (2.15)$$

In the porous electrodes and the anode chamber, the N-S equation is modified by including the Darcy's term for momentum conservation:

$$\rho\frac{\partial u}{\partial t} + \rho u\nabla u = -\nabla p + \nabla\Big[\mu\Big(\nabla u + (\nabla u)^T\Big) - \frac{2}{3}\mu\nabla u\Big] - \frac{\varepsilon\mu u}{k} \qquad (2.16)$$

Here ρ is the gas density, u is the velocity vector, p is pressure and ε is the porosity of the electrode.

2.2.3 Boundary conditions

The electric potentials are specified at the outer boundaries of cathode and anode as working potential and zero potential, respectively. The insulation condition is applied to the bottom and top of the cell.

Inflow gas mole fraction is specified at the inlet of the cathode. The convective flux boundary condition is specified at the outlets of the cathode and anode. Zero flux is assumed at the end of anode chamber, electrolyte/electrode interface and the ends of electrodes.

Standard gas flow rate (standard cubic centime per minute: SCCM) is specified at the cathode while pressure condition is specified at the outlet. No-slip condition is applied to the end of anode chamber, electrolyte/electrode interface and the ends of electrodes.

2.2.4 Model parameters

For model validation, the values of material properties and operation parameters are set to be the same as the experimental conditions in ref. [138] as shown in Table 2.1, Table 2.2 and Table 2.3. The electrochemical characteristics of the model are validated with the experimental data using H_2 as a fuel for SOFC. The exchange current density for CO oxidation in DC-SOFC ($i_{0,co}$) is assumed to be 0.45 times that of H_2 oxidation in a H_2-fueled SOFC. The rate of Boudouard reaction depends on reaction area and activity of catalyst. These effects are fully considered by tuning the equilibrium parameter (K_{br}). In the parametric simulations, the parameters are varied to evaluate their effects on the DC-SOFC performance. The tuning parameters used for the base-case simulation are summarized in Table 2.4.

Table 2.2 Operation parameters for model validation (H_2-SOFC)

Parameter	**Value**	**Unit**
Anode inlet gas flow rate for	50	SCCM
Cathode inlet gas flow rate	10	SCCM
Anode inlet gas composition	H_2 (97%) + H_2O (3%)	
Cathode inlet gas composition	Air	
Temperature	1123	K

Table 2.3 Operation parameters for model validation (DC-SOFC)

Parameter	**Value**	**Unit**

Anode inlet gas flow rate	0	
Distance between anode chamber and electrode, D_{ce}	59	μm
Cathode inlet gas flow rate	10	SCCM
Cathode gas composition	Air	
Temperature	1123	K

Table 2.4 Model tuning parameters

Parameter	**Value**	**Unit**
Cathode tortuosity	3	
Anode tortuosity	3	
H_2 exchange current density, i_{H_2}	1000	Am^{-2}
O_2 exchange current density i_{O_2}	400	Am^{-2}
CO exchange current density, i_{CO}	450	Am^{-2}
H_2 charge transfer coefficient, α_{H_2}	0.5	
CO charge transfer coefficient, α_{CO}	0.5	
O_2 charge transfer coefficient, α_{O_2}	0.5	
Equilibrium constant of Boudouard reaction	6×10^{13}	1/s

2.2.5 Model solution

The model is solved at certain cell potential, inlet gas flow rate, inlet gas species mole fraction, and temperature. The outputs of the model are the distributions of current density, species concentration, chemical reaction rates and others. The calculations are performed using the finite element commercial software COMSOL MULTIPHSICS®.

2.3 Results and discussion

2.3.1. Model validation

In this section, the modeling results of current-potential characteristics are compared with experimental data for model validation. The model tuning parameters are summarized in Table 2.4. The comparison between simulation and experiment is shown in Fig. 2.2. The quite small difference between the modeling results and experimental data validates the present model. A proper mesh density is also chosen by conducting the grid-independence validation shown in Fig. 2.2(c). In the subsequent parametric simulations, the same DC-SOFC structural parameters and tuning parameters are used but the operation temperature, potential and the distance between the carbon chamber and the porous anode (D_{ce}) are changed to investigate their effects on the DC-SOFC performance.

a

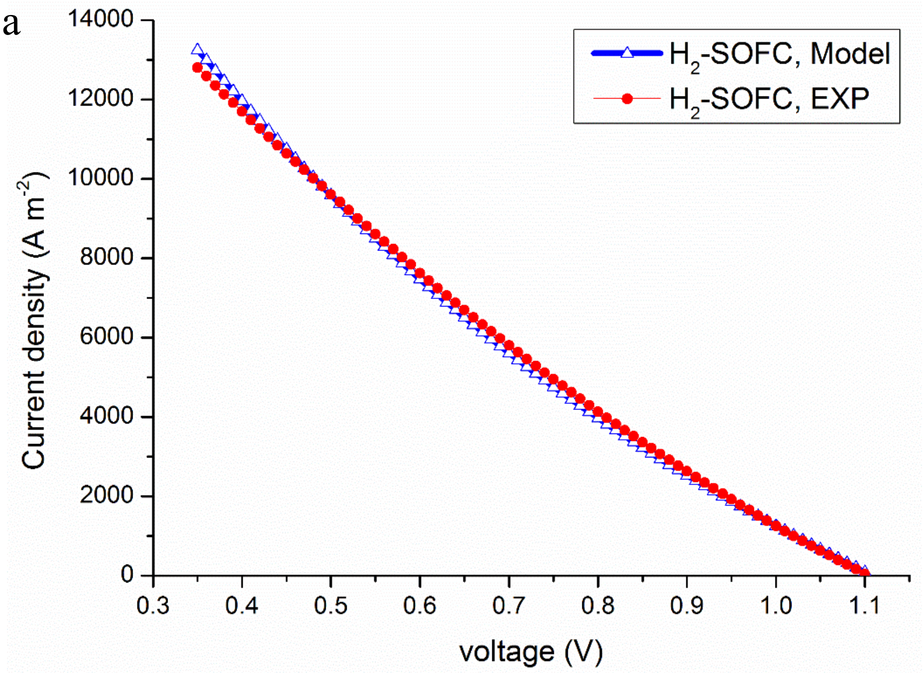

b

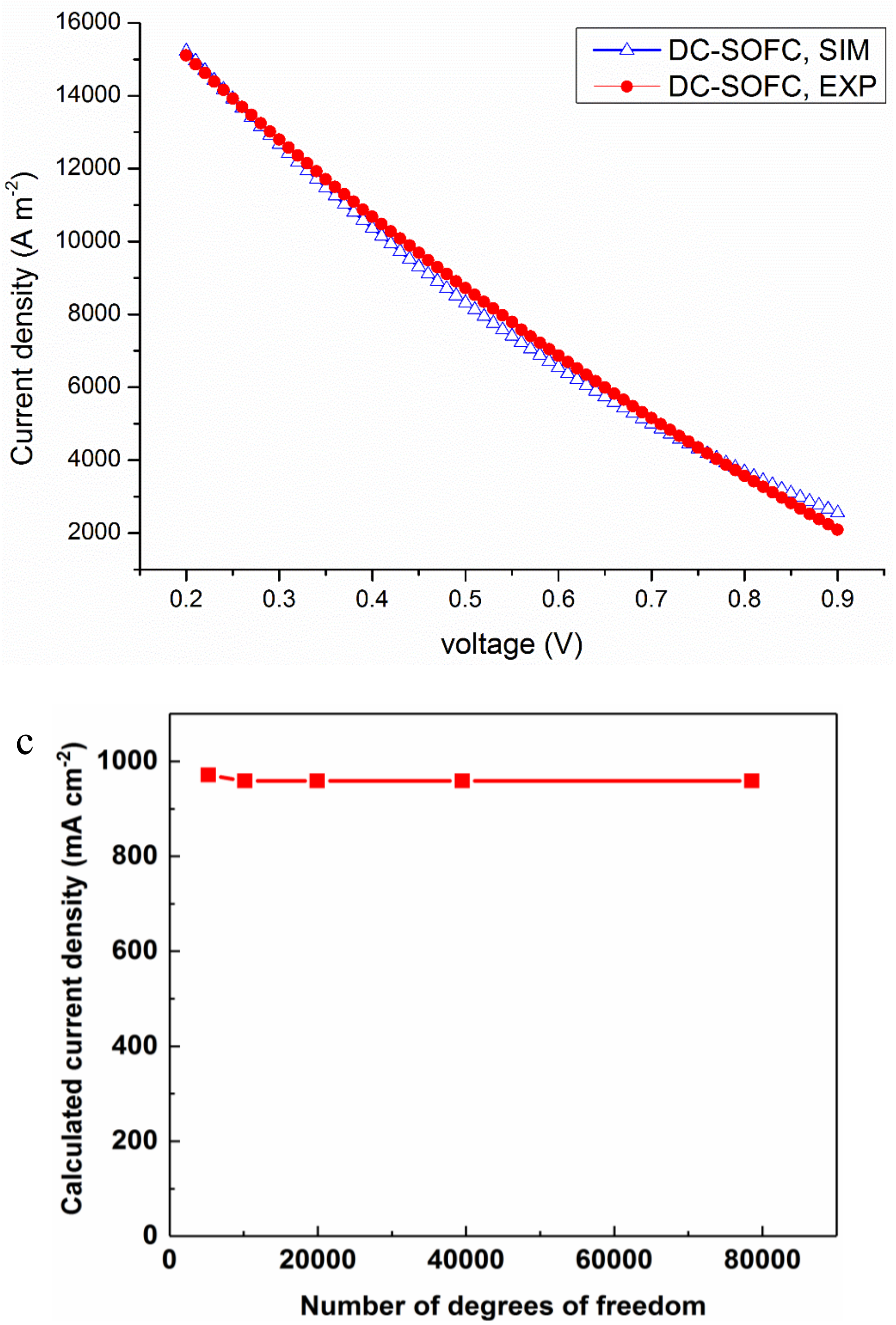

Figure 2.2 Model validation for (a) H_2-SOFC, (b) DC-SOFC and (c) grid-independence.

2.3.2 Effect of distance between carbon and anode

In the DC-SOFC, CO for electrochemical reaction comes from Boudouard reaction between carbon and CO_2. Since CO_2 is produced from the electrochemical reaction in steady-state operation, the counter-diffusion of CO and CO_2 between the carbon chamber and the TPB in the porous anode could be a limiting factor for DC-SOFC performance under certain conditions. As the distance between carbon chamber and anode electrode could play an important role, both the absolute value of D_{ce} and relative value of D_{ce} ($R_{ce} = D_{ce}/L_{cell}$) are studied and discussed in this section. The effects of D_{ce} on DC-SOFC performance are shown from Fig. 2.3 to Fig. 2.5. The detailed operation conditions are shown in Table 2.5.

Table 2.5 Operation parameters for D_{ce} effect study in DC-SOFC

Parameter	**Value**	**Unit**
Operating potential	0.2 - 0.9	V
Anode inlet gas flow rate	0	
Distance between anode chamber and electrode, D_{ce}	59 - 4559	µm
Cathode inlet gas flow rate	10	SCCM
Cathode gas composition	Air	
Temperature	1123	K

The output current density of DC-SOFC is found to increase with decreasing D_{ce} (Fig. 2.3a). The distance effect is more pronounced at a low operating potential (or high current density) but is small at a high operating potential. This phenomenon is caused by both gas transport and electrochemical reaction kinetics. As can be seen in Fig. 2.4, the molar fraction of CO in the carbon chamber is very high (>0.89) under different D_{ce} conditions. When D_{ce} is very small ($D_{ce} = 59\mu m,\ R_{ce} = 0.007$), the CO fraction in the porous anode is also high and very close to that in the carbon chamber. With increasing D_{ce} ($D_{ce} = 4559\mu m,\ R_{ce} = 0.51$), the transport of CO from the carbon chamber to the TPB in the porous anode becomes difficult. Thus, the molar fraction of CO in the porous anode decreases with increasing D_{ce}. When the DC-SOFC is operated at a lower potential (0.2V), the current density is higher and more CO is consumed by electrochemical reaction at the TPB in the porous anode, which causes significant concentration gradient of CO in the porous anode.

Consequently, the performance reduction of DC-SOFC is larger at a lower operating potential and a larger D_{ce}.

It should be noted that although the performance of DC-SOFC decreases with increasing D_{ce}, the performance is still very good even at a large D_{ce} ($D_{ce} = 4559\mu m$, $R_{ce} = 0.51$), as can be seen from Fig. 2.3b. This result indicates that it is feasible to develop large-scale DC-SOFC system since the distance between carbon fuel and anode electrode does not reduce the DC-SOFC performance too much.

It is also found that the current density increases slightly along the cell length in the DC-SOFC (Fig. 2.5). For comparison, the current density decreases significantly along the cell length when gaseous fuel like H_2 and CO is used in SOFC. This is because the CO fuel can be produced from the carbon chamber along the cell length in the DC-SOFC, which results in negligible CO concentration gradient along the channel. However, for H_2 or CO fueled SOFC, the electrochemical consumption of the fuel causes a large fuel concentration gradient along the channel, which results in decreased local equilibrium potential and current density along the cell length direction.

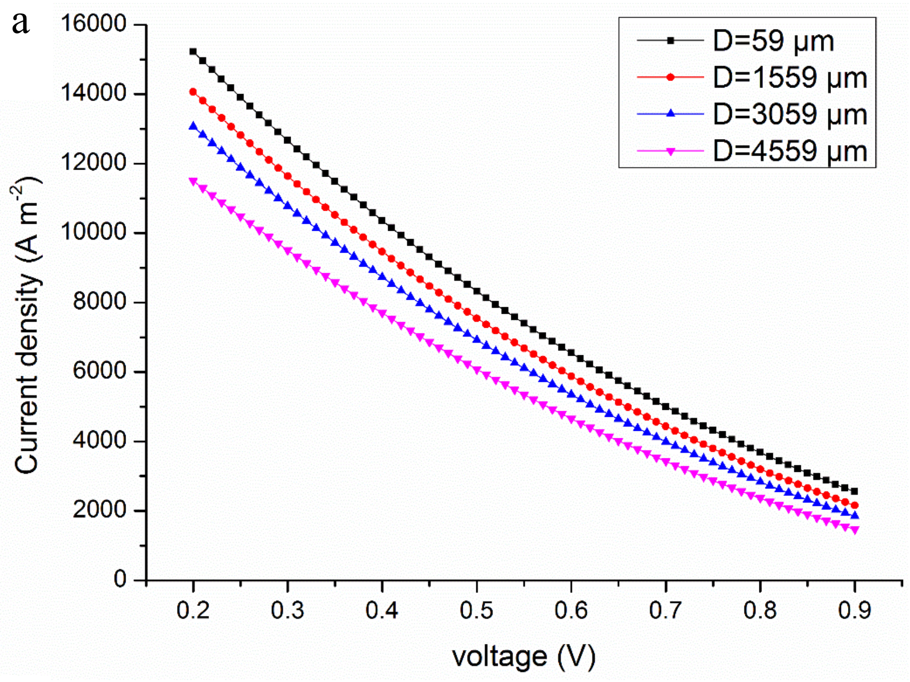

b

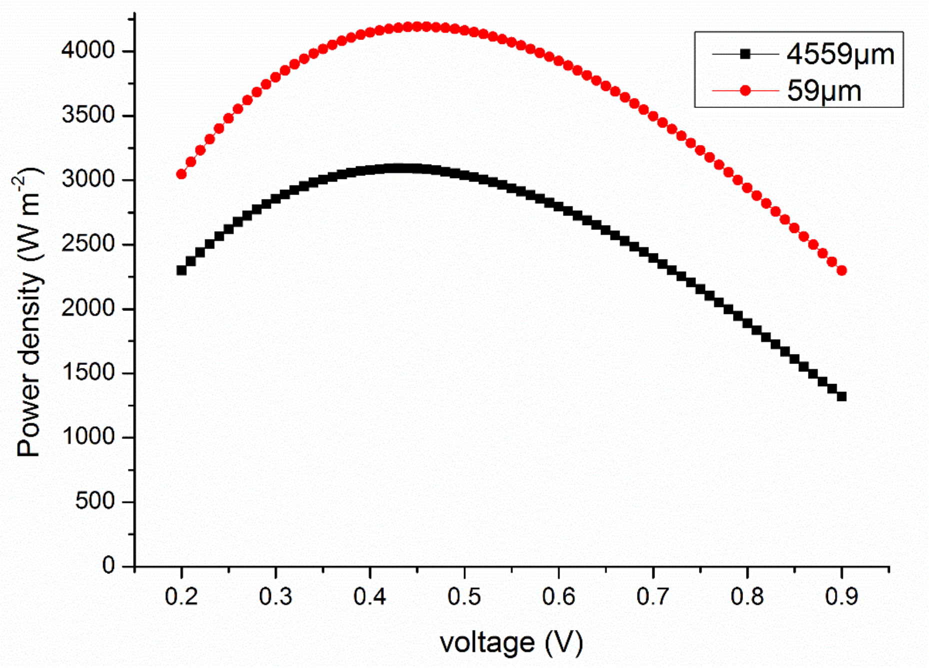

Figure 2.3 Effect of D_{ce} on (a) DC-SOFC output current density, (b) output power density at 1123K.

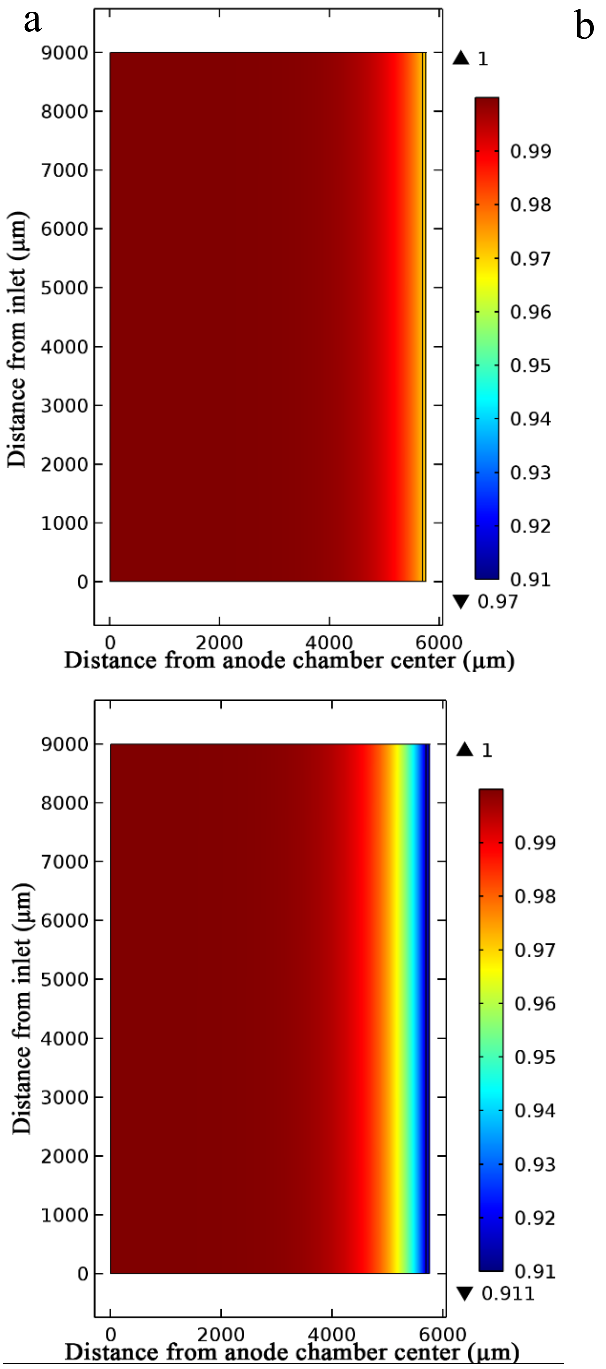
a
b
Distance from inlet (µm)
9000
8000
7000
6000
5000
4000
3000
2000
1000
0
Distance from anode chamber center (µm)
0
2000
4000
6000
▲ 1
0.99
0.98
0.97
0.96
0.95
0.94
0.93
0.92
0.91
▼ 0.97
Distance from inlet (µm)
9000
8000
7000
6000
5000
4000
3000
2000
1000
0
Distance from anode chamber center (µm)
0
2000
4000
6000
▲ 1
0.99
0.98
0.97
0.96
0.95
0.94
0.93
0.92
0.91
▼ 0.911

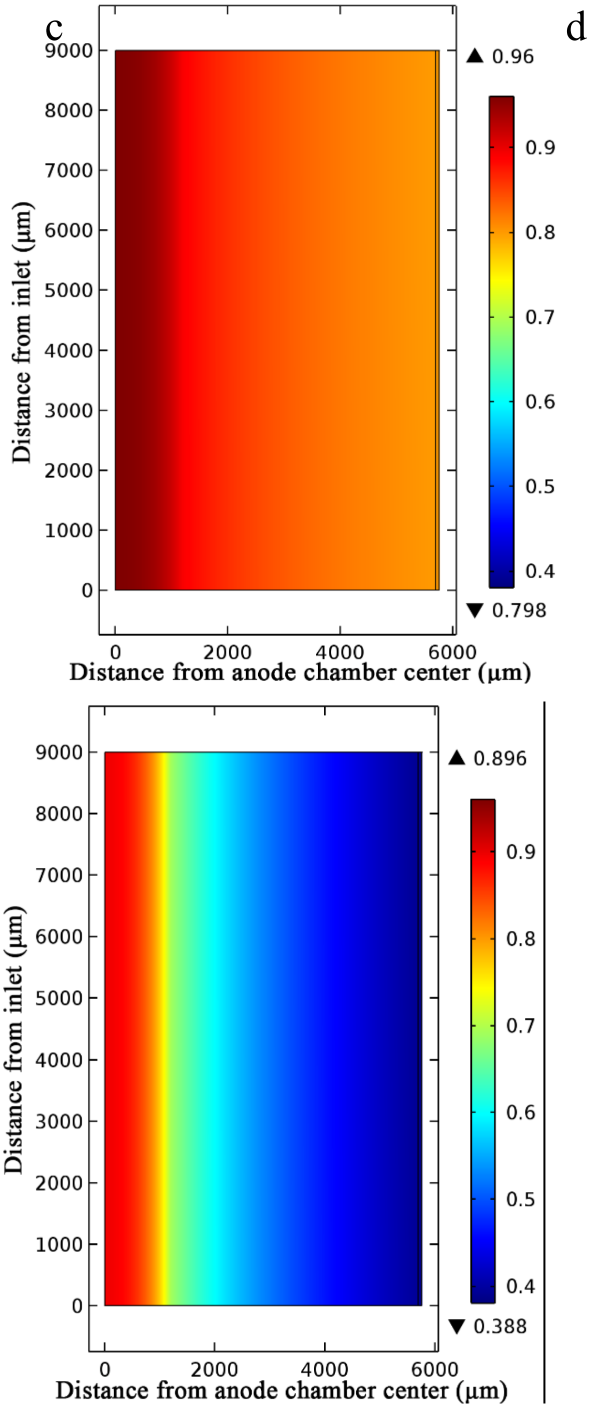

Figure 2.4 Effect of operating potential and D_{ce} on CO molar fraction distribution in DC-SOFC anode at 1123K: (a) $D_{ce} = 59\ \mu\text{m}, \text{V} = 0.7\text{V}$ (b) $D_{ce} = 59\ \mu\text{m}, \text{V} = 0.2\text{V}$ (c) $D_{ce} = 4559\ \mu\text{m}, \text{V} = 0.7\text{V}$ (d) $D_{ce} = 4559\ \mu\text{m}, \text{V} = 0.2\text{V}$

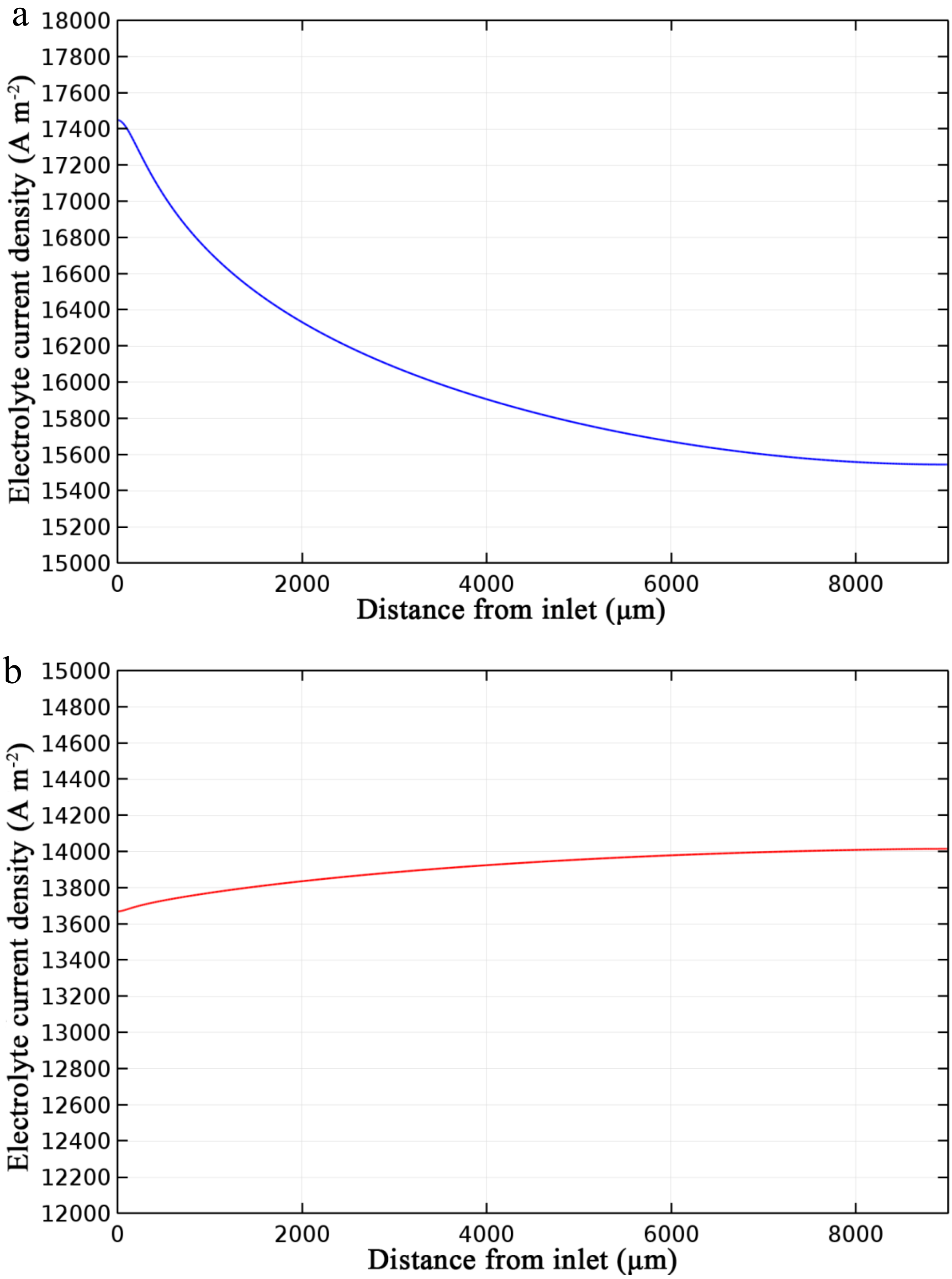

Figure 2.5 Current density distribution along electrolyte in (a) H_2-SOFC and (b) DC-SOFC

2.3.3 Effect of operating temperature

The effects of operating temperature on DC-SOFC are shown in Fig. 2.6. The detailed operating conditions are shown in Table 2.6.

Table 2.6 Operation parameters for temperature effect study in DC-SOFC

Parameter	**Value**	**Unit**
Operating potential	0.7	V
Anode inlet gas flow rate	0	
Distance between anode chamber and electrode, D_{ce}	59 - 4559	μm
Cathode inlet gas flow rate	10	SCCM
Cathode gas composition	Air	
Temperature	973 - 1273	K

As expected, the current density of the DC-SOFC increases with increasing operating temperature (Fig. 2.6a). This is mainly due to the faster Boudouard reaction kinetics at a higher temperature, producing more CO from CO_2 and carbon for electrochemical reaction. In addition, the electrochemical reaction kinetics and the ionic conduction are both improved at a higher temperature. It can also be found from Fig. 2.6b that the molar fraction of CO at the anode outlet is quite high even at a large D_{ce}, when the DC-SOFC is operated at a high temperature (1273K). This result indicates that the CO molar fraction at the DC-SOFC outlet is high and controllable, which demonstrates the feasibility of using carbon fuel in DC-SOFC for electricity and CO co-generation at a high temperature.

The performance of DC-SOFC with a large D_{ce} can also be improved by increasing temperature as can be seen in Fig. 2.6a. The performance of DC-SOFC with 4559 μm D_{ce} at 1223K is very close to that with a D_{ce} of 59μm at an operating temperature of 1123 K. This good performance of DC-SOFC is also benefited from the fast Boudouard reaction kinetics at higher temperature. In addition, the CO molar fraction is much increased at a higher temperature in the DC-SOFC with large D_{ce}, which again indicates that the electricity and CO co-generation at an industry level by DC-SOFC could be feasible.

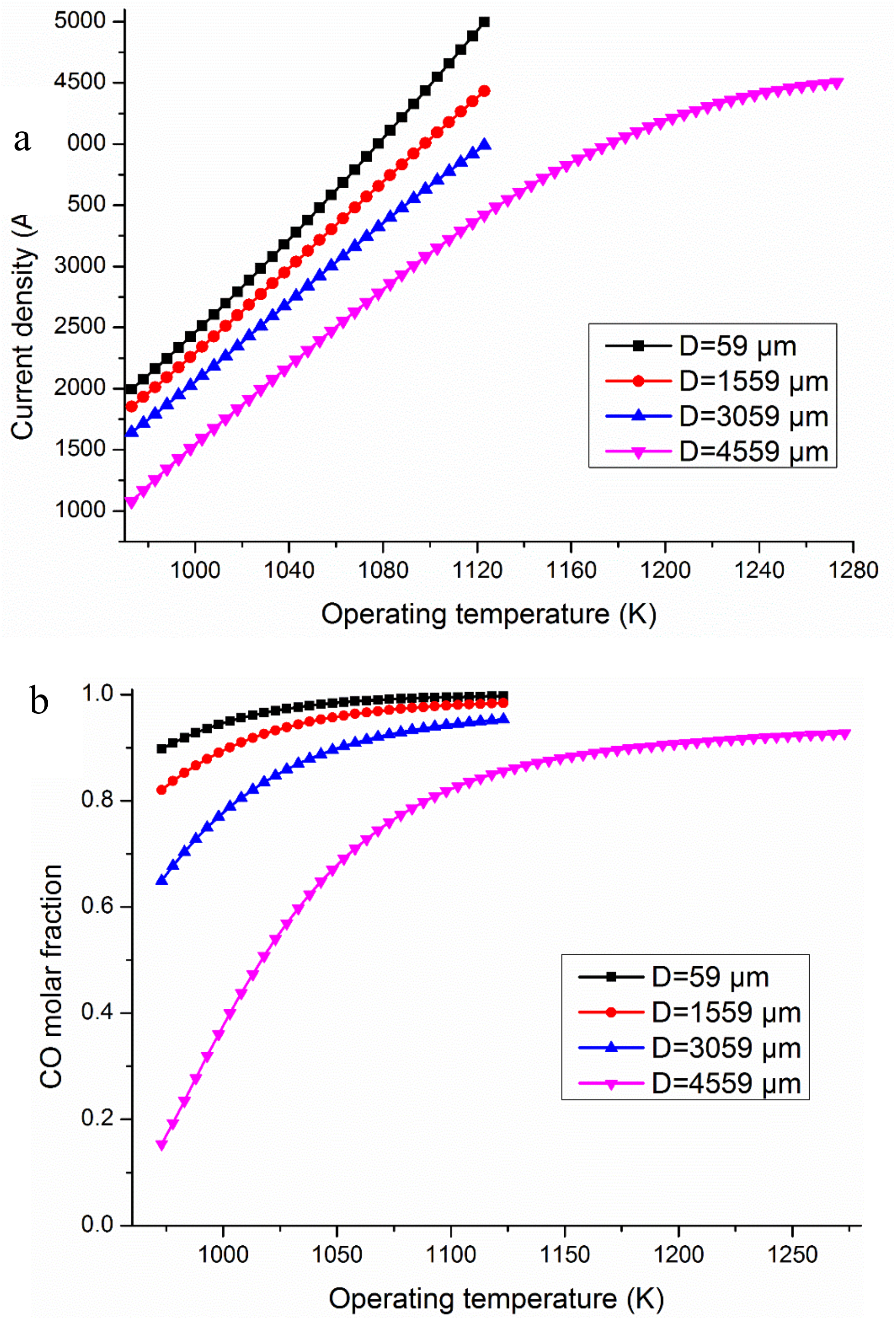

Figure 2.6 Effect of temperature on (a) output current density, (b) anode outlet CO molar fraction at 0.7 V operating potential and different D_{ce} cases.

2.3.4 Comparison between electrolyte-supported and anode-supported DC-SOFC

In Liu et al.' work and in the above simulations, the electrolyte-supported configuration is employed for the DC-SOFC. However, previous studies on SOFC suggested that the anode-supported configuration could offer better cell performance due to the greatly reduced ohmic loss and the only slightly increased concentration loss. As the gas diffusion in the DC-SOFC is more complicated and is coupled with the Boudouard reaction, whether the anode-supported configuration is still the optimal configuration for DC-SOFC and how much performance improved can be achieved are still unknown. In this section, the performance of DC-SOFC with the anode-supported configuration is studied and compared with the electrolyte-supported case.

The schematic of anode supported DC-SOFC can be seen in Fig. 2.1 (b) and the detailed operating conditions are shown in Table 2.7.

Table 2.7 Operation parameters for anode supported DC-SOFC

Parameter	**Value**	**Unit**
Operating potential	0.2 – 0.9	V
Anode inlet gas flow rate	0	
Distance between anode chamber and electrode, D_{ce}	59, 4559	µm
Cathode inlet gas flow rate	10	SCCM
Cathode gas composition	Air	
Temperature	1123	K

The performance comparison between the electrolyte-supported DC-SOFC and the anode-supported DC-SOFC is shown in Fig. 2.7. The performance of the anode-supported DC-SOFC is much better than that of the electrolyte-supported DC-SOFC. This result means that the decrease in ohmic loss of the electrolyte is greater than the increase in concentration overpotential in the anode-supported DC-SOFC. In addition, it can be seen from Fig. 2.8a that CO concentration from the anode-supported DC-SOFC is still very high even at large current density (27500A m^{-2}) when D_{ce} is small

(59µm). However, CO concentration in anode is substantially decreased to be below 0.8 (Fig. 2.8b) when D_{ce} is large (4559µm) and the operating potential is small (0.2A). The results mean that the anode-supported configuration is beneficial to the electrical power output of the DC-SOFC but not favorable for CO generation. To improve the CO generation, a small D_{ce} and a relative high operating potential are recommended in anode-supported DC-SOFC.

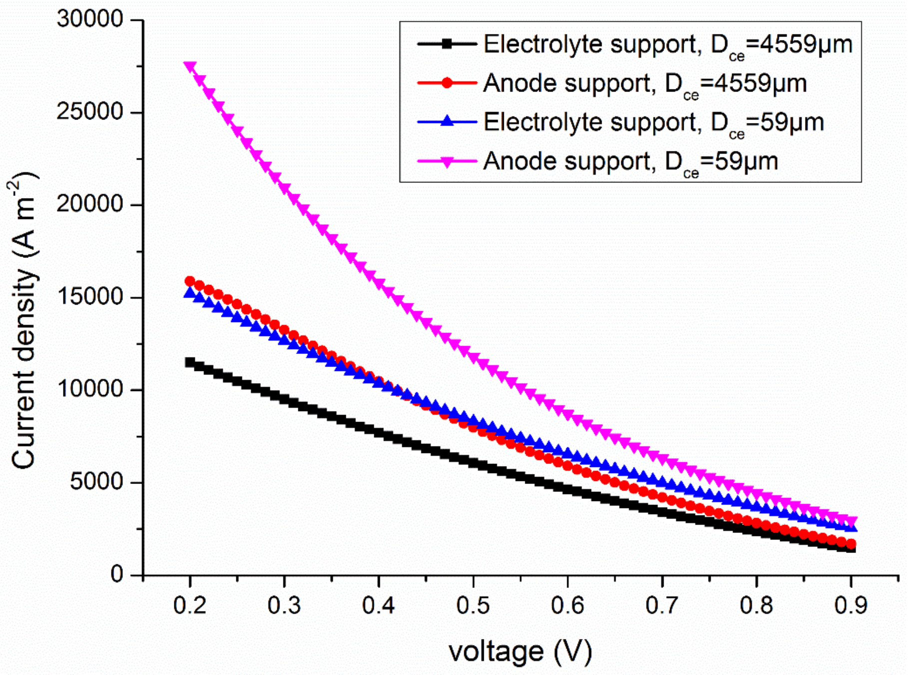

Figure 2.7 Performance comparison between electrolyte-supported and anode-supported DC-SOFCs at different D_{ce}

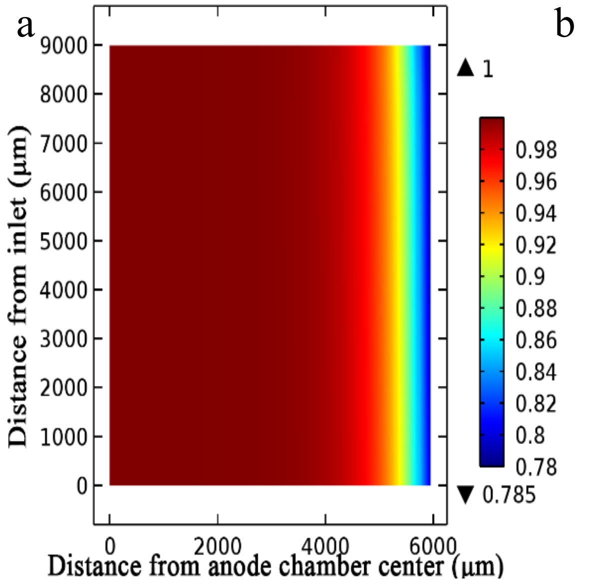
a
b
Distance from inlet (μm)
9000
8000
7000
6000
5000
4000
3000
2000
1000
0
0
2000
4000
6000
Distance from anode chamber center (μm)
▲ 1
0.98
0.96
0.94
0.92
0.9
0.88
0.86
0.84
0.82
0.8
0.78
▼ 0.785

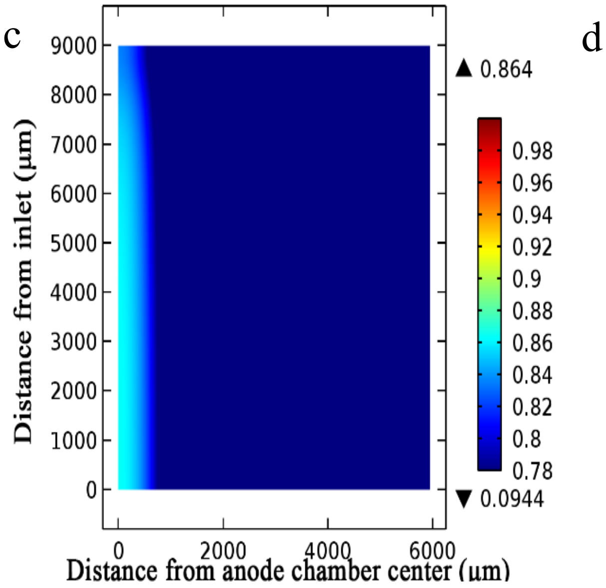
c
d
Distance from inlet (μm)
9000
8000
7000
6000
5000
4000
3000
2000
1000
0
0
2000
4000
6000
Distance from anode chamber center (μm)
▲ 0.864
0.98
0.96
0.94
0.92
0.9
0.88
0.86
0.84
0.82
0.8
0.78
▼ 0.0944

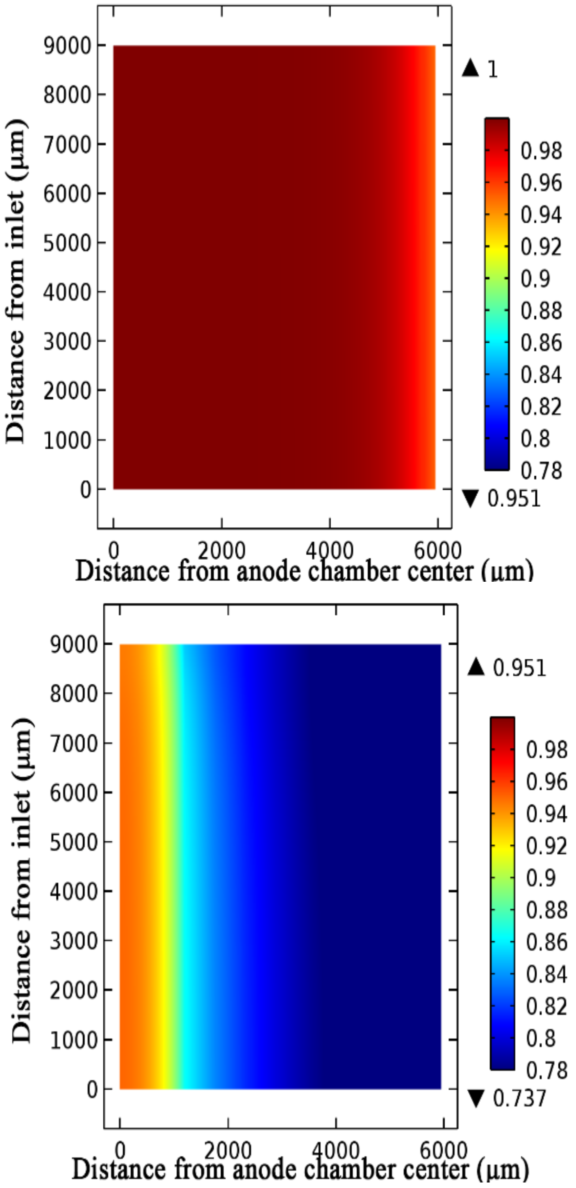

Figure 2.8 Effect of operating potential and D_{ce} on CO molar fraction distribution in anode supported DC-SOFC at 1123K: (a) $D_{ce} = 59\ \mu\mathrm{m},\ \mathrm{V} = 0.2\mathrm{V}$ (b) $D_{ce} = 4559\ \mu\mathrm{m},\ \mathrm{V} = 0.2\mathrm{V}$ (c) $D_{ce} = 59\ \mu\mathrm{m},\ \mathrm{V} = 0.7\mathrm{V}$ (c) $D_{ce} = 4559\ \mu\mathrm{m},\ \mathrm{V} = 0.7\mathrm{V}$

2.4 Conclusions

A multi-physics model considering electrochemical reaction, chemical reactions, ionic/electronic charge transport, mass transport and momentum transport is developed to characterize the performance of a tubular DC-SOFC. The model is validated by comparing the simulation results with experimental data by Liu's group [138]. Parametric simulations are conducted to evaluate the effects of distance between the carbon chamber and the porous anode on DC-SOFC performance. In addition, the temperature effect on DC-SOFC performance and the CO generation characteristics of the DC-SOFC are also studied.

It is found that the distance between carbon chamber and anode electrode D_{ce} could affect the performance of DC-SOFC to some extent. As D_{ce} is increased, the performance of DC-SOFC decreases. However, it is also observed that the performance of DC-SOFC with large D_{ce} is still good enough, indicating that the practical and large-scale DC-SOFC applications could be feasible.

The operating temperature significantly affects the DC-SOFC performance. At a high temperature, the molar fraction of CO at the outlet of DC-SOFC is high and it is feasible to convert the carbon fuel for electricity and CO co-generation. However, at a lower operating temperature, both the average current density and the CO molar fraction at the DC-SOFC outlet are decreased, primarily due to the low Boudouard reaction rate. This study clearly demonstrates the feasibility of controlling the CO generation from DC-SOFC for CO and electricity co-generation.

Compared with gaseous fuel-fed SOFC, the current density of DC-SOFC is found to slightly increase along the cell length, due to the generation of electrochemical fuel along the cell length by the Boudouard reaction.

Electrolyte-supported and anode-supported DC-SOFCs are also compared to understand the effects of support-type on the electrical power output and CO generation characteristics. It is found that an anode-supported DC-SOFC has a much better electrical power output than that of an electrolyte-supported DC-SOFC. However, the anode-supported configuration is not favorable for CO generation, especially at a largeD_{ce}. To improve CO generation, small D_{ce} and relatively higher operation potential are recommended for an anode-supported DC-SOFC.

The present model can be used for subsequent thermodynamic analysis for system design optimization.

Overall, the study results in this chapter show the attractive possibility for gas and electricity cogeneration with DC-SOFCs. This kind of SOFC uses cheap fuel (solid carbon) to generate both CO and electricity, which has great economy advantageous. The modeling results also indicate that a higher temperature, smaller D_{ce} and anode support SOFC is more favorable in real applications. The good performance of DC-SOFC at large D_{ce} further suggests its application in industry.

3. CHAPTER 3 THE THERMAL EFFECT IN DIRECT CARBON SOLID OXIDE FUEL CELLS

3.1 Introduction

In last chapter, the characteristics of DC-SOFCs in electricity power and CO cogeneration have been analyzed by assuming a uniform temperature distribution due to the small cell size. The key reactions in the DC-SOFC are Boudouard reaction (endothermic) and CO electrochemical oxidization (exothermic). The different thermal features of these two reactions brings a quite different thermal impact to the cell especially at a larger scale. Considering that the temperature distribution in DC-SOFCs not only affects the chemical reaction and electrochemical reaction of the cells, but also affects the life time of DC-SOFCs due to the heat management and thermal stress. In this chapter, the previously developed model is extended to study the thermal effects on the DC-SOFC temperature distribution.

3.2 Model development

3.2.1 Model assumption and calculation domain

A 2D numerical model including the electrochemical and chemical reactions, ionic/electronic charge transport, mass/momentum transport and heat transfer is developed for a tubular DC-SOFC. This model is an extension from our previous work [17], which has been well validated. Compared with our previous work, cell length in this model has been extended from 9mm to 90mm, and thermal effect has also been considered to investigate the cell temperature distribution.

The schematic of the electrolyte supported tubular DC-SOFC is shown in Fig. 3.1(a). Carbon fuel is supplied to the anode chamber and air is supplied to the cathode channel. Initial CO/CO_2 comes from the reactions between carbon fuel and initial O_2 in the anode chamber. CO molecules produced in anode chamber diffuse into the porous anode electrode and react with O^{2-} through electrochemical reaction at TPB sites where CO_2 molecules are then formed and electrons are released. After that, the produced CO_2 molecules in anode electrode diffuse back to the chamber and react with solid carbon to produce more CO molecules through Boudouard reaction. These processes repeat continuously between the anode chamber and the anode electrode to maintain CO/CO_2 cycling while generating electricity, related formulas are shown in Eqs. (3.1-3.5).

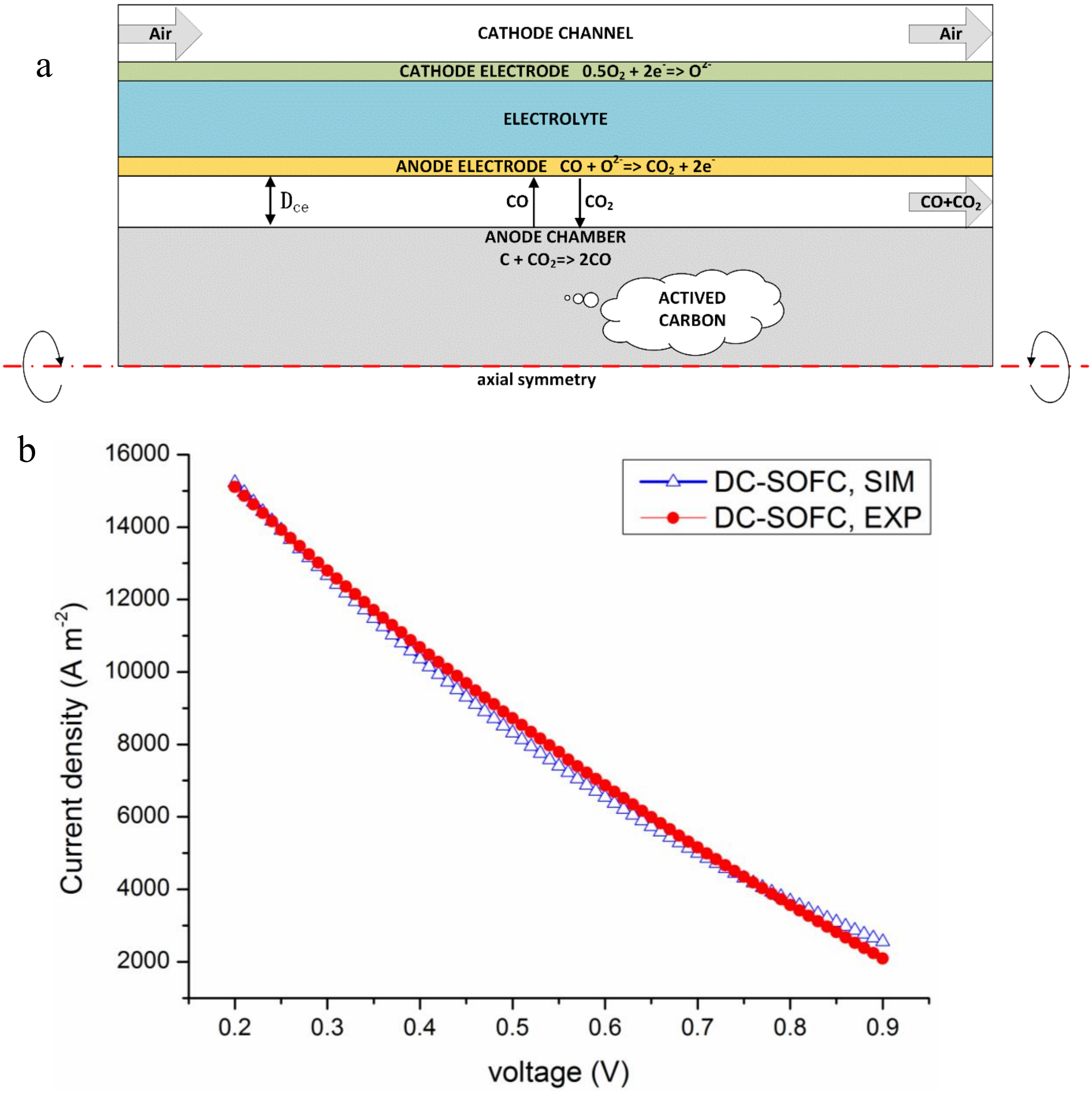

Figure 3.1 Schematic of the electrolyte supported DC-SOFC(a) and model validation for DC-SOFC.

The main assumptions in this model are shown as below.

(1) The electrochemical reactions take place on TPBs, which are assumed to be uniformly distributed in the whole porous electrodes. The two conducting phases (electronic and ionic) in the porous electrodes are continuous and homogeneous.

(2) The ionic and electronic charge transport processes take place in the PEN assembly.

(3) All gases (CO, CO_2, O_2 and N_2) are ideal gases. The gas flow is incompressible.

(4) The volume of activated carbon fuel in the anode chamber does not change in the steady state model.

(5) Thermal radiation is assumed to be negligible.

3.2.2 Heat transfer model

This model is developed based on the model in last chapter, apart from the governing equation introduced in Chapter 2, heat transfer model is also included.

In DC-SOFCs, electrochemical reactions in TPB sites generates heat while the chemical reaction (Boudouard reaction) in anode chamber consumes heat. This will not only result in the gradient of temperature along the cell length, but also along the cell width. General heat balance equation is used to describe the heat transfer in the cell as:

$$\rho C_p u \cdot \nabla T + \nabla \cdot \left(-\lambda_{eff} \nabla T\right) = Q \qquad (3.1)$$

where C_p is the fluid heat capacity at constant pressure, u is the fluid velocity field, λ_{eff} is the effective thermal conductivity and Q is the heat source. In the porous structure of electrodes, λ_{eff} can be calculated as:

$$\lambda_{eff} = (1 - \varepsilon)\lambda_s + \varepsilon\lambda_l \qquad (3.2)$$

where λ_s and λ_l are heat conductivity of solid and liquid phase, respectively. Value of above material property parameters are listed in Table 3.1.

Table 3.1 Material thermodynamic properties [139]

Parameters	**Value**	**Unit**
Thermal conductivity		

Carbon	1.59	W $m^{-1}K^{-1}$
Electrode	13.54	W $m^{-1}K^{-1}$
Electrolyte	2.7	W $m^{-1}K^{-1}$
Specific heat capacity		
Carbon	887.5	J $kg^{-1}K^{-1}$
Electrode	390	J $kg^{-1}K^{-1}$
Electrolyte	300	J $kg^{-1}K^{-1}$
Density		
Carbon	1700	kg m^{-3}
Electrode	6870	kg m^{-3}
Electrolyte	2000	kg m^{-3}

3.2.3 Boundary conditions

The electric potentials are specified at the outer boundaries of cathode and anode as working potential and zero potential, respectively. The insulation condition is applied to the bottom and top of the cell.

Inflow gas mole fraction is specified at the inlet of the cathode. The convective flux boundary condition is specified at the outlets of the cathode and anode. Zero flux is assumed at the end of anode chamber, electrolyte/electrode interface and the ends of electrodes.

Standard gas flow rate (SCCM) is specified at the cathode while pressure condition is specified at the outlet. No-slip condition is applied to the end of anode chamber, electrolyte/electrode interface and the ends of electrodes.

Thermal insulation condition is applied to the outer boundary of cathode chamber, the end of anode chamber and the ends of electrodes and electrolyte. Gas temperature is specified at the cathode inlet.

3.2.4 Model parameters

The values of material thermal properties and tuning parameters are summarized in Table 3.1 and Table 3.2, more detailed information can be found in Chapter 2. In the parametric simulations, the parameters are varied to evaluate their effects on the DC-SOFC performance, detailed operating parameters are listed in Table 3.3 to Table 3.5.

Table 3.2 Model tuning parameters

Parameter	**Value**	**Unit**
Cathode tortuosity	3	
Anode tortuosity	3	
O_2 exchange current density i_{O_2}	400	Am^{-2}
CO exchange current density, i_{CO}	450	Am^{-2}
CO charge transfer coefficient, α_{CO}	0.5	
O_2 charge transfer coefficient, α_{O_2}	0.5	
Equilibrium constant of Boudouard reaction	$6 \times 10^{13} \cdot \frac{T-973}{150}$	1/s

3.2.5 Model solution

The model is solved at certain cell potential, inlet gas flow rate and inlet gas temperature. The output of the model is mainly the temperature distribution. The calculations are performed using the finite element commercial software COMSOL MULTIPHSICS®.

3.3 Results and discussion

3.3.1 Model validation

This model is an extension of our previous model, which has already been validated by comparing the simulation results and experimental data from the literature as shown in Fig. 3.1(b). More detailed information about the model validation can be found in Chapter 2.

3.3.2 Effect of applied voltage

The relationship between operating potential, current density and average electrolyte temperature at given operating conditions are shown in Fig. 3.2. The detailed operating conditions are listed in Table 3.3.

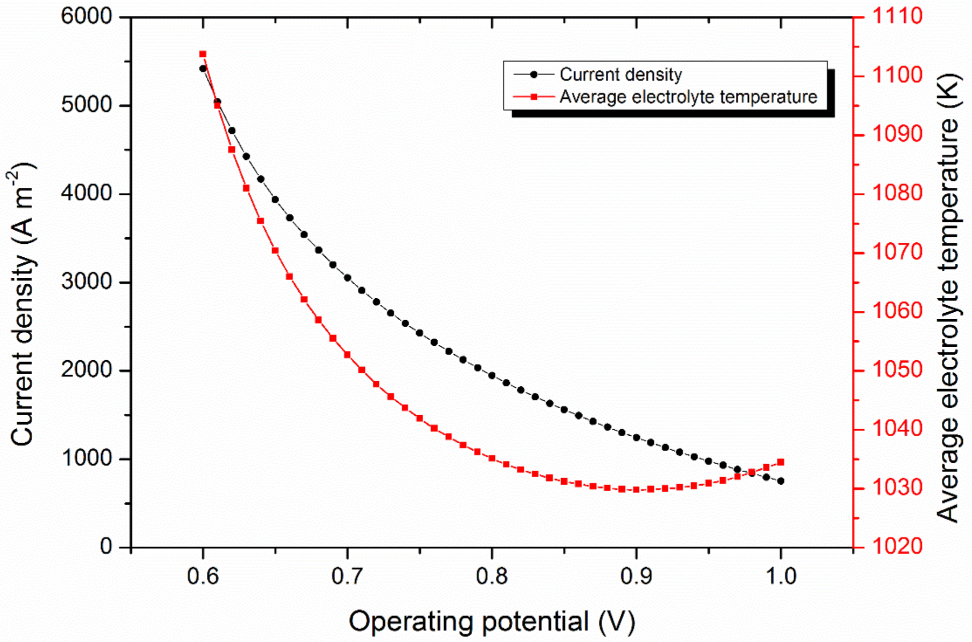

Figure 3.2 Effect of operating potential on cell current density and temperature

Table 3.3 Operation parameters for operating potential effect study in DC-SOFC

Parameter	Value	Unit
Operating potential	0.6 – 1.0	V

Anode inlet gas flow rate	0	
Cathode inlet gas flow rate	400	SCCM
Cathode gas composition	Air	
Cathode inlet gas temperature	1073	K

As can be seen in Fig. 3.2, when operating potential decreases from 1.0 V to 0.6 V, the cell current density increases from 754 A m^{-2} to 5417 A m^{-2}. The average electrolyte temperature decreases slightly when the operating potential decreases from 1035 K at 1.0 V to 1029 K at 0.9 V and increases quickly to 1104 K at 0.6 V. The electrochemical reaction rate and overpotential losses are higher at a lower operating potential, leading to more heat generation. However, more CO_2 can be generated at a higher current density, which in turn leads to a higher rate of the endothermic Boudouard reaction and more heat consumption in the anode chamber. These combined effects result in the slightly temperature decrease when operating potential decreases from 1.0 V to 0.9 V. With a further decrease of operating potential from 0.9 V to 0.6 V, the temperature of DC-SOFC is increased substantially, indicating that the heat generation from the electrochemical reactions and overpotential losses is higher than heat consumption by Boudouard reaction.

The temperature distribution of the DC-SOFC is shown in Fig. 3.3. At an operating potential of 1.0 V, the temperature decreases along the DC-SOFC length and the peak temperature occurs at the cathode inlet. While at an operating potential of 0.6 V, the temperature increases along the cell length and the peak temperature occurs at the cathode outlet. The different temperature distribution patterns are caused by the electrochemical and chemical processes in the DC-SOFC. At a high operating potential, the heat generation from electrochemical reaction and overpotential losses is lower than heat consumption by endothermic Boudouard reaction, leading to a decrease of cell temperature. While at a relatively lower operating potential, exothermic processes are greatly enhanced due to increased current density, which in turn increase the temperature of DC-SOFC.

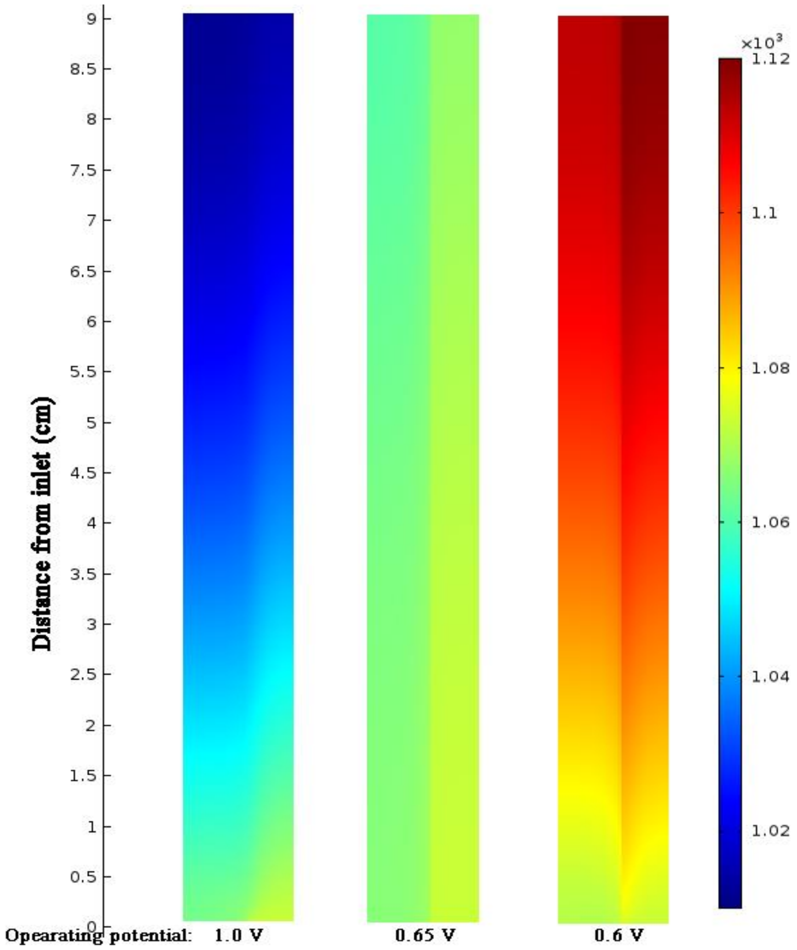

Figure 3.3 Cell temperature distribution at 1.0 V, 0.65 V and 0.6 V operating potential.

The temperature of the anode temperature is found to be always lower than the cathode temperature at the same cell length position, as endothermic Boudouard reaction takes place in the anode chamber. It is important to point out that the temperature distribution of the DC-SOFC is almost uniform at an operating potential of about 0.65V. For long-term and stable operation DC-SOFC, the uniform temperature distribution is desirable to reduce the thermal stress in the cell. The results of the present study clearly demonstrate that the temperature uniformity of DC-SOFC can be achieved by controlling the operating conditions.

Fig. 3.4. shows a breakdown on heat generation/consumption from different components in the cell. It can be seen that the porous anode and the anode chamber contribute most to the heat generation and consumption, respectively. At an operating potential of 1.0 V, the heat consumption by Boudouard reaction in the anode chamber is slightly higher than the heat generation from electrochemical reaction and overpotential losses, which well explains the thermal effect in Fig. 3.3. In the porous anode, the entropy change due to electrochemical reaction contributes to over 90% of heat generation in the anode while activation loss in anode contributes to about 9.85%. At an operating potential of 0.6, both the heat generation and heat consumption are substantially enhanced and the heat generation from electrolyte and the cathode are not negligible. The total heat generation is found to be higher than the heat consumption, again in consistence with the results in Fig. 3.3. Compared with the 1V case, the anode activation loss contributes to about 29% of the total heat generation in the anode at 0.6V. The results suggest that the heat generation/consumption in the anode is the key for controlling the temperature field of DC-SOFC. Thus it is possible to adjust the operating parameters to control the chemical and electrochemical processes in the anode to control the temperature distribution in DC-SOFC.

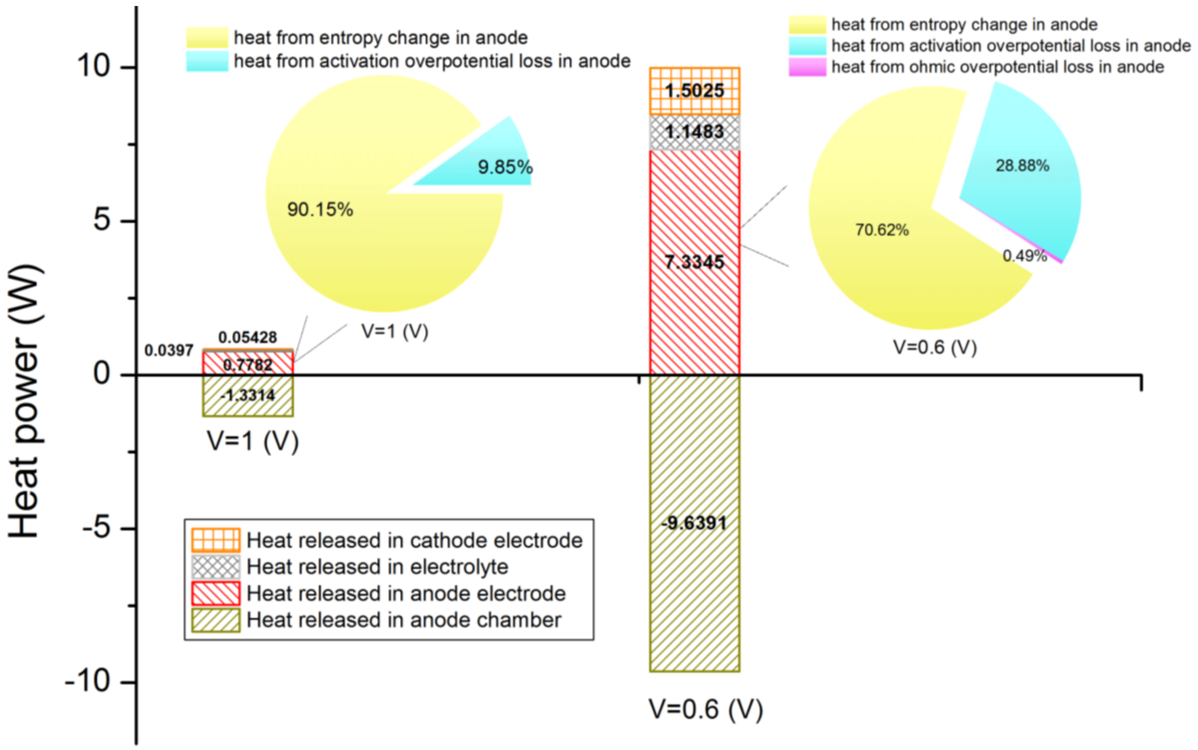

Figure 3.4 Breakdown of heat power from different components in the cell

3.3.3 Effect of cathode inlet gas temperature

Inlet gas temperature will also affect the temperature distribution in the cell. Detailed operating parameters are listed in Table 3.4.

Table 3.4 Operation parameters for cathode inlet gas temperature effect study in DC-SOFC

Parameter	**Value**	**Unit**
Operating potential	0.6 – 1.0	V
Anode inlet gas flow rate	0	
Cathode inlet gas flow rate	400	SCCM
Cathode gas composition	Air	
Cathode inlet gas temperature	1023 - 1173	K

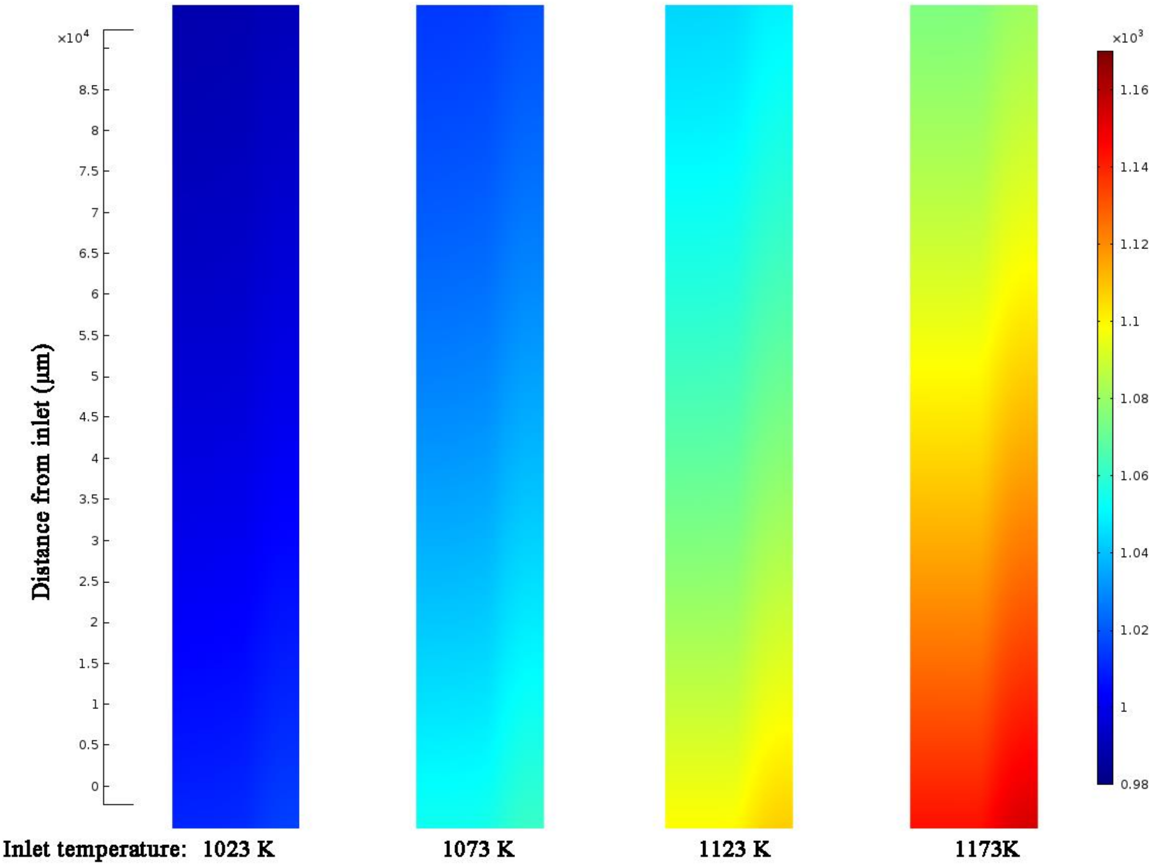

Figure 3.5 Cathode inlet gas temperature effects on cell temperature distribution at 1.0 V

As shown in Fig. 3.5, at a potential of 1 V, cell temperature decreases from inlet to outlet along the cell length at cathode inlet gas temperature from 1023K to 1173K. It can also be found from Fig. 3.5 that the temperature gradient along the cell length increases with increasing cathode inlet gas temperature. As shown in Fig. 3.6(a), when the operating potential is 0.6V, cell temperature increases from inlet to outlet along the cell length. However, it should also be noted that when cell operates with a relative high cathode inlet gas temperature (1123 K), the peak temperature could occur at the middle of the DC-SOFC. This is because electrochemical reaction rate is very high at a high temperature and low operating potential and oxygen is almost exhausted in the cathode channel (Fig. 3.6(b)), resulting in nearly zero electrochemical reaction and no heat generation in the end of the DC-SOFC. For comparison, the rate of endothermic chemical reaction is still high throughout the anode chamber, decreasing the temperature of DC-SOFC in the downstream.

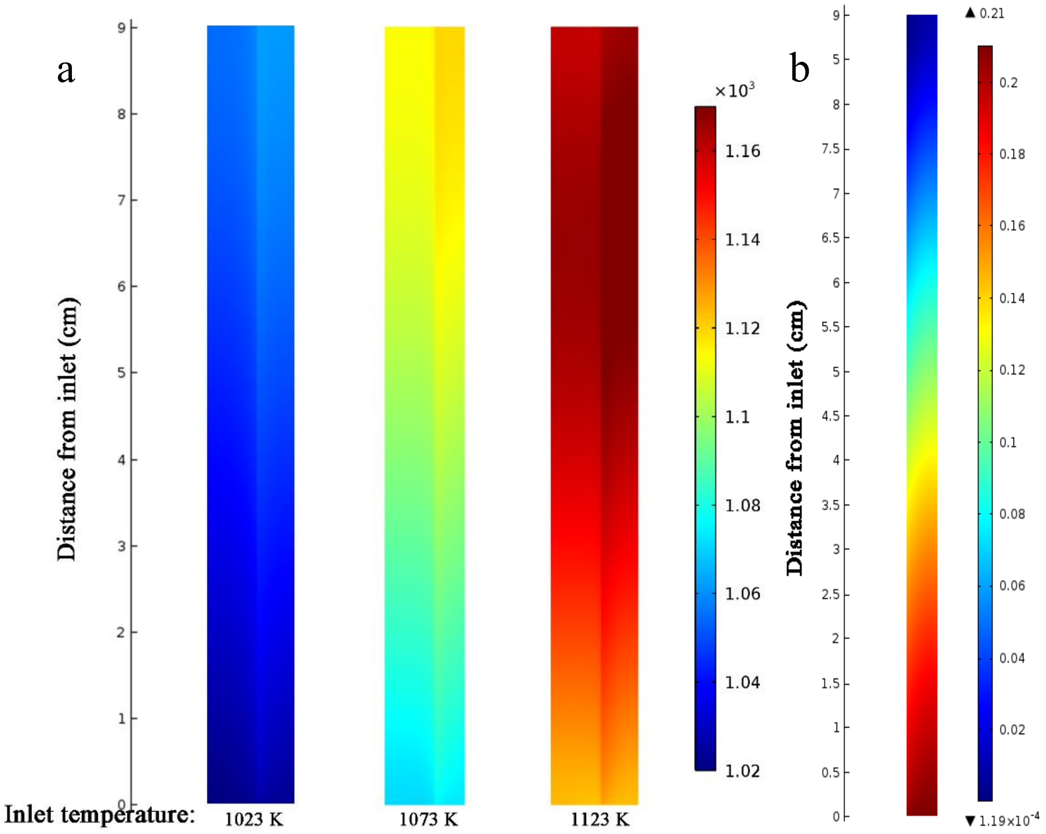

Figure 3.6 Cathode inlet gas temperature effects on cell temperature distribution at 0.6 V operating potential (a) and cathode O_2 molar fraction (b) with 1123 K inlet gas temperature.

3.3.4 Effect of distance between carbon and anode electrode

Previous study has shown how the distance between carbon fuel and anode electrode (D_{ce}) will affect the performance of DC-SOFC [140]. As the thermal conductivity of gas is much smaller than that of solid carbon, the increase of D_{ce} will surely increase the variation of temperature in the cell. Thus the effect of D_{ce} on the temperature distribution of the cell is discussed, detailed operating parameters are listed in Table 3.5.

Table 3.5 Operation parameters for D_{ce} effect study in DC-SOFC

Parameter	**Value**	**Unit**
Operating potential	0.6 - 1	V
Distance between anode chamber and electrode, D_{ce}	59 - 2059	μm
Anode inlet gas flow rate	0	
Cathode inlet gas flow rate	400	SCCM
Cathode gas composition	Air	
Cathode inlet gas temperature	1073	K

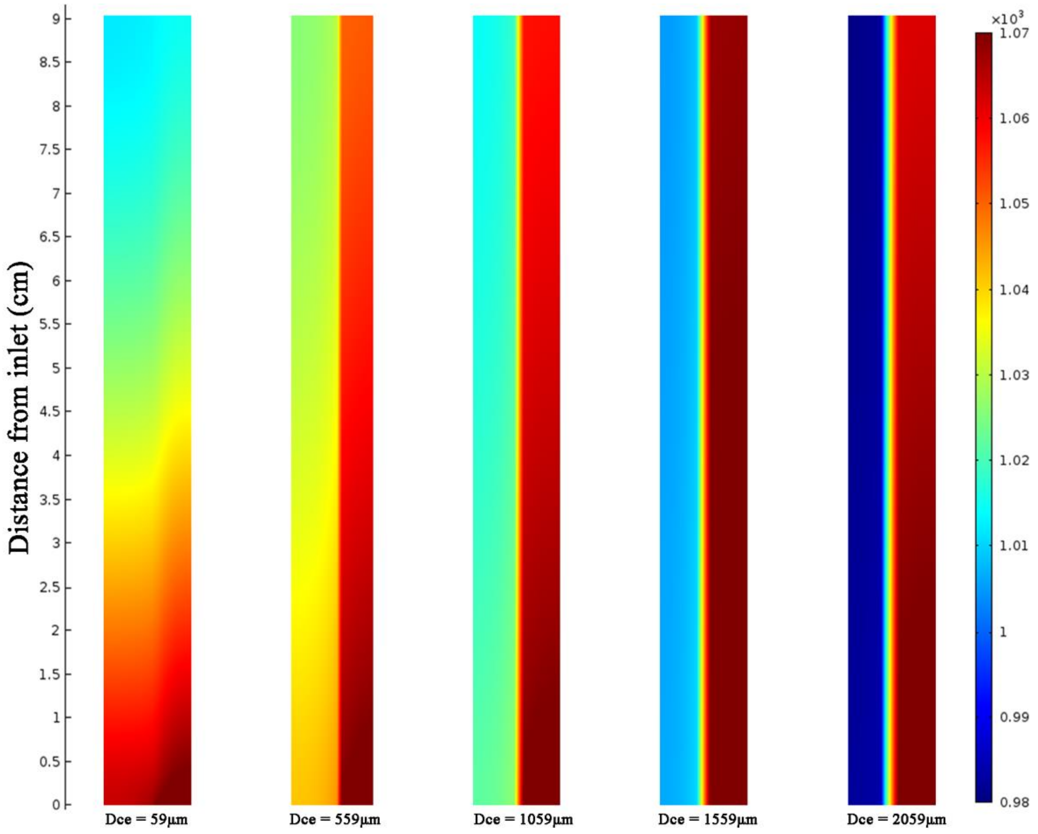

Figure 3.7 Effects of D_{ce} on the temperature distribution in the cell with 1073K cathode inlet gas temperature and 0.7 V operating potential

Fig. 3.7 shows the effects of D_{ce} on the temperature distribution in the cell with 1073K cathode inlet gas temperature and 0.7 V operating potential. Distance between carbon and anode electrode surface varies from 59 μm to 2059 μm in this study. As can be seen from Fig. 3.7, when D_{ce} is quite small (59 μm), the gradient along the cell width is quite small. With the increase of D_{ce}, there occurs an obvious temperature boundary between solid carbon and anode gas channel and the gradient along the cell width becomes quite large.

Besides, it is observed from Fig. 3.8 that the CO molar fraction in anode decreases quickly with the increase of D_{ce}, which is due to the increased gas transport difficulty and lower chemical reaction temperature caused by larger D_{ce}. Thus, it is also important to keep a small distance between carbon fuel and anode electrode when cell is placed horizontally.

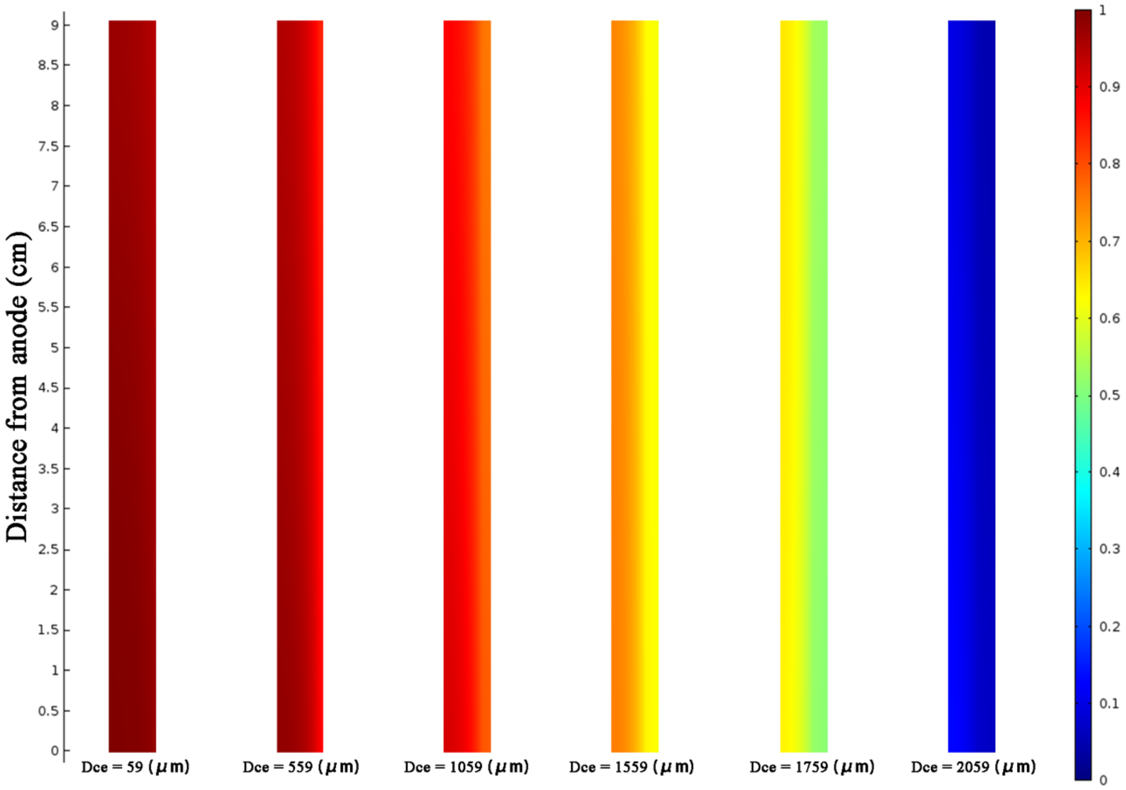

Fig. 3.8. Effects of D_{ce} on the CO molar fraction distribution in the anode with 1073K

cathode inlet gas temperature and 0.7 V operating potential

3.4 Conclusions

A multi-physics model considering electrochemical reaction, chemical reactions, ionic/electronic charge transport, mass/momentum transport and heat transfer is developed to characterize the temperature distribution of a tubular DC-SOFC. Parametric simulations are conducted to evaluate the effects of operating potential, cathode inlet gas temperature and distance between the carbon fuel and anode electrode on DC-SOFC temperature distribution.

It is found that the operating potential has a great effect on the temperature distribution of the cell. With the decrease of operating potential, the overall cell temperature increases quickly. Besides, the temperature gradient also changes from negative to positive along the cell length with the cell operating potential decreasing from 1.0 V to 0.6 V and a relative even temperature distribution of the cell is found when the operating potential is around 0.65V. It is also observed from the breakdown analysis that most of the heat is generated from anode electrode, where entropy change heat is the majority part compared with other processes.

Cathode inlet gas temperature is also found to play an important role on the temperature distribution of the cell. When the operating voltage is high (1.0 V), cathode inlet gas plays as the outer heat source and it plays as the outer heat sink when the operating voltage is low (0.6 V). It should also be noted that when the cathode inlet gas temperature is high (1123K), cathode oxygen may be exhausted in the cell, which not only causes a peak temperature point in the middle position of the cell length but also decreases cell’s electrochemical performance.

The effect of distance between carbon fuel and anode electrode on temperature distribution is also studied in this work. It is found that the temperature gradient increases quickly along the cell width with the increase of D_{ce} due to the small thermal conductivity of the gas.

4. CHAPTER 4 MODELING OF DIRECT CARBON SOLID OXIDE FUEL CELLS WITH H_2O AND CO_2 AS GASIFICATION AGENTS

4.1 Introduction

The systems studied in Chapter 2 to Chapter for use CO_2 and the carbon gasification agent in anode chamber. Catalysts are necessary in these systems because of the slow Boudouard reaction rate. However, the pre-process of solid carbon for catalyst mixture is complex, which results in additional fuel cost. H_2O is regarded as an alternative gasification agent due to its fast carbon gasification reaction rate. Therefore, H_2O is adopted as the gasification agent in this chapter for experiment conduction and model development.

4.2 Model development

4.2.1 Model assumption and calculation domain

2D mathematical models are developed to simulate the chemical/electrochemical reaction, ion/electron transport and mass/momentum transport in DC-SOFCs with CO_2 and H_2O as agents. The schematics of the CO_2 assisted DC-SOFC and H_2O assisted DC-SOFCs are shown in Fig. 4.1. Solid carbon is placed in the anode chamber and H_2O (or CO_2) is also supplied to the anode. Solid carbon in anode chamber is very close to the porous anode. The surface area of button cell is 0.45 cm^2.The thickness of anode, electrolyte and cathode are 400μm, 8μm and 24μm, respectively.

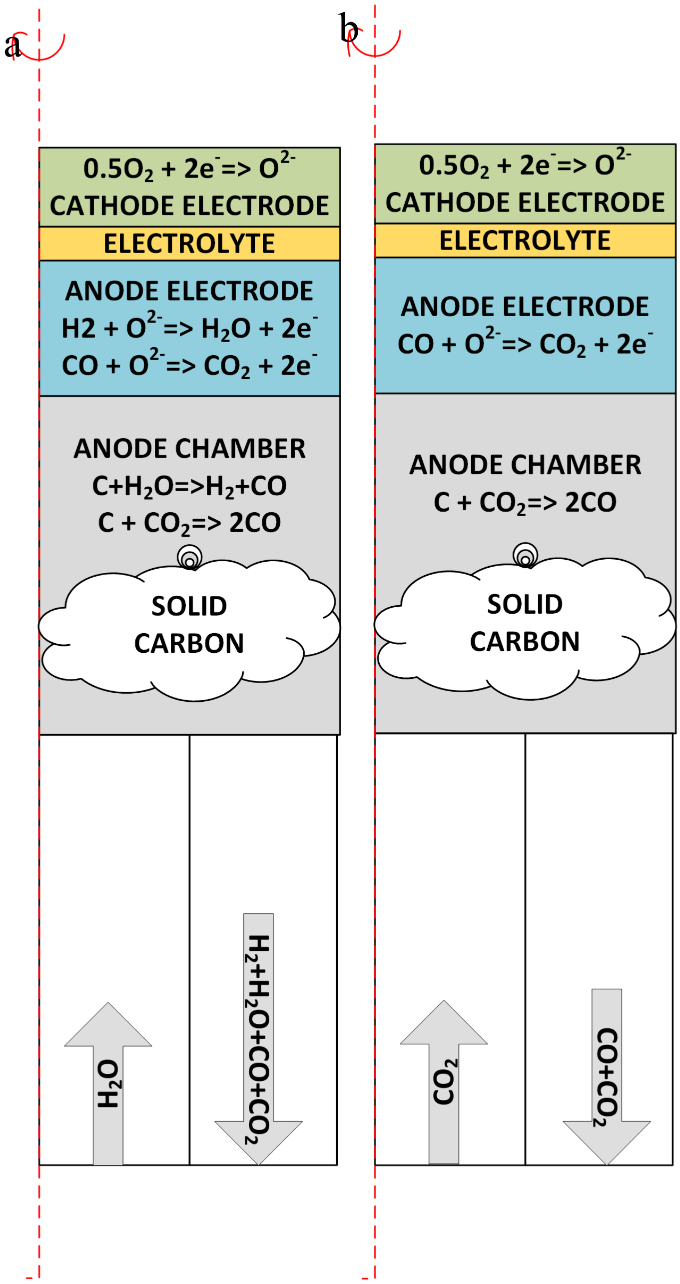

Figure 4.1. Schematic of H_2O assisted DC-SOFC(a) and CO_2 assisted DC-SOFC (b).

Model assumptions are as follows:

(1) In H_2O assisted DC-SOFCs, H_2 and CO both participate in the electrochemical reactions and share the TPB sites, which is proportional to their relative local concentration.

(2) TPBs are distributed uniformly in the whole porous electrode. Both ionic- and electronic- conducting phases in the porous electrodes are homogeneous and continuous.

(3) Gases in the model (CO, H_2O, H_2, O_2, N_2) are ideal gases and incompressible gas flow in the gas channels.

(4) Temperature distribution in the cell is uniform due to its small size.

(5) The volume of carbon fuel in the anode chamber does not change with time.

4.2.2 Governing equations

4.2.2.1 Chemical reactions

When using CO2 as gasification agent in DC-SOFCs, Boudouard reaction plays a key role as it produces CO to maintain the electrochemical reaction. This key reaction (Eq. (4.1)) converts carbon and CO_2 into CO. Here solid carbon is the energy source and CO is an energy carrier that transports the chemical energy from solid carbon to the anode TPB. The reaction rate of Boudouard reaction is calculated as Eq. (4.2)[141]

$$C + CO_2 \leftrightarrow 2CO \tag{4.1}$$

$$R_{C\_CO2} = \frac{K_1 p_{CO_2}}{1+K_2 p_{CO}+K_3 p_{CO_2}} \tag{4.2}$$

When H_2O is added in DC-SOFCs, the main chemical reaction rate in anode chamber becomes water gasification reaction (Eq. (4.3)) instead of Boudouard reaction as water gasification has a much higher reaction rate. The reaction rate of water gasification reaction is calculated as Eq. (4.4)

$$C + H_2O \leftrightarrow CO + H_2 \tag{4.3}$$

$$R_{C\_H2O} = \frac{K_4 p_{H_2O}}{1+K_5 p_{H_2}+K_6 p_{H_2O}} \tag{4.4}$$

Besides, WGSR catalyzed by nickel in anode electrode also plays an important role as shown in Eq. (4.5). This reaction converts CO into H_2 and ensures H_2 to mainly participate in electrochemical reaction. The Reaction rate of WGSR is calculated by Eqs. (4.6-4.9).[142]

$$CO + H_2O \leftrightarrow CO_2 + H_2 \tag{4.5}$$

$$R_{WGSR} = k_{sf}(p_{H_2O}p_{CO} - \frac{p_{H_2}p_{CO_2}}{K_{ps}}) \tag{4.6}$$

$$k_{sf} = 0.0171\exp(\frac{-103191}{RT})\ (\text{mol m}^{-3}\ \text{Pa}^{-2}\ \text{s}^{-1}) \tag{4.7}$$

$$K_{ps} = \exp(-0.2935Z^3 + 0.6351Z^2 + 4.1788Z + 0.3169 \tag{4.8}$$

$$Z = \frac{1000}{T} - 1 \tag{4.9}$$

Overall, in H_2O assisted DC-SOFCs, water gasification reaction becomes the key chemical reaction instead of Boudouard reaction. This change ensures a faster gas fuel supplement and brings in H_2 in the fuel cell. WGSR in anode electrode largely improves the percentage of H_2 component in gas fuel and makes H_2 as the main intermediate between solid fuel and anode electrode. Faster gas fuel production rate and better electrochemical reaction activity are thus achieved by introducing H_2O into DC-SOFCs.

4.2.2.2 Electrochemical reaction

In CO_2-assisted DC-SOFCs, CO is the only fuel to be electrochemically oxidized. While in H_2O-assisted DC-SOFCs, both H_2 and CO will be produced in chemical reactions and participate in the electrochemical reactions.

As air is supplied to the cathode of SOFC, O_2 molecules are reduced to form oxygen ions (O^{2-}) via Eq. (4.10)

$$O_2 + 4e^- \rightarrow 2O^{2-} \tag{4.10}$$

The oxygen ions flow through the ionic-conducting electrolyte to the anode, where they react electrochemically with CO/H_2 molecules, form CO_2/H_2O and release electrons as shown in Eq. (4.11) and Eq. (4.12):

$$CO + O^{2-} \rightarrow CO_2 + 2e^- \tag{4.11}$$

$$H_2 + O^{2-} \rightarrow H_2O + 2e^- \tag{4.12}$$

The operating potential can be calculated by thermodynamic equilibrium potential and operating overpotential losses as shown in Eq. (4.13):

$$V = E_{eq} - \eta_{act} - \eta_{ohmic} \tag{4.13}$$

The equilibrium potential (E_{eq}) is determined by the thermodynamic property of the reaction. In CO_2-assisted DC-SOFC, as only CO participate in the electrochemical reaction, the equilibrium potential can be calculated by the Nernst equation (Eq. (4.14)).

However, for H_2O-assisted DC-SOFC, both H_2 and CO can participate in the electrochemical reaction. In the present study, the equilibrium potentials for CO fuel and H_2 fuel can be determined by Eq. (4.14) and Eq. (4.15) respectively. It should be noted that the equilibrium potentials calculated by Eq. (4.14) and Eq. (4.15) are equal at an open circuit condition. When current is extracted from DC-SOFC, the equilibrium potentials for H_2 fuel and CO fuel become different due to the different overpotential losses involved in electrochemical oxidation of H_2 fuel and CO fuel.

$$E_{CO} = E_{CO}^0 + \frac{RT}{2F}\ln\left[\frac{P_{CO}^L(P_{O_2}^L)^{1/2}}{P_{CO_2}^L}\right] \quad (4.14)$$

$$E_{H_2} = E_{H_2}^0 + \frac{RT}{2F}\ln\left[\frac{P_{H_2}^L(P_{O_2}^L)^{1/2}}{P_{H_2O}^L}\right] \quad (4.15)$$

The value of E_{CO}^0 and $E_{H_2}^0$ can be calculated by Eq. (4.16) and Eq. (4.17):

$$E_{CO}^0 = 1.46713 - 0.0004527T \text{ (V)} \quad (4.16)$$

$$E_{H_2}^0 = 1.253 - 0.00024516T \text{ (V)} \quad (4.17)$$

Butler-Volmer equation is adopted to describe the relationship between the activation overpotential and the current density as shown in Eq. (4.18).

$$i = i_0\left\{\exp\left(\frac{\alpha nF\eta_{act}}{RT}\right) - \exp\left(\frac{(1-\alpha)nF\eta_{act}}{RT}\right)\right\} \quad (4.18)$$

Considering temperature effect, i_0 can be further expressed as Eq. (4.19).

$$i_0 = \gamma \exp(-\frac{E_{act}}{RT}) \quad (4.19)$$

where γ (Am^{-2}) is the pre-exponential factor and E_{act} is the activation energy level.

The ohmic overpotential (η_{ohmic}) is caused by ionic/electronic conduction. Thus it is related to the current intensity and ionic/electronic conductivity of the cell. η_{ohmic} can be calculated by Ohm law, more detailed information can be found in Chapter 2.

4.2.2.3 Mass transport

The rate of mass transport ($N_i, mol\ m^{-3}\ s^{-1}$) in channels and porous electrodes can be calculated by the general Fick's model as shown in Eq. (4.20)[112]:

$$N_i = -\frac{1}{RT}\left(\frac{B_0 y_i P}{\mu}\frac{\partial \mathrm{P}}{\partial \mathrm{z}} - D_i^{eff}\frac{\partial(y_i\mathrm{P})}{\partial \mathrm{z}}\right)\ (i = 1, \dots, n) \quad (4.20)$$

D_i^{eff} is the overall effective diffusion coefficient of component *i* (m^2s^{-1}), which can be further calculated by Eq. (4.21) for gas diffusion in the porous electrodes [114]:

$$D_i^{eff} = \frac{\varepsilon}{\tau}\left(\frac{1}{D_{im}^{eff}} + \frac{1}{D_{ik}^{eff}}\right)^{-1} \quad (4.21)$$

D_{ik}^{eff} and D_{im}^{eff} ($m^2\ s^{-1}$) are respectively the Knudsen diffusion coefficient and molecular diffusion coefficient. It should be noted that only the molecular diffusion is considered in the gas channels as Knudsen diffusion becomes significant only when the mean-free path of the molecular species is comparable or larger than the pore size.

4.2.2.4 Momentum transport

The N-S equation including the Darcy’s term is used to describe the momentum transport of gas species in porous electrodes as shown in Eq. (4.22):

$$\rho\frac{\partial u}{\partial t}+\rho u\nabla u=-\nabla p+\nabla[\mu\left(\nabla u+(\nabla u)^{T}\right)-\frac{2}{3}\mu\nabla u\Big]-\frac{\varepsilon\mu u}{k} \quad (4.22)$$

where ρ (kg m^{-3}) is the gas density and u (m s^{-1}) is the velocity vector. When the last term on the right side is neglected, Eq. (4.21) is reduced to conventional N-S equation for momentum conservation in gas channels.

4.2.3 Boundary conditions

The electric potentials are specified at the outer boundaries of cathode and anode as working potential and zero potential, respectively. The insulation condition is applied to the bottom and top of the cell.

Inflow gas mole fraction is specified at the inlet of the cathode. The convective flux boundary condition is specified at the outlets of the cathode and anode. Zero flux is assumed at the end of anode chamber, electrolyte/electrode interface and the ends of electrodes.

Standard gas flow rate is specified at the cathode while pressure condition is specified at the outlet. No-slip condition is applied to the end of anode chamber, electrolyte/electrode interface and the ends of electrodes.

4.2.4 Model parameters

The modeled button cell uses Ni-YSZ composites (mixture of YSZ and nickel) as anode, bilayer YSZ/SDC (samaria-doped ceria) electrolyte and LSCF (lanthanum strontium cobalt ferrite) as cathode. Material properties such as ionic and electronic conductivities are listed in Table 4.1. Widely used chemical and electrochemical reaction and other tuning parameters are adopted and listed in Table 4.2.

Table 4.1 Material properties[137, 139, 143-145]

Parameters	**Value or expression**	**Unit**

Ionic conductivity		
YSZ	$3.34 \times 10^4 e^{\frac{-10300}{T}}$	Sm^{-1}
SDC	$\frac{100}{T} \times 10^{5.48077-\frac{3792.53}{T}}$	Sm^{-1}
LSCF	$\frac{100}{T} \times 10^{2.51289-\frac{3036.75}{T}}$	
Electronic conductivity		
LSCF	$\frac{100}{T} \times 10^{4.32576+\frac{1204.26}{T}}$	Sm^{-1}
Ni	$3.27 \times 10^6 - 1065.3T$	Sm^{-1}
Porosity		
Cathode	0.2	
Anode	0.6	
Anode volume fraction		
YSZ	0.4	
Ni	0.6	
S_{TPB}		
Cathode layer	2.14×10^5	m^{2}m^{-3}
Anode layer	2.14×10^5	m^{2}m^{-3}
Electrode tortuosity	3	

Table 4.2 Reaction parameters

Parameter	**Value**	**Unit**
Chemical reaction		
$\boldsymbol{K_1}$	9.32×10^{-4}	s mol kg^{-1} m^{-2}
$\boldsymbol{K_2}$	1.25×10^{-3}	Pa^{-1}
$\boldsymbol{K_3}$	3.82×10^{-5}	Pa^{-1}
$\boldsymbol{K_4}$	2.19×10^{-3}	s mol kg^{-1} m^{-2}
$\boldsymbol{K_5}$	9.88×10^{-4}	Pa^{-1}
$\boldsymbol{K_6}$	8.13×10^{-5}	Pa^{-1}
Electrochemical reaction		
γ_{H_2}	2.944×10^{10}	A m^{-2}
E_{act,H_2}	1.2×10^{5}	J mol^{-1}
γ_{O_2}	1.39×10^{9}	A m^{-2}
E_{act,O_2}	1.2×10^{5}	J mol^{-1}
γ_{CO}	1.673×10^{9}	A m^{-2}
$E_{act,CO}$	1.2×10^{5}	J mol^{-1}
α_{H_2}	0.75	
α_{CO}	0.5	

4.2.5 Model solution

The model is solved at given operating conditions such as electric potentials, temperature, inlet gas flow rate and mole fraction. The output of the model includes distributions of the electrochemical reaction rates, chemical reaction rates and mole fraction of gas species in the cell. The commercial software COMSOL MULTIPHYSICS® is employed for the numerical simulation.

4.3 Results and discussion

4.3.1 Model validation

Single cells were prepared and tested for model validation of DC-SOFCs with both CO_2 and H_2O as agents. The fuel cell employed Ni-YSZ anode-supported anode, bilayer YSZ/SDC electrolyte and LSCF cathode. For the fuel cell test, the cell was sealed onto a quartz tube by means of silver paste and silver layers were printed onto the anode and cathode surfaces for current collection. The solid carbon was fixed by asbestos in the anode chamber. A quartz tube was positioned beneath the carbon layer for introducing CO_2 and H_2O. The inlet gas flow rate of anode was set as 30 SCCM (standard conditions). 10 SCCM H_2O was carried into anode by 20SCCM N_2 in the test. The operating temperature was kept constant at 850 °C during the test. Current-voltage values were collected based on the four-terminal configuration. The schematic designs for fuel cell tests and other detailed information of the testing procedures could be found in ref.[125].

The modeling results of current-voltage characteristics for both CO_2-assisted DC-SOFCs and H_2O-assisted DC-SOFCs are compared with experimental data as shown in Fig. 4.2. The quite small difference between the modeling results and experimental data validates the present model. The same structure and tuning parameters are used in the subsequent parametric simulations.

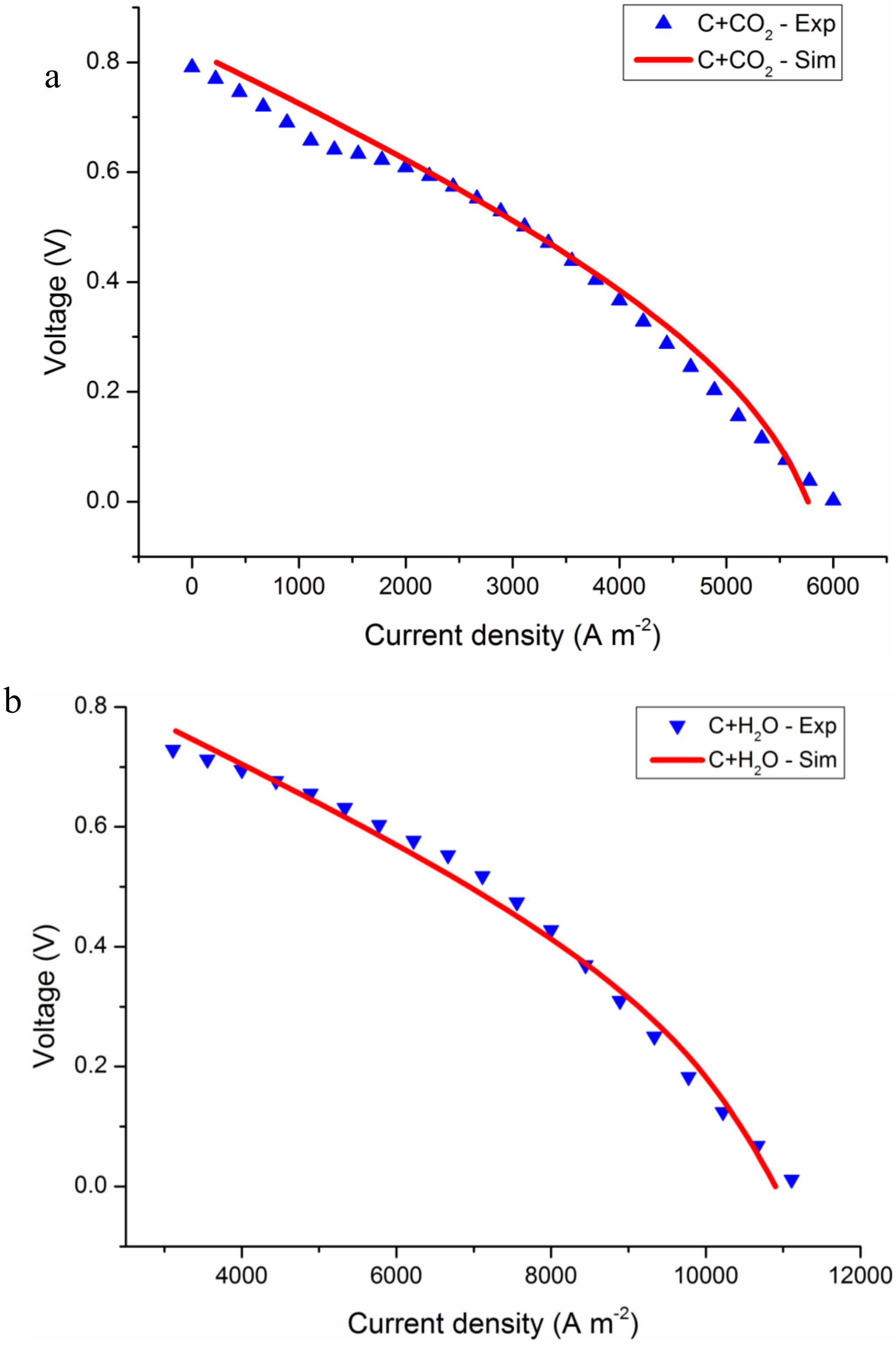

Figure 4.2 Model validation for DC-SOFCs with CO_2(a) and H_2O(b) as agents.

4.3.2 Effect of applied voltage

The voltage-current density-power density curves of DC-SOFCs with two kinds of agents are shown in Fig. 4.3. The detailed operating conditions are listed in Table 4.3.

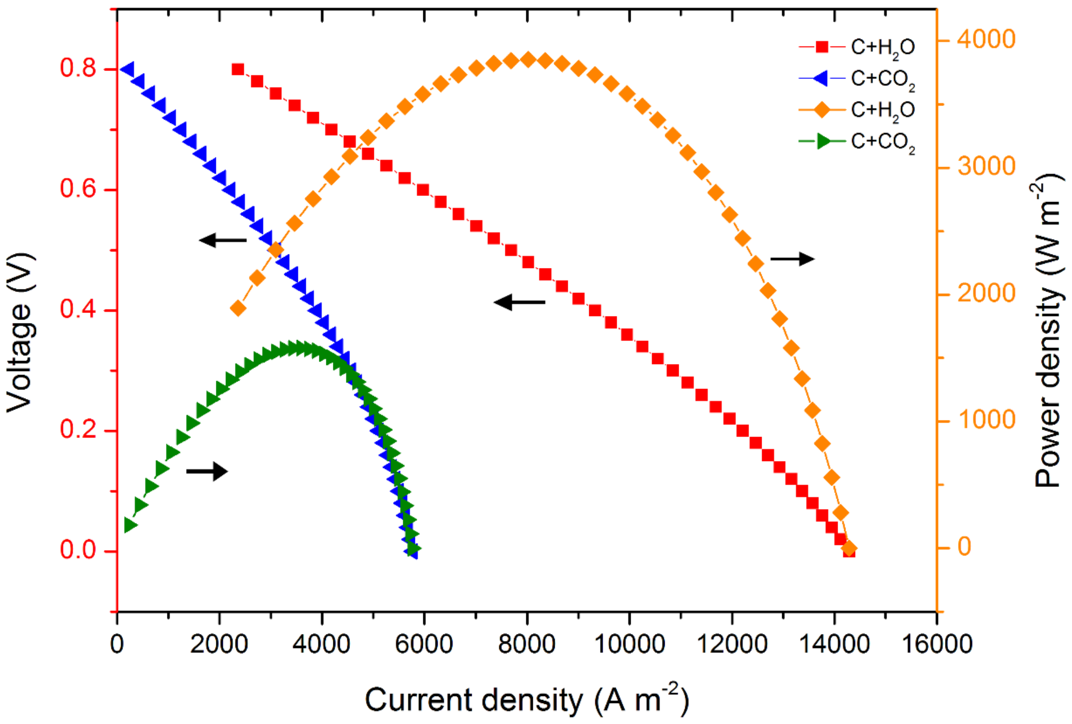

Figure 4.3 The voltage-current density-power density relationships of DC-SOFCs with CO_2 and H_2O as agents

Table 4.3 Operation parameters for operating potential effect study in DC-SOFCs

Parameter	**Value**	**Unit**
Operating potential	0 – 0.8	V
Anode inlet gas flow rate	30	SCCM
Cathode inlet gas flow rate	10	SCCM
Anode gas composition for H_2O assisted DC-SOFC	H_2O 100%	
Cathode gas composition	Air	
Temperature	1123	K

It is found that the performance of DC-SOFCs with H_2O as agent is much higher than that with CO_2 as agent, which is consistent with the previous study[130]. For DC-SOFCs with H_2O as agent, the peak power density reaches 3852 W m^{-2} at 0.48V, which is more than two times of that with CO_2 as agent (1579 W m^{-2} at 0.44V).

This significantly higher performance of H_2O-assisted DC-SOFC is mainly caused by 2 factors. Firstly, faster carbon gasification kinetics by H_2O agent offers a higher mole fraction of fuel (both CO and H_2) and thus higher open circuit voltage. Secondly, with H_2 participating in electrochemical reaction together with CO, a much higher electrochemical reaction rate could be obtained in H_2O assisted DC-SOFCs. As can be seen from Fig. 4.4(a, b), the carbon gasification rate in H_2O assisted DC-SOFCs ranges from 6.45 mol m^{-3} s^{-1} to 20.7 mol m^{-3} s^{-1} at 1123 K and 0.5 V operating potential. While the carbon gasification rate in CO_2 assisted DC-SOFCs only ranges from 2.71 mol m^{-3} s^{-1} to 12.4 mol m^{-3} s^{-1}. Consequently, the fuel mole fraction (H_2 + CO) in H_2O assisted DC-SOFCs is much higher than that (CO) in CO_2 assisted DC-SOFCs at the same applied voltage as shown in Fig. 4.4(c, d) and thus the higher performance could be obtained.

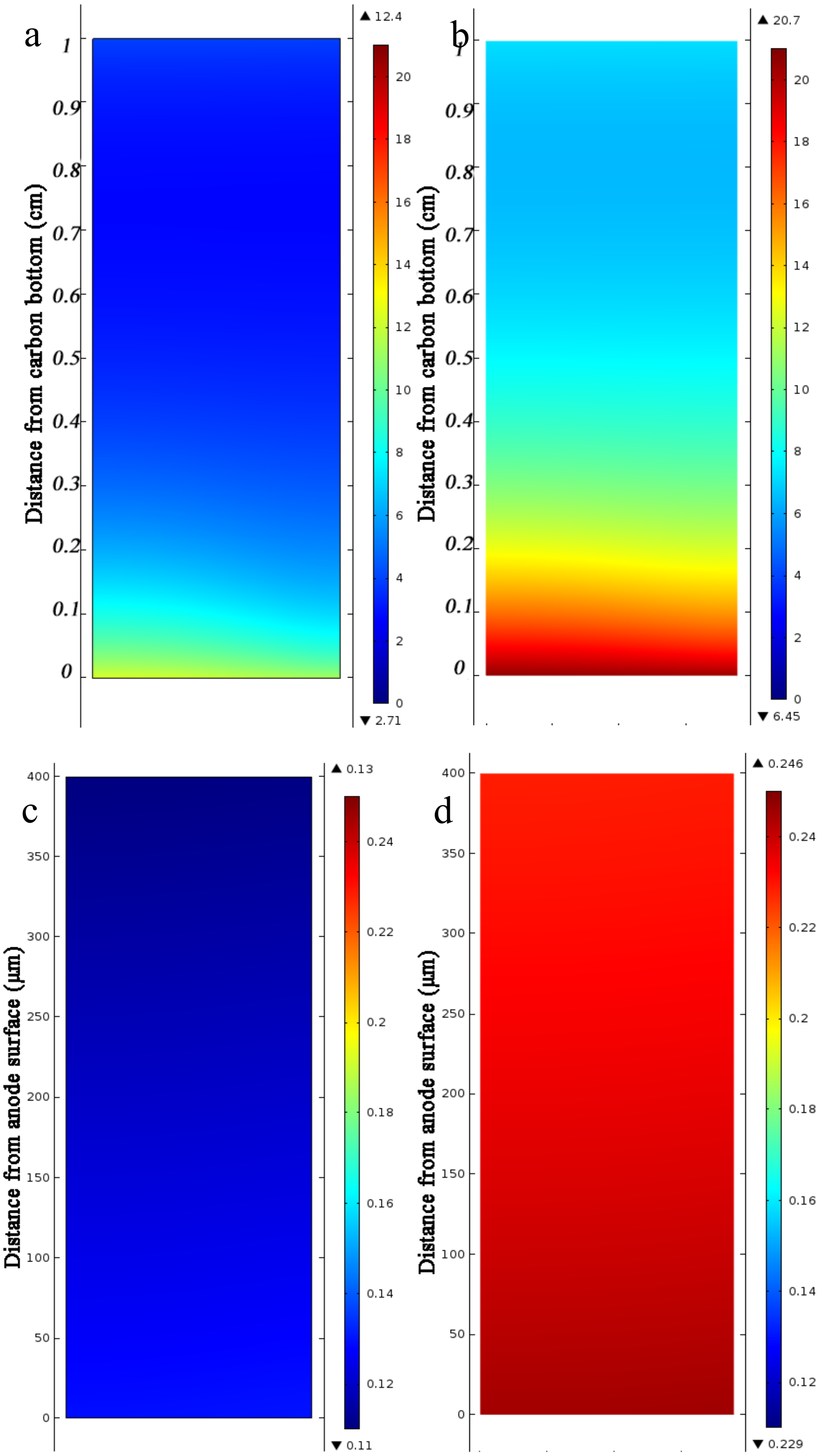

Figure 4.4 The carbon gasification rate with CO_2 (a) and H_2O (b) as agents in carbon layer and mole fraction of fuel with CO_2 (c) and H_2O (d) in anode of DC-SOFCs at 0.5 V and 1123 K

4.3.3 Effect of anode inlet H_2O mole fraction

As H_2O is carried into anode by N_2 in the experiments, the anode inlet H_2O mole fraction only reaches about 33%, which is at a quite low level. Thus, it would be necessary to study the effect of inlet H_2O mole fraction on the performance of DC-SOFC. The related operating conditions are listed in Table 4.4.

Table 4.4 Operation parameters for anode inlet H_2O mole fraction effect study in DC-SOFCs

Parameter	**Value**	**Unit**
Operating potential	0.5	V
Anode inlet gas flow rate	30	SCCM
Cathode inlet gas flow rate	10	SCCM
Anode gas composition for H_2O assisted DC-SOFC	1% - 99%	
Cathode gas composition	Air	
Temperature	1123	K

As can be seen in Fig. 4.5, the current density of DC-SOFC increases significantly with the increase of inlet H_2O mole fraction. The DC-SOFC only has a current density of 2000 A m^{-2} at 1% inlet H_2O mole fraction, while 7000 A m^{-2} is reached with 35% inlet H_2O mole fraction. With the further increase of inlet H_2O mole fraction, only a small increase of current density is achieved due to the limited steam carbon gasification reaction rate. This tendency is also indicated by the change of H_2/H_2O mole fraction ratio in anode. As shown in Fig. 4.6, the molar ratio of H_2/H_2O is quite small (<0.06) at 1% inlet H_2O mole fraction, and it increases 2 more times (~0.2) at 35% inlet H_2O mole fraction, which is almost at the same level with 99% inlet H_2O mole fraction.

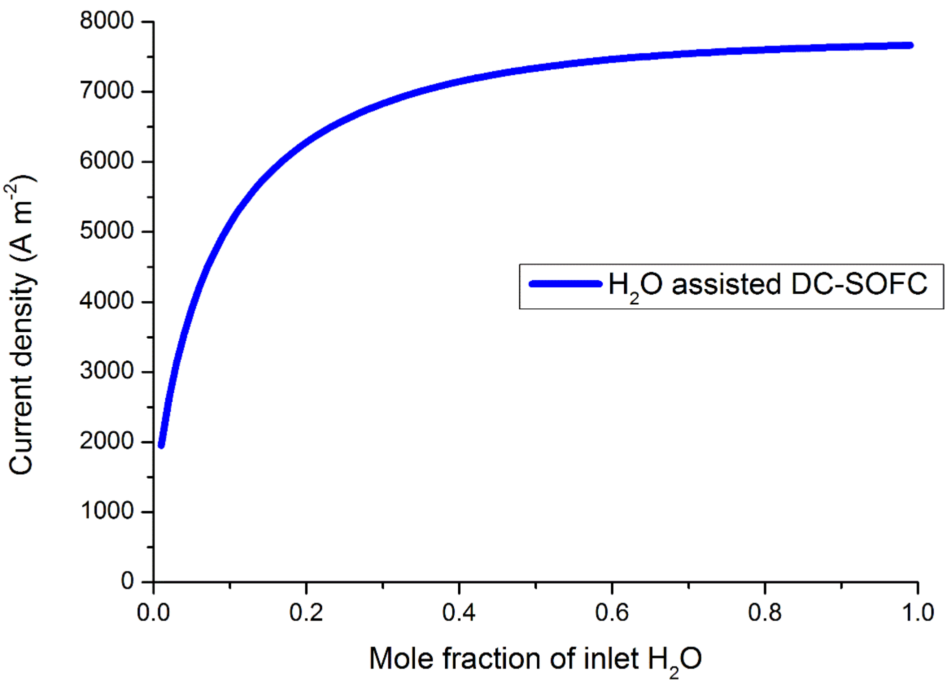

Figure 4.5 Effect of inlet H_2O mole fraction change on the performance of DC-SOFC at 0.5V operating potential

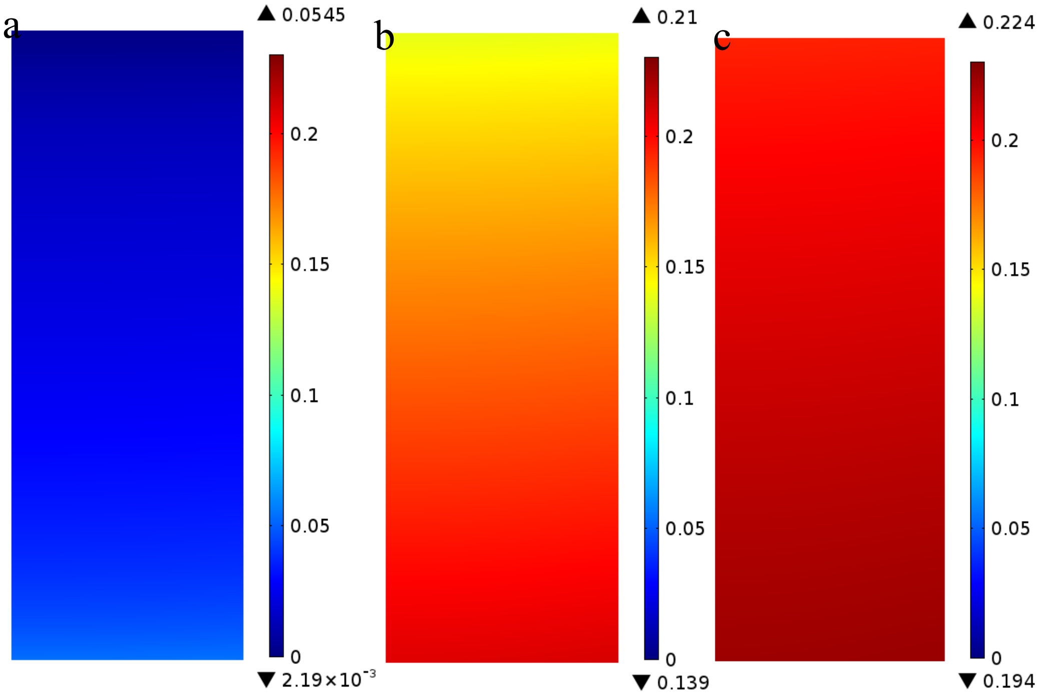

Figure 4.6 Molar ratios of H_2/H_2O in the anode of DC-SOFCs with 1%(a), 35%(b) and 99%(c) mole fraction of H_2O in anode inlet gas

4.3.4 Effect of anode inlet gas flow rate

For H_2-fueled SOFCs, a higher anode inlet gas flow rate ensures a higher anode fuel concentration and higher current density at certain operating potential. For internal reforming SOFC, it is more complicated as the fuel (H_2 and CO) for electrochemical reaction is different from the hydrocarbon fuel. On the one hand, more hydrocarbon fuel may favor the internal reforming reaction, producing more H_2 and CO. On the other hand, high flowrate of the hydrocarbon fuel may also dilute the concentration of H_2 and CO fuel for electrochemical reaction if the reforming reaction is not high enough. The related operating conditions for this section are listed in Table 4.5.

Table 4.5 Operation parameters for anode inlet gas flow rate effect study in DC-SOFCs

Parameter	**Value**	**Unit**
Operating potential	0.5	V
Anode inlet gas flow rate	1 -30	SCCM
Cathode inlet gas flow rate	10	SCCM
Anode gas composition for H_2O assisted DC-SOFC	100%	
Cathode gas composition	Air	
Temperature	1123	K

For DC-SOFCs with CO_2 as agent, the increase of anode inlet gas flow has a negative effect on its performance at an operating temperature of 1123K. As can be seen in Fig. 4.7, with the anode inlet gas flow rate increasing from 1 SCCM to 30 SCCM, the current density of CO_2 assisted DC-SOFC decreases from 3500 A m^{-2} to 3100 A m^{-2}. This is mainly caused by relative slow Boudouard reaction rate, which has become the rate-determining step in DC-SOFCs. As a result, CO_2 produced by electrochemical reaction is already enough for carbon gasification at 1123K and the inlet CO_2 will only dilute the fuel in DC-SOFCs.

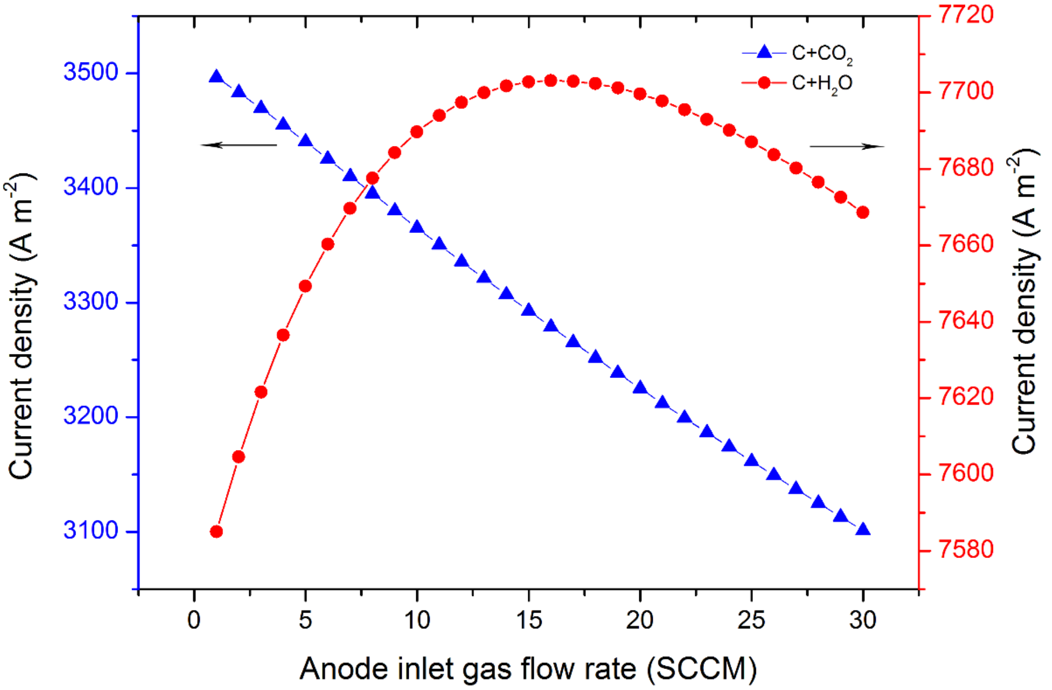

Figure 4.7 The effect of anode inlet gas flow rate on current density of DC-SOFCs with CO_2 and H_2O as agents at 0.5 V and 1123 K

In H_2O assisted DC-SOFCs, the carbon gasification rate is faster and benefits more from the increase of anode inlet gas flow rate in the beginning. Until when the steam carbon gasification rate cannot catch up with the further increase of inlet gas flow rate, fuels in anode are also diluted by inlet H_2O, which results in the decrease of the current density of DC-SOFC.

4.3.5 Effect of operating temperature

The related operating conditions for this section are listed in Table 4.6. As can be seen from Fig. 4.8, the current density of both H_2O-assisted DC-SOFC and CO_2 assisted DC-SOFC is increased at a higher temperature. For CO_2-assisted DC-SOFCs, with temperature increasing from 923 K to 1123 K, the current density is increased from 37 A m^{-2} to 3293 A m^{-2} when the temperature is increased from 923K to 1123K. This huge increase indicates that a relative higher temperature is very necessary for CO_2 assisted DC-SOFCs as Boudouard reaction rate is quite slow at a relatively lower temperature. For H_2O-assisted DC-SOFCs, the current density is 372 A m^{-2} at 923 K, which is almost 10 times of the current density of CO_2-assisted DC-SOFCs. When the operating temperature reaches 1048 K, the current density of H_2O-assisted DC-SOFC reaches

3439 A m^{-2}, exceeding the current density of CO_2 assisted DC-SOFCs at 1123K. Finally, H_2O assisted DC-SOFCs achieves 7690 A m^{-2} at 1123 K, which is still more than 2 times higher than that of CO_2 assisted DC-SOFCs. Both H_2O and CO_2 assisted DC-SOFCs benefits from the increase of operating temperature. Apart from general improvement of electrochemical reaction kinetics as for most SOFCs, faster chemical reaction kinetics as a higher temperature also brings great benefits for DC-SOFCs.

Table 4.6 Operation parameters for temperature effect study in DC-SOFCs

Parameter	**Value**	**Unit**
Operating potential	0.5	V
Anode inlet gas flow rate	10	SCCM
Cathode inlet gas flow rate	10	SCCM
Anode gas composition for H_2O assisted DC-SOFC	100%	
Cathode gas composition	Air	
Temperature	923 - 1123	K

It should also be noticed that H_2O assisted DC-SOFCs still has an acceptable output power density at relatively lower temperature. Thus, using H_2O as agent is very promising for DC-SOFCs at a wider range of temperature.

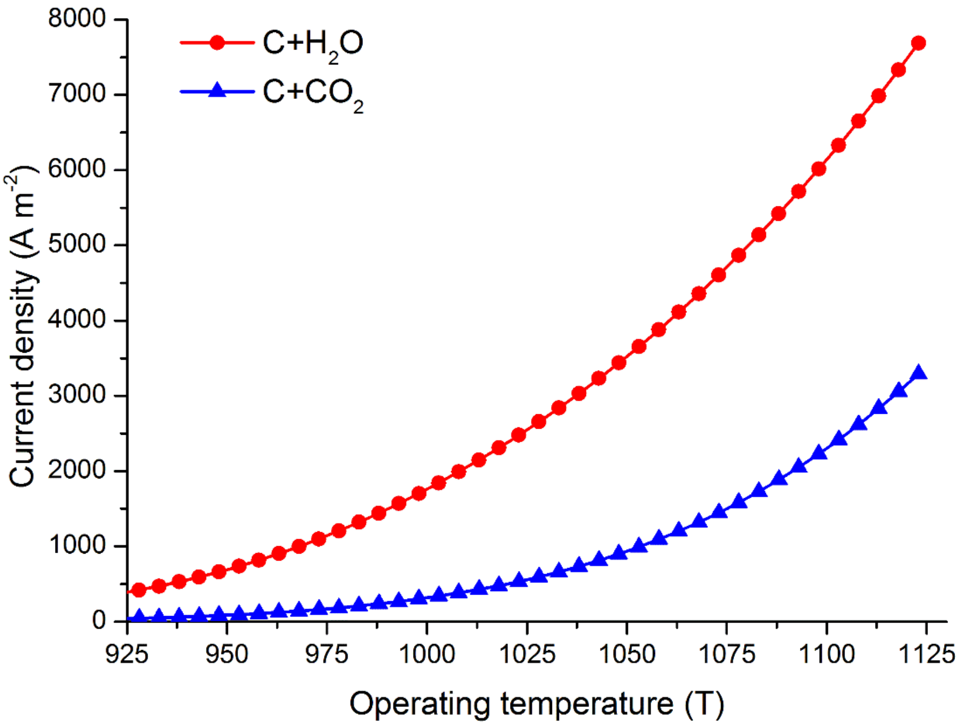

Figure 4.8 The effect of operating temperature on current density of DC-SOFCs with H_2O and CO_2 as agents at 0.5 V operating potential

4.4 Conclusion

A multi-physics model is developed to study the performance of DC-SOFCs with H_2O and CO_2 as agents. Parametric analyses are carried out to investigate the effects of operating potential, anode inlet gas mole fraction/flowrate and operating temperature on the performance of DC-SOFCs. The performance of DC-SOFCs with two different agents are also compared to see the improvement by adding H_2O for carbon gasification in DC-SOFCs.

Benefiting from faster carbon gasification, H_2O-assisted DC-SOFCs has a much higher fuel concentration in anode than CO_2-assisted DC-SOFCs. Coupled with faster electrochemical reaction kinetics by H_2 fuel, using H_2O as agent significantly improves the performance of DC-SOFCs compared with CO_2 agent. As can be seen from the Power-Voltage curve, H_2O-assisted DC-SOFC achieves a peak power density of 3852 W m^{-2}, which is more than 2 times higher than CO_2assisted DC-SOFCs. Besides, H_2O- assisted DC-SOFC has a much better potential for operating at wider temperature range due to its fast gasification reaction kinetics. It is also found that a high anode inlet gas flow rate is not necessary for DC-SOFCs.

5. CHAPTER 5 EXPERIMENTAL AND MODELING OF HIGH PERFORMANCE DIRECT CARBON SOFC WITH IN-SITU CATALYTIC STEAM-CARBON GASIFICATION REACTION

5.1 Introduction

In-situ catalytic steam-carbon gasification is a very attractive strategy as not only a higher power density can be expected due to faster steam-carbon gasification rate, but also higher fuel concentration at the anode outlet can be obtained for wider applications such as fuel and electricity co-generation. Therefore, there is a need to systematically investigate the improvement brought by in-situ catalytic steam-carbon gasification in DC-SOFCs.

5.2. Model development

5.2.1 Model assumption and calculation domain

The chemical/electrochemical reaction, ion/electron conduction and mass/momentum transportation are fully coupled in the 2D mathematical DC-SOFC models. The schematics of DC-SOFC using H_2O as agent is shown in Fig. 5.1. Solid carbon is placed in the anode chamber (near the porous anode) and H_2O is supplied from the anode inlet for steam-carbon gasification. The button cell has a surface area of 0.45 cm^2 with the thickness of its anode, electrolyte and cathode being 400μm, 8μm and 24μm, respectively.

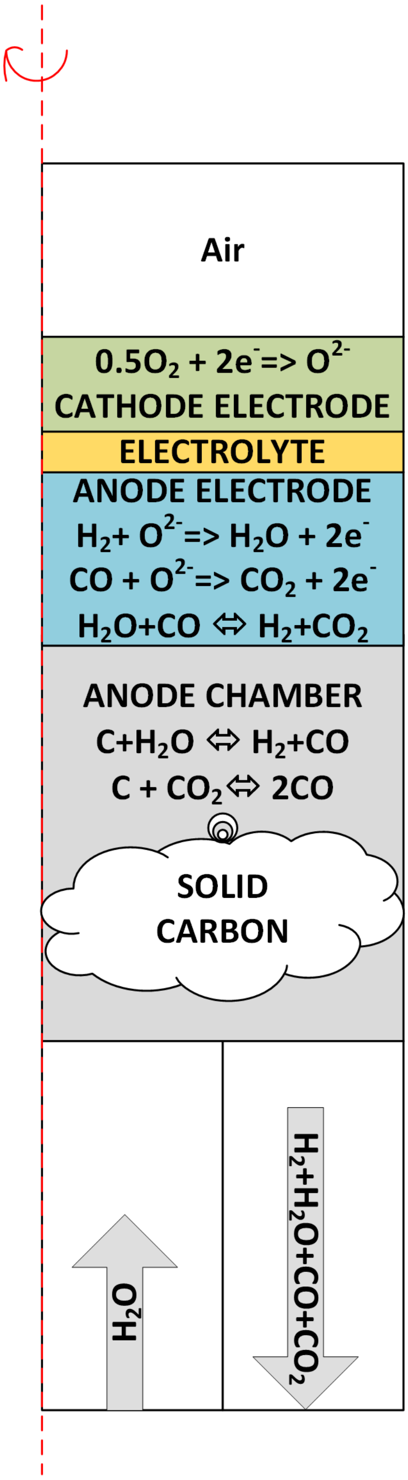

Figure 5.1 Schematic of DC-SOFC using H_2O as gasification agent.

Model assumptions are as follows:

(1) Both H_2 and CO participate in the electrochemical reactions and the TPB sites they shared is proportional to their local concentration percentage.

(2) TPB sites are distributed uniformly in the whole porous electrode. Both ionic- and electronic- conducting phases in the porous electrodes are homogeneous and continuous.

(3) Gases in the model (CO, H_2O, H_2, O_2, N_2) are ideal gases.

(4) Temperature distribution in the cell is uniform due to its small size.

(5) The volume of carbon fuel in the anode chamber does not change with time.

5.2.2 Governing equations

Compared with last chapter, the steam-carbon gasification reaction rate is largely boosted due to the catalysts added in anode chamber. The catalytical steam-carbon gasification reaction rate can be calculated by Eq. (5.2)[141]. Different tuning parameters (listed in Table 5.2) are used when catalyst is adopted for the reaction.

$$C + H_2O \leftrightarrow CO + H_2 \tag{5.1}$$

$$R_{C\_H2O} = \frac{K_1 p_{H_2O}}{1+K_2 p_{H_2}+K_3 p_{H_2O}} \tag{5.2}$$

As CO_2 is formed in the electrochemical oxidation of CO, the Boudouard reaction (Eq. (5.3)) is also considered. Its reaction rate can be calculated by Eq. (5.4).

$$C + CO_2 \leftrightarrow 2CO \tag{5.3}$$

$$R_{C\_CO2} = \frac{K_4 p_{CO_2}}{1+K_5 p_{CO}+K_6 p_{CO_2}} \tag{5.4}$$

Due to the co-existence of H_2O and CO, WGSR catalyzed by nickel in porous electrode is also considered as shown in Eq. (5.5). Its reaction rate can be calculated by Eqs. (5.6-5.9) [36].

$$CO + H_2O \leftrightarrow CO_2 + H_2 \tag{5.5}$$

$$R_{WGSR} = k_{sf}(p_{H_2O}p_{CO} - \frac{p_{H_2}p_{CO_2}}{K_{ps}}) \tag{5.6}$$

$$k_{sf} = 0.0171\exp(\frac{-103191}{RT})\ (\mathrm{mol\ m^{-3}\ Pa^{-2}\ s^{-1}}) \tag{5.7}$$

$$K_{ps} = \exp(-0.2935Z^3 + 0.6351Z^2 + 4.1788Z + 0.3169) \tag{5.8}$$

$$Z = \frac{1000}{T} - 1 \tag{5.9}$$

5.2.2.4 Model solution

Electric potentials are specified at the two electrodes while two ends of the cell are electrically insulated. Inflow gas mole fraction and flow rate (SCCM) are given at the inlets. The outflow condition is specified at the outlets of the gas channels. Zero flux is specified at the end of the electrodes and pressure condition is specified at the outlets of the two gas channels.

The model is solved at given operating conditions such as electric potentials, temperature, inlet gas flow rate and mole fraction. The output of the model includes distributions of the electrochemical reaction rates, chemical reaction rates and mole fraction of gas species in the cell. The commercial software COMSOL MULTIPHYSICS® is employed for the numerical simulation.

5.2.3 Boundary conditions

The electric potentials are specified at the outer boundaries of cathode and anode as working potential and zero potential, respectively. The insulation condition is applied to the bottom and top of the cell.

Inflow gas mole fraction is specified at the inlet of the cathode. The convective flux boundary condition is specified at the outlets of the cathode and anode. Zero flux is assumed at the end of anode chamber, electrolyte/electrode interface and the ends of electrodes.

Standard gas flow rate (SCCM) is specified at the cathode while pressure condition is specified at the outlet. No-slip condition is applied to the end of anode chamber, electrolyte/electrode interface and the ends of electrodes.

5.2.4 Model parameters

The cell uses Ni-YSZ composites as anode, bilayer YSZ/SDC as electrolyte and LSCF cathode. Material properties, chemical/electrochemical reaction and other tuning parameters are adopted and listed in Table 5.1 and Table 5.2, respectively.

Table 5.1 Material properties [137, 139, 143-145]

Parameters	**Value or expression**	**Unit**
Ionic conductivity		

YSZ	$3.34 \times 10^{4} e^{\frac{-10300}{T}}$	Sm^{-1}
SDC	$\frac{100}{T} \times 10^{5.48077-\frac{3792.53}{T}}$	Sm^{-1}
LSCF	$\frac{100}{T} \times 10^{2.51289-\frac{3036.75}{T}}$	Sm^{-1}
Electronic conductivity		
LSCF	$\frac{100}{T} \times 10^{4.32576+\frac{1204.26}{T}}$	Sm^{-1}
Ni	$3.27 \times 10^{6} - 1065.3T$	Sm^{-1}
Porosity		
Cathode	0.2	
Anode	0.6	
Anode volume fraction		
YSZ	0.4	
Ni	0.6	
S_{TPB}		
Cathode layer	2.14×10^{5}	m^{2}m^{-3}
Anode layer	2.14×10^{5}	m^{2}m^{-3}
Electrode tortuosity	3	
Solid carbon	Activated carbon (Aladdin, Shanghai, China; A. R.)	

Table 5.2 Reaction parameters [146]

Parameter	**Value**	**Unit**
Chemical reaction without catalyst		
K_1	1.03×10^{-3}	s mol kg^{-1} m^{-2}
K_2	9.88×10^{-4}	Pa^{-1}

K_3	8.13×10^{-5}	Pa^{-1}
K_4	3.11×10^{-5}	$s\ mol\ kg^{-1}\ m^{-2}$
K_5	1.25×10^{-3}	Pa^{-1}
K_6	3.82×10^{-5}	Pa^{-1}
Chemical reaction with catalyst		
K_1	3.87×10^{-2}	$s\ mol\ kg^{-1}\ m^{-2}$
K_2	9.88×10^{-4}	Pa^{-1}
K_3	8.13×10^{-5}	Pa^{-1}
K_4	1.17×10^{-3}	$s\ mol\ kg^{-1}\ m^{-2}$
K_5	1.25×10^{-3}	Pa^{-1}
K_6	3.82×10^{-5}	Pa^{-1}
Electrochemical reaction		
γ_{H_2}	3.68×10^{9}	$A\ m^{-2}$
E_{act,H_2}	1.2×10^{5}	$J\ mol^{-1}$
γ_{O_2}	3.48×10^{9}	$A\ m^{-2}$
E_{act,O_2}	1.2×10^{5}	$J\ mol^{-1}$
γ_{CO}	1.67×10^{9}	$A\ m^{-2}$
$E_{act,CO}$	1.2×10^{5}	$J\ mol^{-1}$
α_{H_2}	0.5	
α_{CO}	0.5	
α_{O_2}	0.85	

5.2.5 Model solution

The model is solved at given operating conditions such as electric potentials, temperature, inlet gas flow rate and mole fraction. The output of the model includes distributions of the electrochemical reaction rates, chemical reaction rates and mole fraction of gas species in the cell. The commercial software COMSOL MULTIPHYSICS® is employed for the numerical simulation.

5.3 Results and discussion

5.3.1 Experiments for model validation

The fuel cell adopted in this study for model validation employed Ni-YSZ as anode supporting the bilayer YSZ/SDC electrolyte and LSCF cathode. Na_2CO_3 was adopted as the catalyst to enhance the steam-carbon gasification reaction. For a typical synthesis, 0.015 mole catalyst was dissolved into 30 ml de-ionized water. Then 1 mole carbon was added to the solution under vigorous stirring for 12 hours. The colloid was dried at 110 ºC for 4 hours and then calcined at 500 ºC in nitrogen for 2 hours.

For the fuel cell test, the bottom cell was sealed onto a quartz tube by silver paste. The anode and cathode surfaces were printed with silver layers for current collection. 0.2 g solid carbon was fixed by asbestos in the anode chamber. A quartz tube was positioned beneath the carbon layer for introducing steam. The inlet gas flow rate of anode was set as 90 SCCM (standard conditions). 30 SCCM H_2O was carried into anode by 60SCCM N_2 in the test. The operating temperature was kept constant at 850 ° C during the test. Current-voltage values were collected based on the four-terminal configuration..

The modeling results of current-voltage characteristics for DC-SOFCs using H_2O as agent are compared with experimental data as shown in Fig. 5.2. The quite small difference between the modeling results and experimental data validates the present model. The same structure and tuning parameters are used in the subsequent parametric simulations.

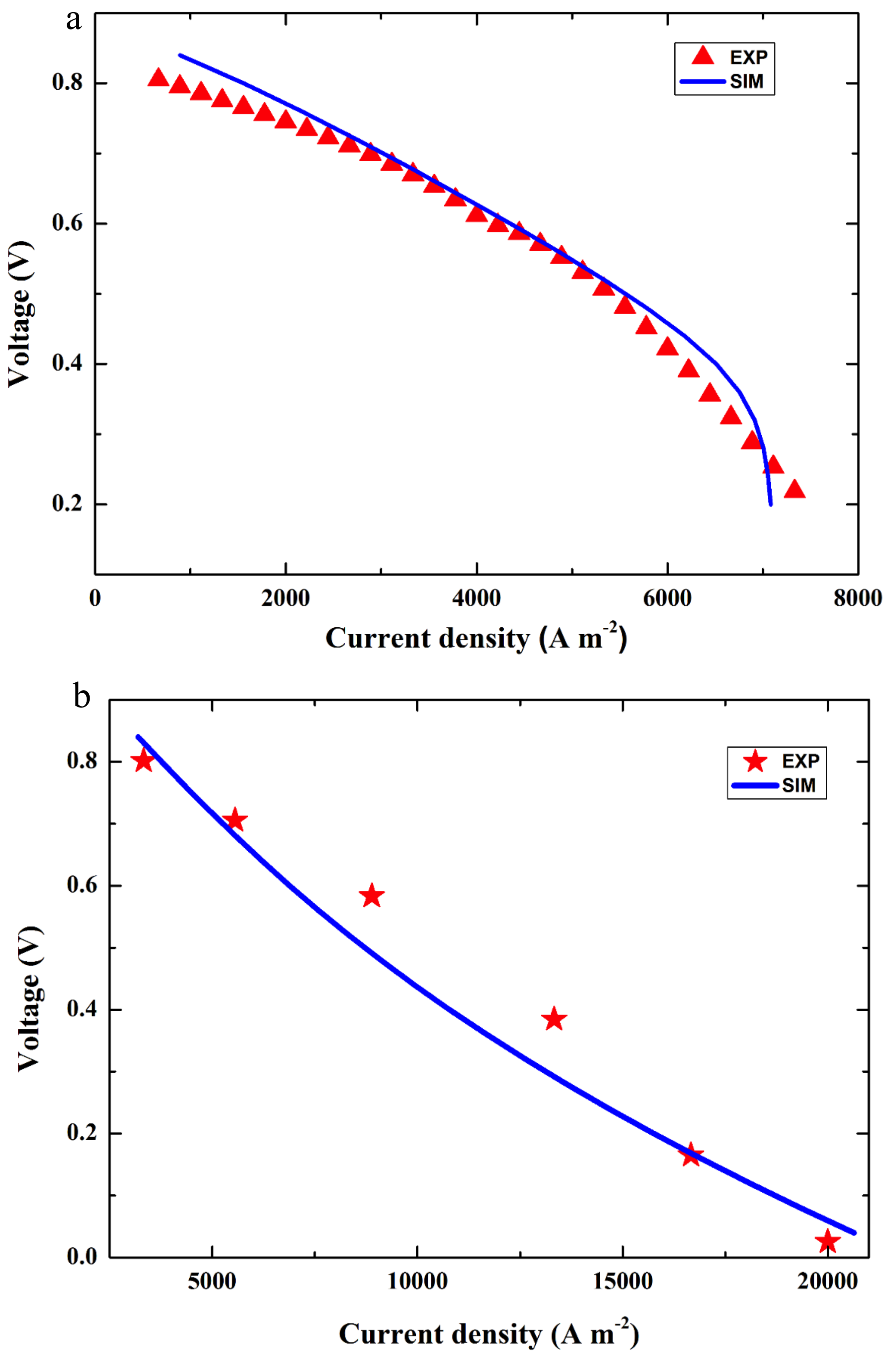

Figure 5.2 Model validation for DC-SOFCs using H_2O as agents without (a) and with (b) catalyst.

5.3.2 Effect of applied voltage

The voltage-current density-power density curves of DC-SOFCs using H_2O as agent are shown in Fig. 5.3. The detailed operating conditions are listed in Table 5.3.

Table 5.3 Operation parameters for operating potential effect study in DC-SOFCs

Parameter	**Value**	**Unit**
Operating potential	0 – 1	V
Anode inlet gas flow rate	90	SCCM
Cathode inlet gas flow rate	10	SCCM
Anode gas composition	H_2O	
Cathode gas composition	Air	
Temperature	1123	K

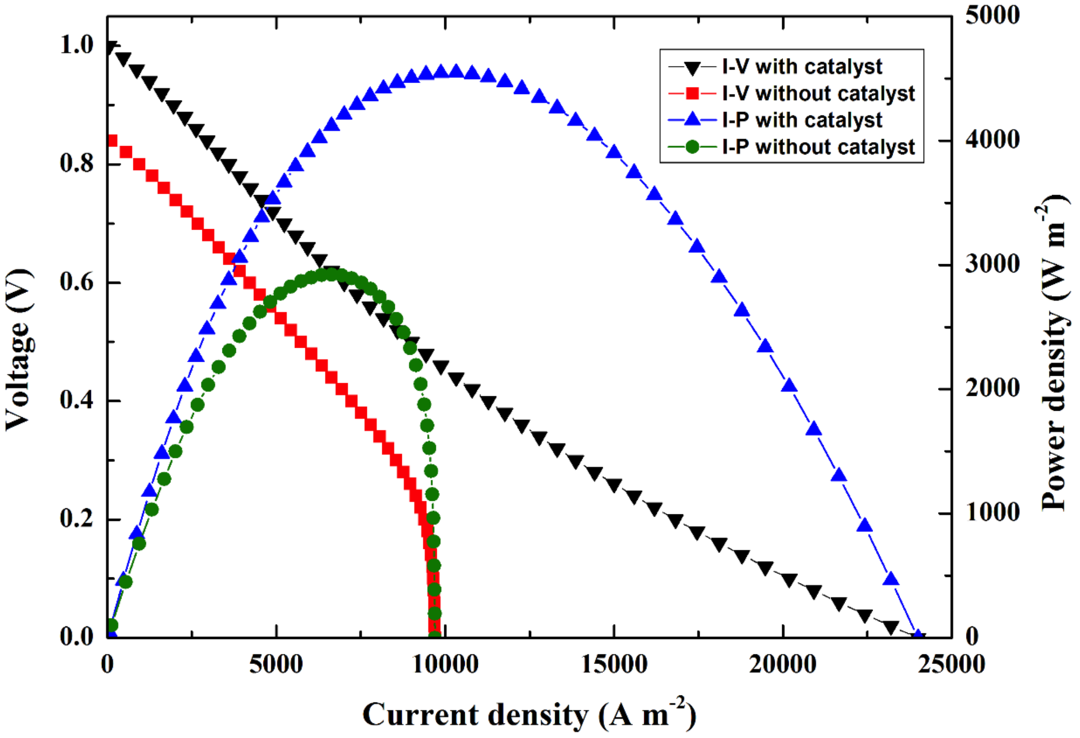

Figure 5.3 The voltage-current density-power density relationships of DC-SOFCs using H_2O as agents with and without catalyst.

As can be seen in Fig. 5.3, the cell with in-situ catalytic steam-carbon gasification has a much better performance compared with the cell without catalyst. By adding catalyst, the peak power density of the cell increases from about 3000 W m^{-2} to 4600 W m^{-2}, with the maximum current density increasing from about 10000 A m^{-2} to 23000 A m^{-2}. This significant performance improvement is mainly caused by the faster steam-carbon gasification kinetics. As can be seen in Fig. 5.4(a) and Fig. 5.4(b), the peak steam-carbon gasification reaction rate increases from 11.1 mol m^{-3} s^{-1} to 292 mol m^{-3} s^{-1} with most parts in catalytic carbon layer being larger than 50 mol m^{-3} s^{-1}. Consequently, the mole fraction of the fuel (both H_2 and CO) in anode is significantly improved from about 0.1 to about 0.4 as shown in Fig. 5.4(c) and Fig. 5.4(d). The high fuel concentration indicates the potential for syngas and electricity co-generation in DC-SOFC with in-situ catalytic gasification.

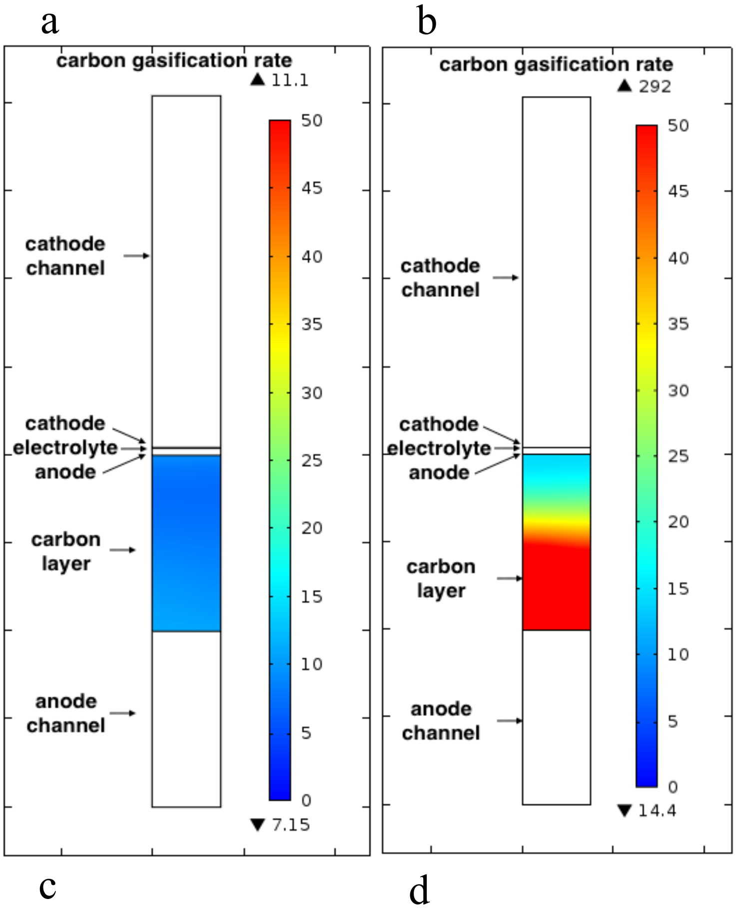

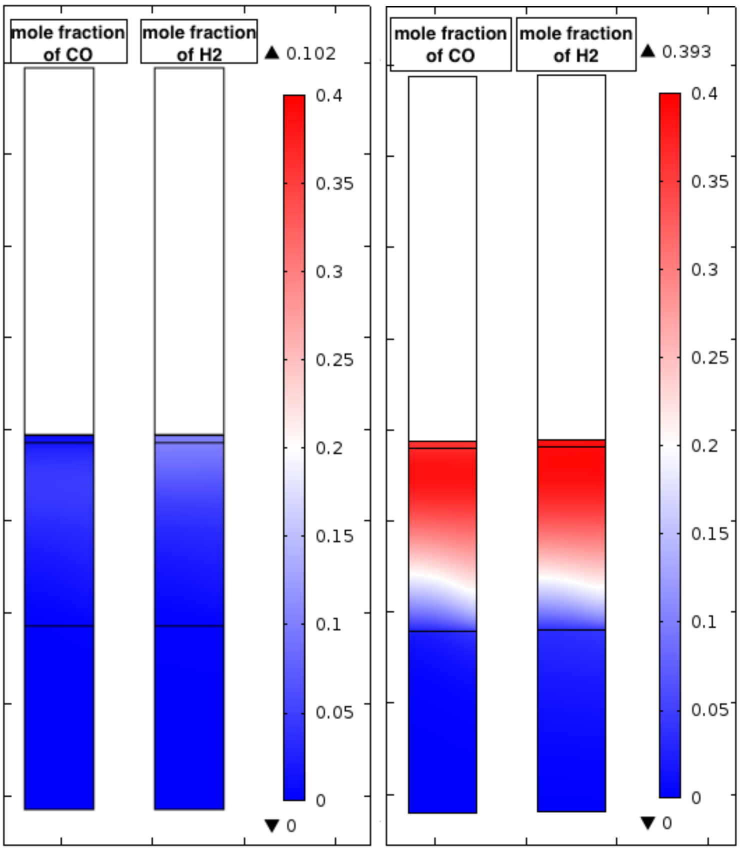

Figure 5.4 The carbon gasification rate (mol m^{-3} s^{-1}) without (a) with (b) catalyst in carbon layer and mole fraction of fuel without (c) and with (d) catalyst in anode of DC-SOFCs at 0.8 V and 1123 K

It should also be noted that the fuel concentration distribution in anode is significantly affected by both steam-carbon gasification reaction and applied voltage. As can be found in Fig. 5.5(a), the H_2 mole fraction obtains a sharp increase to 0.4 in carbon layer at 0.9 V applied voltage, while it decreases quickly to 0.2 in the area close to anode at 0.1 V applied voltage. The relationship between electrochemical performance and syngas molar fraction on anode surface is further shown in Fig. 5.5(b). The syngas molar fraction exceeds over 80% at small operating current density, while declines to less than 50% at 23000 A m^{-2}. Thus, a high operating potential is more favored to maintain a high fuel concentration in the anode outlet gas.

a

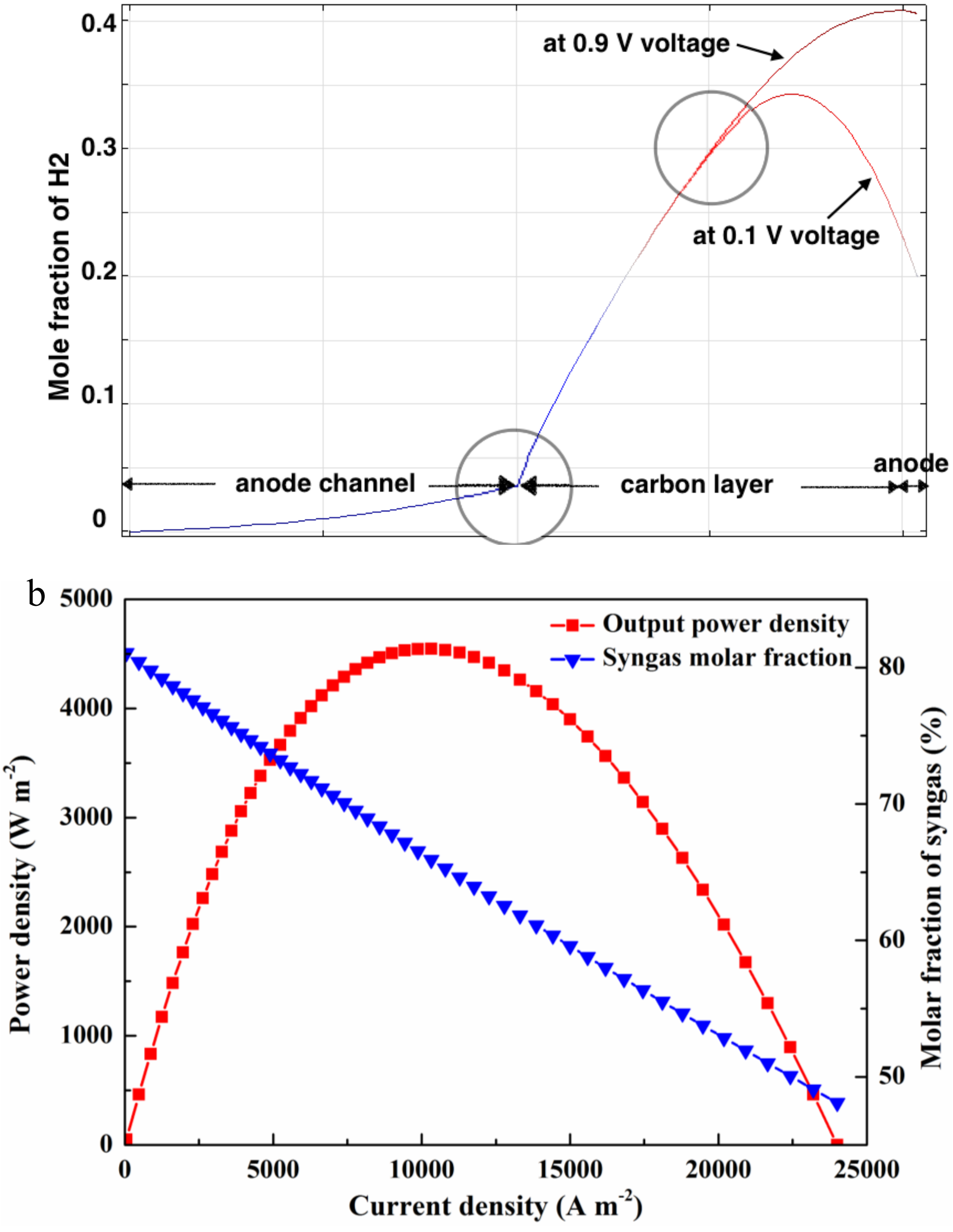

Figure 5.5 (a)Distribution change of H_2 mole fraction in anode with catalytic gasification at 0.9 V and 0.1 V operating potentials and 1123K; (b) I-P characteristics and syngas molar fraction change at different operating current densities.

5.3.3 Effect of anode inlet gas flow rate

In DC-SOFCs using H_2O as agent, steam is introduced to the anode inlet as it participates in the carbon gasification reaction, however, the inlet steam can dilute fuel concentration on the other hand. Thus, it should be careful to choose a suitable steam flow rate in operation. For the study of anode inlet gas flow rate effect, the operating parameters are listed in Table 5.4.

Table 5.4 Operation parameters for anode inlet gas flow rate effect study in DC-SOFCs

Parameter	**Value**	**Unit**
Operating potential	0.5	V
Anode inlet gas flow rate	1 -200	SCCM
Cathode inlet gas flow rate	10	SCCM
Anode gas composition	H_2O	
Cathode gas composition	Air	
Temperature	1123	K

As can be seen in Fig. 5.6, the performance of the fuel cell increases first at small anode gas flow rate, while decreases quickly at large flow rate. A small steam flow rate is more suitable for the fuel cell as it reaches the peak current density at 10 SCCM in this case. However, no significant decrease of current density is observed in a wide flow rate range when catalyst is added in the fuel cell. Besides, a large steam flow rate is more favored under the fast in-situ catalytic gasification reaction with its peak current density being obtained at 40 SCCM flow rate.

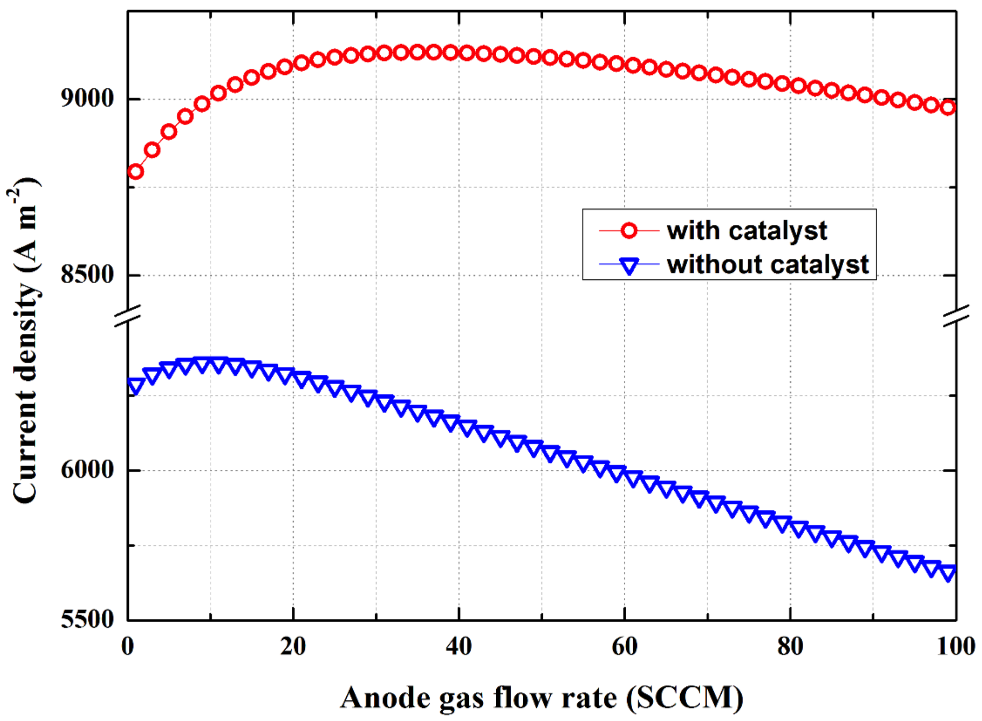

Figure 5.6 The effect of anode inlet gas flow rate on current density of DC-SOFCs with H_2O as agents at 0.5 V and 1123 K

In addition, the mole fraction of H_2 and CO in anode is also significantly affected by inlet steam flow rate as can be seen in Fig. 5.7(a). Apart from different electrochemical reaction kinetics, the reaction rate of WGSR is another key factor to the mole fraction change of H_2 and CO (as shown in Fig. 5.7(b)) since steam-carbon gasification produces equal amount of H_2 and CO. At small gas flow rates, more H_2 than CO is consumed by electrochemical reaction due to the faster reaction kinetics of H_2, in the meanwhile, the lack of steam favors WGSR to convert H_2 and CO_2 into H_2O and CO in anode (shown as negative value of WGSR in Fig. 5.7(b)). As a result, more CO than H_2 is left in anode. With an increase of steam flow rate, the WGSR rate turns to positive and keeps growing, while the Boudouard reaction rate remains at a small value. Consequently, the mole fraction of CO keeps decreasing, while the mole fraction of H_2 keeps rising to exceed CO and remains at a relative high level. This phenomenon indicates that the outlet gas composition from anode can be adjusted by controlling the inlet gas flow rate.

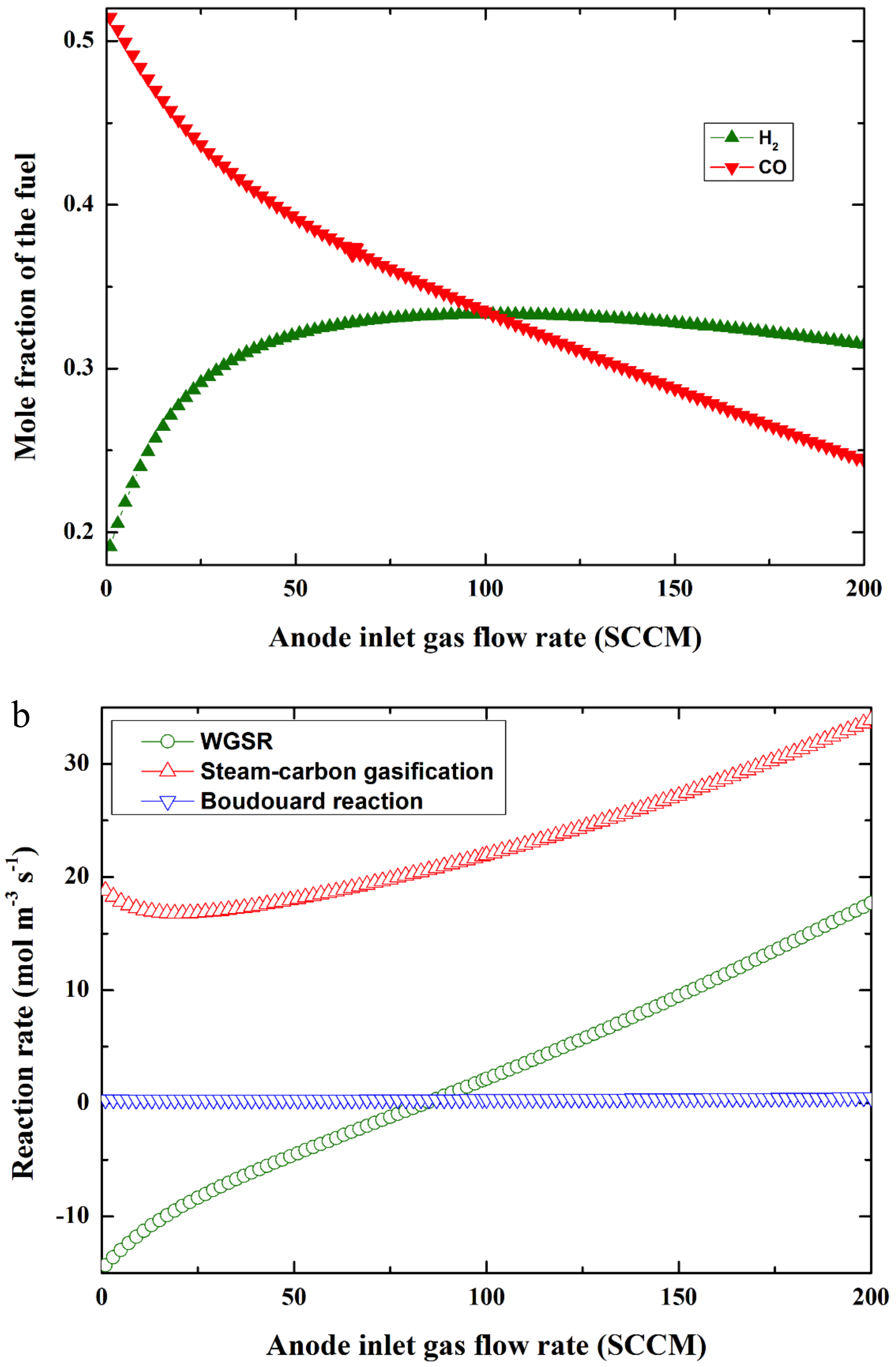

Figure 5.7 The effect of anode inlet gas flow rate on fuel mole fraction (a) and chemical reaction rates (b) in anode surface of DC-SOFCs at 0.5 V and 1123 K

5.3.5 Effect of operating temperature

The operating temperature affects not only the electrochemical kinetics but also the chemical reaction rate, thus, both the output power and the fuel percentage (H_2 & CO) in outlet gas will be significantly changed at different operating temperature. For the study of temperature effect, the operating parameters are listed in Table 5.5.

Table 5.5 Operation parameters for temperature effect study in DC-SOFCs

Parameter	**Value**	**Unit**
Operating potential	0.5	V
Anode inlet gas flow rate	90	SCCM
Cathode inlet gas flow rate	10	SCCM
Anode gas composition	H_2O	
Cathode gas composition	Air	
Temperature	923 - 1173	K

As can be seen in Fig. 5.8(a), the current density of DC-SOFC with H_2O as agent is increased at a higher temperature. The existence of catalyst improves the performance of DC-SOFC especially at a low operating temperature, where a large improvement can be found (4 times improvement at 923 K and 1.4 times improvement at 1173 K). Although the output electricity power improvement by adding catalyst is not that significant at high operating temperature, the fuel percentage in outlet gas is largely improved as shown in Fig. 5.8(b). Benefited from faster chemical reaction kinetics as a higher temperature, the fuel percentage in outlet gas increases from 0.15% at 923 K to 20% at 1173 K without catalyst, while a percentage of 85% of fuel in the outlet gas can be obtained with the help of catalyst at 1173 K. The high fuel concentration indicates an excellent potential for fuel (H_2 & CO) and electricity cogeneration in DC-SOFC with in-situ catalytic steam-carbon gasification.

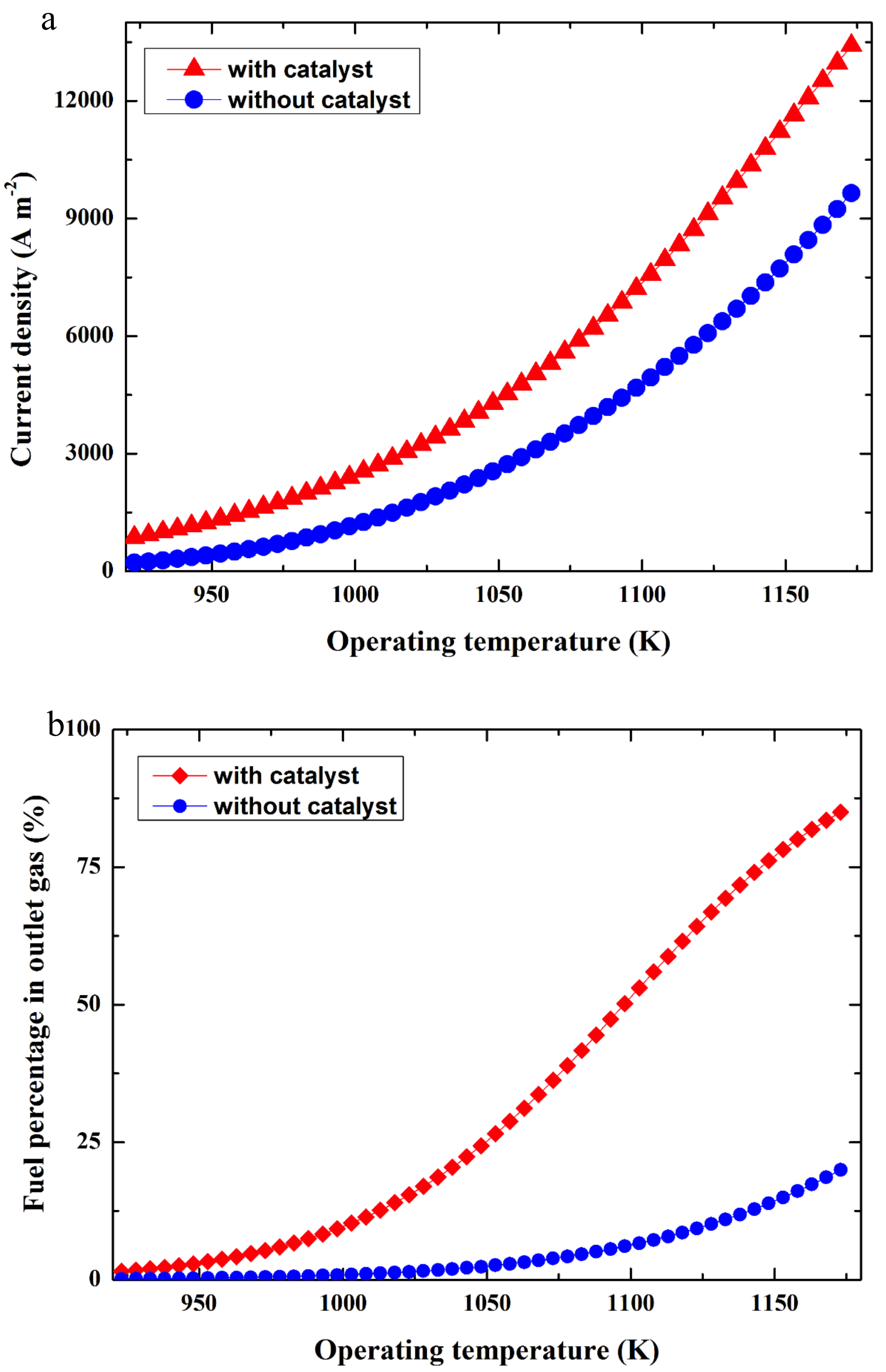

Figure 5.8 The effect of operating temperature on current density (a) and fuel percentage in outlet gas (b) of DC-SOFCs with H_2O as agents at 0.5 V operating potential

5.4 Conclusion

Both experimental testing and mathematical modeling are conducted to study the performance of DC-SOFCs with in-situ catalytic gasification of carbon by H_2O. The model is compared and validated by experimental results. Parametric analyses are carried out to investigate the effects of operating potential, anode inlet gas flowrate and operating temperature on the performance of the cell. The performance of DC-SOFCs with and without catalyst are also compared to evaluate the improvement by adding catalyst for steam-carbon gasification in DC-SOFCs.

In-situ catalytic steam-carbon gasification largely increases the gas fuel production rate for electrochemical reaction, which brings a significant improvement of output power density. A peak power density of about 4600 W m^{-2} is obtained with the help of catalyst compared with that of 3000 W m^{-2} without catalyst. The high fuel percentage in anode outlet gas is also obtained due to the faster gasification reaction with catalyst. It is found that the mole fraction of H_2 and CO in the outlet gas is significantly affected by the inlet gas flow rate. The mole fraction of CO is larger than H_2 at small inlet gas flow rate (< 100 SCCM), while H_2 exceeds CO at high inlet gas flow rate (> 100 SCCM). Thus, it could be possible to adjust the fuel component by controlling the inlet gas flow rate. The operating temperature also significantly affect the fuel percentage in outlet gas, where a high fuel percentage (84% at 1173 K) can be obtained, indicating the possibility for fuel and electricity co-generation in DC-SOFC with H_2O as agent by integrating in-situ catalytic steam-carbon gasification.

6. CHAPTER 6 MODELING OF DIRECT CARBON-ASSISTED SOLID OXIDE ELECTROLYSIS CELL FOR SYNGAS PRODUCTION AT TWO DIFFERENT ELECTRODES

6.1 Introduction

Previous chapters have introduced the characteristics of SOCs for electricity power and fuel cogeneration using solid carbon. In this chapter, the electrolysis mode of SOCs are studied. An SOEC model is developed to study its potential for syngas production at two different electrodes. For practical application of SOEC, its electricity consumption needs to be further reduced as the quality of electricity (i.e. exergy) is high. Recent studies have demonstrated that by supplying low cost fuel (such as CH4 and CO) to the anode of SOEC (termed as fuel-assisted SOEC: FA-SOEC) for steam electrolysis could significantly reduce the operating potential of SOEC, thus greatly reduce the electrical power consumption. When fuel is supplied to the FA-SOEC anode to consume the oxygen ions so as to reduce the oxygen partial pressure, the equilibrium potential can be greatly reduced. If the fuel concentration in anode is sufficiently high and the operating current is relatively low, the required potential for electrolysis could become negative. This means that the FA-SOEC can generate electrical power rather than consume it. Therefore, the FA-SOEC can also be considered as an SOFC whose oxygen ions come from H_2O, instead of from O_2 molecules.

6.2 Model development

6.2.1 Model assumptions and calculation domain

Numerical model of tubular CA-SOEC is developed by coupling governing equations of electrochemical reactions, chemical reactions, ion/electronic charge transport, mass transport and momentum transport. Due to the excellent reversible operating characteristic of fuel cell, the electrochemical properties of the cell in the fuel cell mode are adopted for the electrolysis mode.

The schematic of the tubular CA-SOEC unit is shown in Fig. 6.1. One end of the anode chamber is sealed. Activated carbon powder (Aladdin, 8-16 mesh) is supplied to anode chamber and water vaper is supplied to the cathode channel. The carbon powder reacts with O_2 (from the initial rest air) in anode chamber to form CO_2 in the first stage, which further react with carbon through Boudouard reaction to produce CO. The CO gas is then diffused to the TPB sites in the porous anode to reacts with O^{2-} form CO_2. Subsequently, the electrochemically produced CO_2 diffuses back to anode chamber to react with carbon to form CO. This reaction route repeats between anode chamber and anode electrode in the steady operating state, with net CO production and electricity generation as shown in Eqs (1, 3-5).

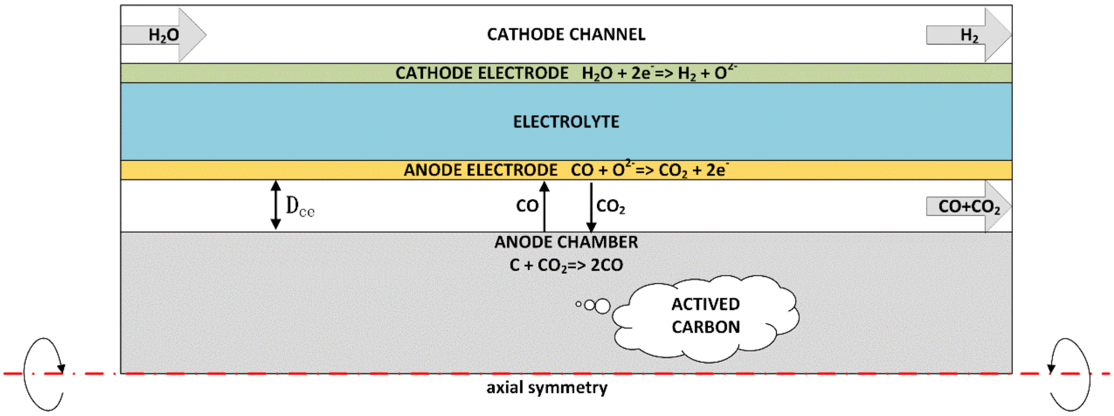

Figure 6.1 Schematic of CA-SOEC

The cell in the present study has a length of 9cm (L_{cell}), an inner diameter of 11.5mm and an outer diameter of 12.0mm. The thickness of anode, electrolyte and cathode are 20μm, 201μm and 20μm, respectively. In addition, the tubular CA-SOEC uses Ag-GDC for both anode and cathode, and YSZ for electrolyte. The materials of both electrodes are porous enough for gas transport and the electrolyte is dense enough to separate gases of anode and cathode. The current is measured at operating voltage ranging from 0.7 V to -0.1 V, where positive voltage means the cell generates electricity and negative means the cell consumes electricity.

The main assumptions are listed as following:

The electrochemical reactions spatially occur along electrode thickness within the porous electrodes. The active sites for electrochemical reactions are assumed to be uniformly distributed in the porous electrodes. The two conducting phases (electronic and ionic) are considered to be homogeneous in the porous electrodes.

The ionic and electronic charge transport processes take place in PEN. The charge transfer reactions are assumed to take place all through the porous electrodes at TPB.

All of the gases (CO, CO_2, H_2 and H_2O) are considered as ideal gases. The flow is considered to be incompressible.

Temperature distribution is uniform in CA-SOEC.

The volume of activated carbon in anode chamber does not change.

6.2.2 Governing equations

The micro-scale tubular CA-SOEC model couples the process of electrochemical reactions in porous electrodes, chemical reactions in chamber, ion/electronic charge transport in electrolyte and electrodes, mass & momentum transport in channels and electrodes.

6.2.2.1 Chemical reaction model

In the anode side, reversed Boudouard reaction is considered as the governing reaction at the solid carbon-gas phase interface, as shown in Eq. (6.1).

$$C + CO_2 \leftrightarrows 2CO \tag{6.1}$$

where the initial CO_2 comes from the reaction between carbon and initial O_2 in anode. When CA-SOEC starts to operate, CO_2 can be electrochemically produced. The reversed Boudouard reaction rate is calculated by Eq. (6.2)[147]:

$$R_{rb} = k_{rb}\exp(-E_{rb}/RT)c_{CO_2} \tag{6.2}$$

6.2.2.2 Electrochemical reaction model

As shown in Fig. 6.1, the CO/CO_2 gas mixture and H_2O/H_2 mixture are at the anode and cathode, respectively. In the porous cathode, H_2O molecule diffuses through the porous electrode to the TPB sites in the whole cathode, where it is reduced to oxygen ions (O^{2-}) and H_2 via reactions (6.3).

$$H_2O + 2e^- \rightarrow H_2 + O^{2-} \tag{6.3}$$

The oxygen ions transport through the dense electrolyte to TPB at anode, where they lose electrons and form CO_2 molecules with CO as described in reaction (6.4).

$$CO + O^{2-} \rightarrow CO_2 + 2e^- \qquad (6.4)$$

The overall electrochemical reaction can be written as:

$$CO + H_2O \rightarrow CO_2 + H_2 \qquad (6.5)$$

In operation, the required potential (V) applied to SOEC can be expressed as:

$$V = E + \eta_{act,an} + \eta_{act,ca} + \eta_{ohmic} \qquad (6.6)$$

where E is the equilibrium potential (Nernst potential) related with thermodynamics; η_{act} is the activation overpotentials reflecting the electrochemical activity of the electrodes; η_{ohmic} is the ohmic overpotential influenced by ionic and electronic conduction. It should be noted that the concentration overpotentials are not included in Eq. (6.6) as the gas partial pressure at the reaction sites (TPB) are used in the calculation of equilibrium potential.

Equilibrium potential (Nernst potential)

In CA-SOEC, the equilibrium potentials for reactions (6.5) can be separated to two parts of partial equilibrium potential in cathode and anode as shown in Eqs. (6.7) - (6.8).

$$E_{H_2-H_2O,ca} = \frac{RT}{2F}\ln(\frac{P^L_{H_2O,ca}}{P^L_{H_2,ca}}) \qquad (6.7)$$

$$E_{CO-CO2,an} = \frac{RT}{2F}\ln(\frac{P^L_{CO_2,an}}{P^L_{CO,an}}) \qquad (6.8)$$

where R is the universal gas constant; T is temperature (K); F is the Faraday constant and P^L_{CO}, $P^L_{CO_2}$, $P^L_{H_2}$ and $P^L_{H_2O}$ are the local partial pressures of CO, CO_2, H_2 and H_2O at the TPB (reaction sites), respectively. The overall Nernst potential in CA-SOEC is the standard overpotential plus the difference of cathode and anode partial equilibrium potential as

$$E = E^0 + E_{H_2-H_2O,ca} - E_{CO-CO2,an} \qquad (6.9)$$

where

$$E^0 = \Delta G/nF \qquad (6.10)$$

for temperature range between 873K and 1273K, E^0 can be expressed as:

$$E^0 = -0.178 + 1.626 \times 10^{-4}\ (V) \qquad (6.11)$$

Activation overpotential

The activation overpotentials are related to the activation energy barriers for electrochemical reactions to proceed. The Butler-Volmer equation is widely used for determining the relationship between the activation overpotential and the current density:

$$i = i_0 \left\{ \exp\left(\frac{\alpha n F \eta_{act}}{RT}\right) - \exp\left(\frac{(1-\alpha) n F \eta_{act}}{RT}\right) \right\} \quad (6.12)$$

where i_0 is the exchange current density, α is the electronic transfer coefficient and n is the number of electrons transferred per electrochemical reaction.

Ohmic overpotential

The ohmic overpotential in a FA-SOEC consists of ionic ohmic overpotential and electronic ohmic overpotential. The ionic and electronic conductivity of electrode and electrolyte materials can be found in Table 6.1. The ohmic overpotential can be calculated by the Ohm's law:

$$i_l = -\sigma_l{}^{eff} \nabla(\emptyset_l) \quad (6.13)$$

$$i_s = -\sigma_{s.eff} \nabla(\emptyset_s) \quad (6.14)$$

Where $\sigma_{l.eff}$ and $\sigma_{s.eff}$ are the effective ionic and electronic conductivity, $\emptyset_l$ and $\emptyset_s$ are the ion conducting and electron conducting electric potentials, respectively. In porous electrodes, they are related with the structure parameters including volume fraction and tortuosity as:

$$\sigma_l{}^{eff} = \sigma_l \cdot \frac{V_l}{\tau_l} \quad (6.15)$$

$$\sigma_s{}^{eff} = \sigma_s \cdot \frac{V_s}{\tau_s} \quad (6.16)$$

where σ_l and σ_s are the intrinsic ionic and electronic conductivity as listed in Table 6.1.

Table 6.1 Model parameters [53]

Parameters	**Value or expression**	**Unit**
Ionic conductivity		
GDC	$\frac{100}{T} \times 10^{\left(6.66071 - \frac{5322.92}{T}\right)}$ [148]	Sm^{-1}

YSZ	$3.34 \times 10^4 e^{\frac{-10300}{T}}$	Sm^{-1}
Electronic conductivity		
Ag	$\frac{1.59e^{8}}{(0.0038T-0.1134\ ))}$	Sm^{-1}
Porosity		
Cathode	0.46	
Anode	0.46	
Electrode volume fraction		
GDC	0.21	
Ag	0.79	
S_{TPB}		
Cathode layer	2.14×10^5	m^{2}m^{-3}
Anode layer	2.14×10^5	m^{2}m^{-3}

6.2.2.3 Mass transport model

In the porous electrode, gas diffusion occurs by means of both free molecular diffusion and Knudsen diffusion. Free molecular diffusion dominates in large pores and Knudsen diffusion becomes significant when pore sizes are comparable or smaller than molecular mean-free path. The extended Fick's model is used to describe gas transport in the porous electrodes as:

$$N_i = -\frac{1}{RT}\left(\frac{B_0 y_i P}{\mu}\frac{\partial \mathrm{P}}{\partial \mathrm{z}} - D_i^{eff}\frac{\partial (y_i \mathrm{P})}{\partial \mathrm{z}}\right)\ (i = 1, \dots, n) \quad (6.17)$$

Where N_i represents the flux of mass transport, B_0 is the permeability coefficient, y_i is the mole fraction of component i, μ is the dynamic viscosity of the gas and D_i^{eff} is the effective diffusivity of species i. In an SOEC where both molecular diffusion (D_{im}^{eff}) and Knudsen diffusion (D_{ik}^{eff}) are important, D_i^{eff} can be written as:

$$D_i^{eff} = (\frac{1}{D_{im}^{eff}} + \frac{1}{D_{ik}^{eff}}) \quad (6.18)$$

D_{im}^{eff} and D_{ik}^{eff} depend on the micro-structure of the porous electrode and operating conditions.

6.2.2.4 Momentum conservation model

The general Navier-Stokes equation is used to describe the momentum conservation. For momentum conservation in channels, the equation can be described as:

$$\rho \frac{\partial u}{\partial t} + \rho u \nabla u = -\nabla p + \nabla\left[\mu\left(\nabla u + (\nabla u)^T\right) - \frac{2}{3}\mu \nabla u\right] \quad (6.19)$$

For momentum conservation in porous electrodes and anode chamber, the equation is modified by including the Darcy's term for momentum conservation in the porous layer:

$$\rho \frac{\partial u}{\partial t} + \rho u \nabla u = -\nabla p + \nabla\left[\mu\left(\nabla u + (\nabla u)^T\right) - \frac{2}{3}\mu \nabla u\right] - \frac{\varepsilon \mu u}{K} \quad (6.20)$$

where ρ is the gas density, u is the velocity vector, p is pressure and ε is the porosity the electrode.

6.2.3 Boundary conditions

The electric potentials are specified at the outer boundaries of cathode and anode as working potential and zero potential, respectively. Insulation condition is applied to the bottom and top of the cell.

Inflow gas mole fraction is specified at cathode. The convective flux boundary condition is specified at the outlet of the cathode and anode. Zero flux is assumed at the end of anode chamber, electrolyte/electrode interface and the ends of electrodes.

Standard gas flow rate (SCCM) is specified at cathode while pressure condition is specified at the outlet. No slip condition is applied to the end of anode chamber, electrolyte/electrode interface and the ends of electrodes.

6.2.4 Model parameters

For model validation, the values of material property and operation parameters are consistent with experiments[138], as shown in Table 6.1, Table 6.2 and Table 6.3. The electrochemical characteristics of the model are validated by the experimental data using H_2 as SOFC fuel. The DC-SOFC exchange current density ($i_{0,co}$) is assumed to be 0.45 times of H_2-SOFC exchange current density ($i_{0,H2}$) as shown in experiments. The reaction rate of Boudouard reaction is affected by reaction area, activity of catalyst et al. These effects are validated by tuning the equilibrium parameter k_{rb}. The electrochemical parameters used in CA-SOEC are the same with those validated in DC-SOFC model due to the reversible characteristic of cell. The tuning parameters used for base-case simulation are summarized in Table 6.4. In parametric studies, those parameters are varied to evaluate their effects on the CA-SOEC performance.

6.2.5 Model solution

The model is solved by setting a certain cell voltage/inlet gas flow rate/temperature. The outputs of the model are the distributions of current density, species concentration, chemical reaction rates and others. The calculations are performed using the finite element commercial software COMSOL MULTIPHSICS®.

6.3 Results and discussion

6.3.1 Model validation

In this section, the modeling results of current-voltage characteristics are compared with experimental data for model validation. The comparison results between simulation and experimental data are shown in Fig. 6.2 and good agreement between them is observed. In the subsequent parametric simulation, the same cell structure parameters and tuning parameters are used and the length of the cell is extended to 90mm to increase the utilization of cathode gas. The operation temperature, voltage, inlet gas flow rate and the distance between carbon chamber and anode electrode (D_{ce}) are varied to study their effects on CA-SOEC performance.

Table 6.2 Operation parameters for model validation (H_2-SOFC)

Parameter	**Value**	**Unit**
Anode inlet gas flow rate for	50	SCCM
Cathode inlet gas flow rate	10	SCCM
Anode inlet gas composition	H_2 (97%) + H_2O (3%)	
Cathode inlet gas composition	Air	
Temperature	1123	K

Table 6.3 Operation parameters for model validation (DC-SOFC)

Parameter	**Value**	**Unit**
Distance between anode chamber and electrode, D_{ce}	59	µm
Cathode inlet gas flow rate	10	SCCM
Cathode gas composition	Air	
Temperature	1123	K

Table 6.4 Model tuning parameters

Parameter	**Value**	**Unit**
Cathode tortuosity	3	
Anode tortuosity	3	
H_2 exchange current density, i_{H_2}	1000	Am^{-2}
O_2 exchange current density i_{O_2}	400	Am^{-2}
CO exchange current density, i_{CO}	450	Am^{-2}
H_2 charge transfer coefficient, α_{H_2}	0.5	
CO charge transfer coefficient, α_{CO}	0.5	
O_2 charge transfer coefficient, α_{O_2}	0.5	
Equilibrium constant of Boudouard reaction	6×10^{13}	1/s

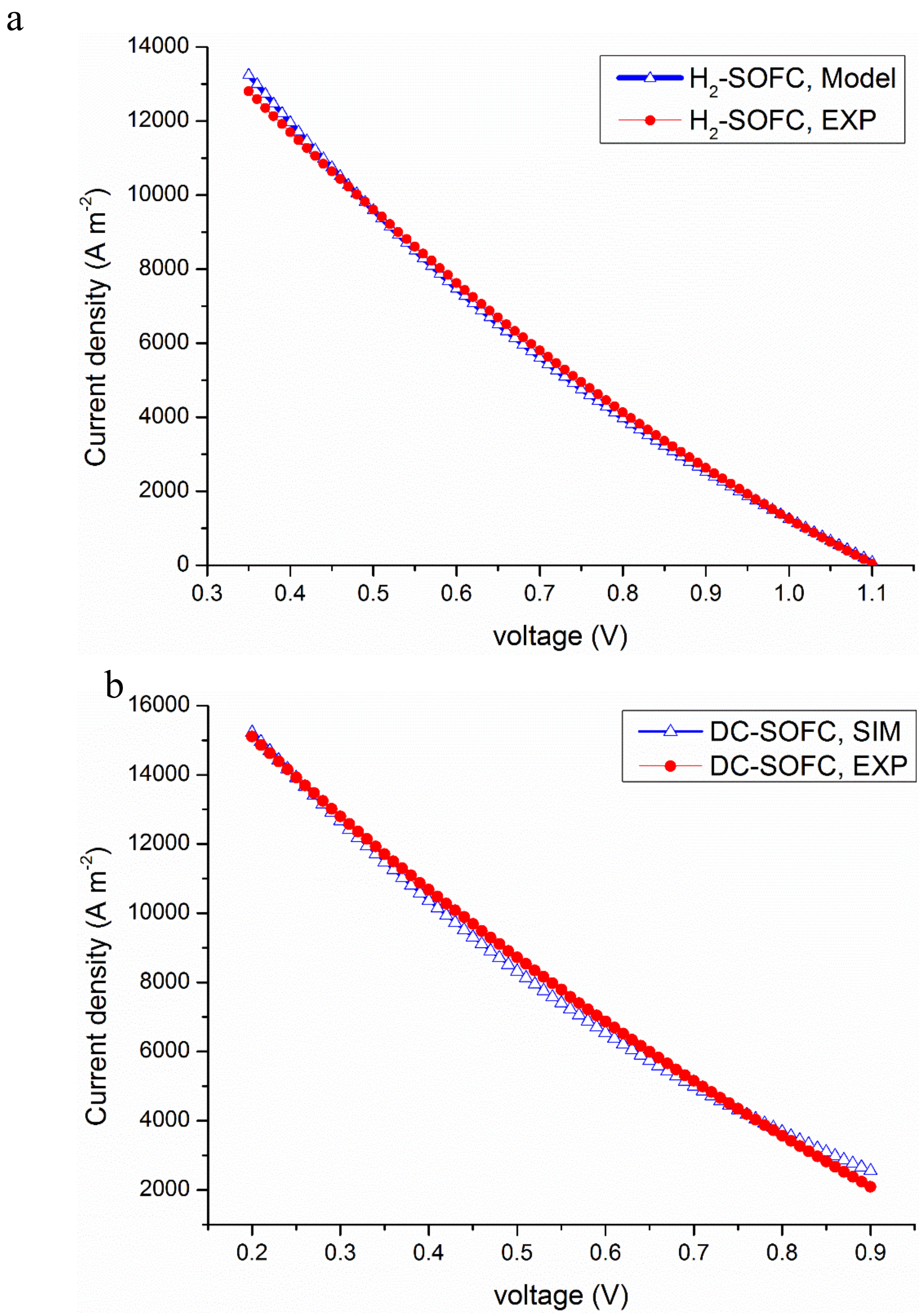

Figure 6.2 Model validation for (a) H_2-SOFC and (b) DC-SOFC

6.3.2 Effect of applied voltage

The effects of operating voltage on CA-SOEC electrolysis of H_2O and its detailed operation conditions are shown in Fig. 6.3 and Table 6.5, respectively.

Table 6.5 Operation parameters for operating potential effect study in DC-SOFC

Parameter	**Value**	**Unit**
Operating voltage	-0.1 – 0.7	V
Cathode inlet gas flow rate	100	SCCM
Cathode gas composition	H_2O	
Temperature	1123	K

Fig. 6.3 shows that the CA-SOEC can work both on fuel cell mode and electrolysis cell mode. When CA-SOEC is working at fuel cell mode, it generates electricity spontaneously and its open circuit voltage is about 0.7 V. In such a fuel cell, water is the oxidant, which is reduced to H_2 at cathode while carbon is oxidized at anode as fuel. The high short current density of CA-SOEC (3000 A m^{-2}) also indicates that it can generate hydrogen at a high rate even without any electrical power supplement.

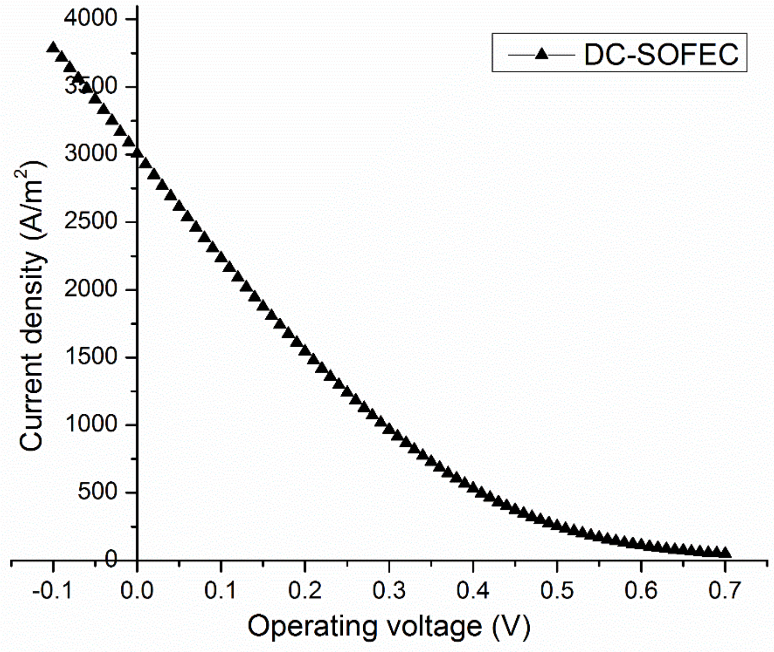

Figure 6.3 Effect of operating voltage on CA-SOEC performance at 1123K

Compared with conventional SOEC, CA-SOEC electrolysis not only operates at a much lower voltage, but also realizes gas-electricity co-generation. The co-generation is very attractive and enables SOEC to consume carbon for H_2 production at a high efficiency and a low cost.

It is also found that the molar fraction of CO at the anode outlet (Fig. 6.4) is very high (almost close to 1) under different operating voltages and the molar fraction of the rest gas (CO_2) is very low. On the other side (cathode), H_2 is generated by the electrolysis of H_2O in cathode. CO and H_2 produced separately at two different electrodes of CA-SOEC can be stored or mixed to produce syngas with any desired H_2/CO ratio, which can overcome the problem of syngas composition control in H_2O/CO_2 co-electrolysis by conventional SOEC. The easy control of syngas composition by CA-SOEC can greatly facilitate subsequent processes of syngas for various chemical or fuel generation.

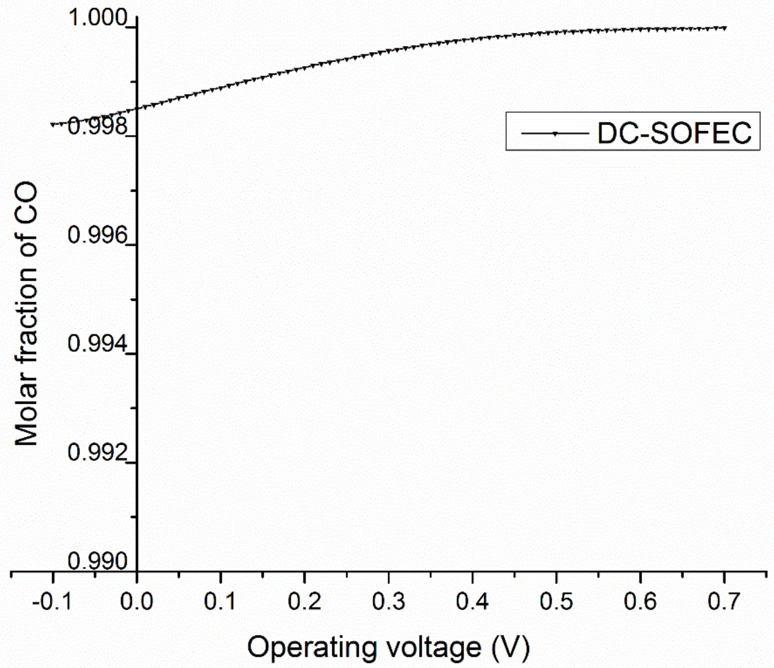

Figure 6.4 Effect of operating voltage on anode outlet CO molar fraction in CA-SOEC at 1123K.

6.3.3 Effect of operating temperature

The effects of operating temperature on CA-SOEC performance are shown in Fig. 6.5 and Fig. 6.6. The detailed operation conditions are shown in Table 6.6.

Table 6.6 Operation parameters for temperature effect study in DC-SOFC

Parameter	**Value**	**Unit**

Operating voltage	0, 0.2, 0.4, 0.6	V
Cathode inlet gas flow rate	100	SCCM
Cathode gas composition	H_2O	
Temperature	973 – 1203	K

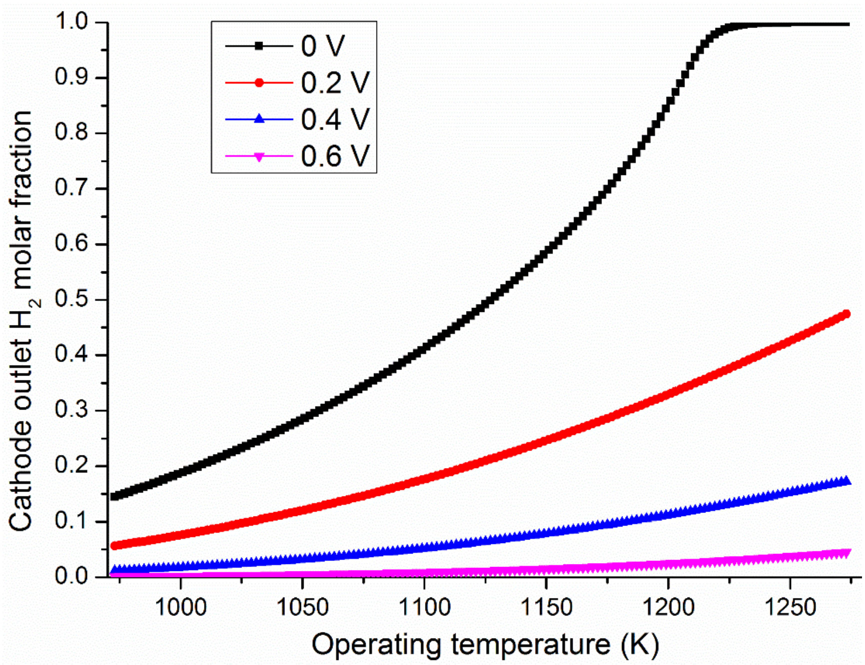

Figure 6.5 Effect of temperature on CA-SOEC cathode outlet H_2 molar faction at different operating voltages.

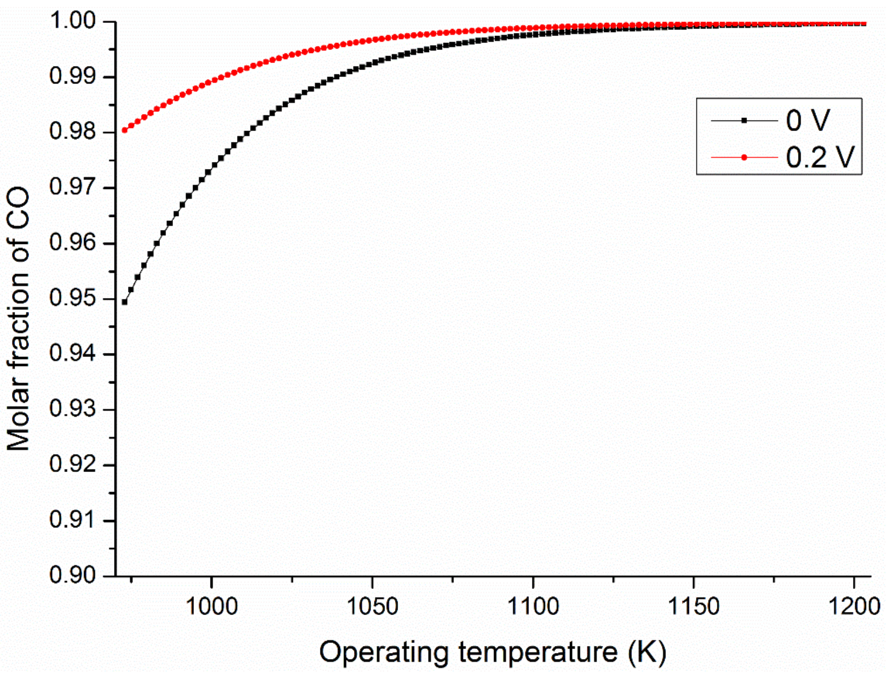

Figure 6.6 Effect of operating temperature on anode outlet CO molar fraction in CA-SOEC at 0V and 0.2V operating voltages.

It is found that the H_2 molar fraction at the cathode outlet of CA-SOEC increases significantly with increasing temperature at a low operating voltage such as 0.2V or 0V. However, the H_2 molar fraction only increases slightly at a higher operating voltage, i.e. 0.4V and 0.6V. This phenomenon is due to the temperature-dependence of the electrochemical/chemical reaction kinetics and the ionic conductivity. The increased temperature can increase the electrochemical reaction kinetics, ionic conductivity, and the Boudouard reaction rate. As a higher rate of Boudouard reaction can produce more CO, it can increase the anode partial equilibrium potential thus increase the current density at a given operating voltage. In addition, the concentration overpotential is very significant when the current density is high, especially when the gas concentration at the TPB is close to zero. The higher CO concentration can significantly enlarge the limiting current density, thus significantly improve the performance of CA-SOEC at a high current density (or low operating voltage). When the operating voltage is close to 0, the H_2 molar fraction at the cathode outlet can reach almost 100%. Under this condition, the CA-SOEC is actually an electrochemical reactor, producing H_2 and CO at the two electrodes without generating or consuming electricity. For comparison, in the conventional chemical reactors based on reforming reaction to convert carbon or hydrocarbon fuels for syngas production, both H_2 and CO are produced in the same reactor and it is usually difficult to control the gas composition. In the proposed CA-SOEC, it is feasible to collect pure H_2 from CA-SOEC at a reasonably high temperature and the CO molar fraction at the anode outlet can also be kept at a high level as shown in Fig. 6.6. The overall benefits resulted by higher temperature is a higher output current density (at a given voltage) and a higher anode outlet CO molar fraction as well. To this end, it indicates that CA-SOEC has a great potential for electricity and syngas cogeneration at high temperature.

6.3.4 Effect of gas flow rate at the cathode inlet

The gas flow rate at the cathode inlet is also varied to examine its effect on CA-SOEC electrolysis of H_2O at different applied potentials and temperature. This gas flow rate changes from 50 SCCM to 300 SCCM with different applied voltages and temperatures. More detailed operation conditions can be seen in Table 6.7.

Table 6.7 Operation parameters for inlet H_2O flow rate effect study in DC-SOFC

Parameter	**Value**	**Unit**
Operating voltage	0, 0.2	V
Cathode inlet gas flow rate	50 – 300	SCCM
Cathode gas composition	H_2O	
Temperature	1073, 1173	K

A higher flow rate of the H_2O leads to higher reactant concentration in the downstream, which helps increase the cathode partial equilibrium potential and overall cell performance. However, increasing higher cathode flow rate also brings the problem of low reactant utilization as can be seen in Fig. 6.7: when the cathode flow rate is small, almost 100% H_2O can be converted to H_2 at high temperature (1173K) and 0V voltage. At lower temperature and higher operating voltage, the conversion ratio of H_2O decreases quickly. Therefore, a higher temperature is favored and the cathode flow rated should be carefully considered as it is not only related with the reactant utilization but also the extra pump work. The determination of the optimal flow rate requires a detailed thermodynamic analysis.

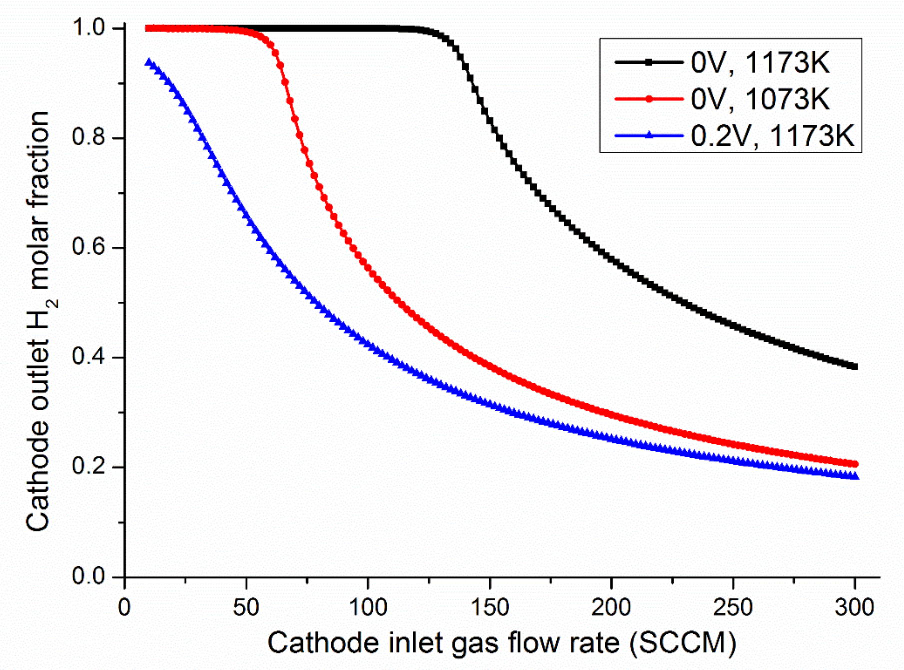

Figure 6.7 Effect of cathode inlet gas flow rate on outlet H_2 molar fraction at 1073K and 1173K operating temperatures and 0V and 0.2V operating voltages.

6.3.5 Effect of distance between carbon and anode electrode

Since the source of CO for electricity generation is the Boudouard reaction between carbon (from carbon chamber) and CO_2 (from electrochemical reaction in anode electrode), the transport of CO from carbon chamber to anode TPB sites and CO_2 from TPB sites to carbon chamber is crucial to cell performance. When the cell is placed in a flatwise orientation, the distance between carbon surface and upside anode surface becomes larger as carbon is continuously consumed. Even though the bottom of carbon bed touches the anode, there is a distance between upside of carbon bed and the upside anode surface. It is expected that the distance between carbon chamber and anode electrode, noted as D_{ce}, play an important role in the transport of CO and CO_2, which is discussed in this section from the simulated results in Fig. 6.8 and Fig. 6.9. The detailed operation conditions are shown in Table 6.8.

Table 6.8 Operation parameters for D_{ce} effect study in DC-SOFC

Parameter	**Value**	**Unit**
Operating voltage	0	V

Distance between anode chamber and electrode, D_{ce}	59 – 4559	µm
Cathode inlet gas flow rate	100	SCCM
Cathode gas composition	H_2O	
Temperature	1073 – 1273	K

As expected, the cathode outlet H_2 molar fraction of CA-SOEC increases with decreasing D_{ce} (Fig. 6.8). Compared with low operating temperature, the performance of CA-SOEC working at a high temperature has a much higher improvement with decreasing D_{ce}. This phenomenon is caused by both gas transport and electrochemical reaction rate. Besides, a higher temperature ensures a high outlet H_2 molar fraction even at larger D_{ce} conditions. As can be seen in Fig. 6.9, the molar fraction of CO at anode outlet is very close in different D_{ce} conditions at high temperature. When D_{ce} is very small ($D_{ce} = 59\mu m$), the CO fraction in anode electrode is very close to 1. As D_{ce} is increased, the transport of CO from carbon chamber to anode active sites (TPB) becomes more difficult. Thus, the molar fraction of CO decreases in anode active sites with the increase of D_{ce} especially at a low temperature (973K).

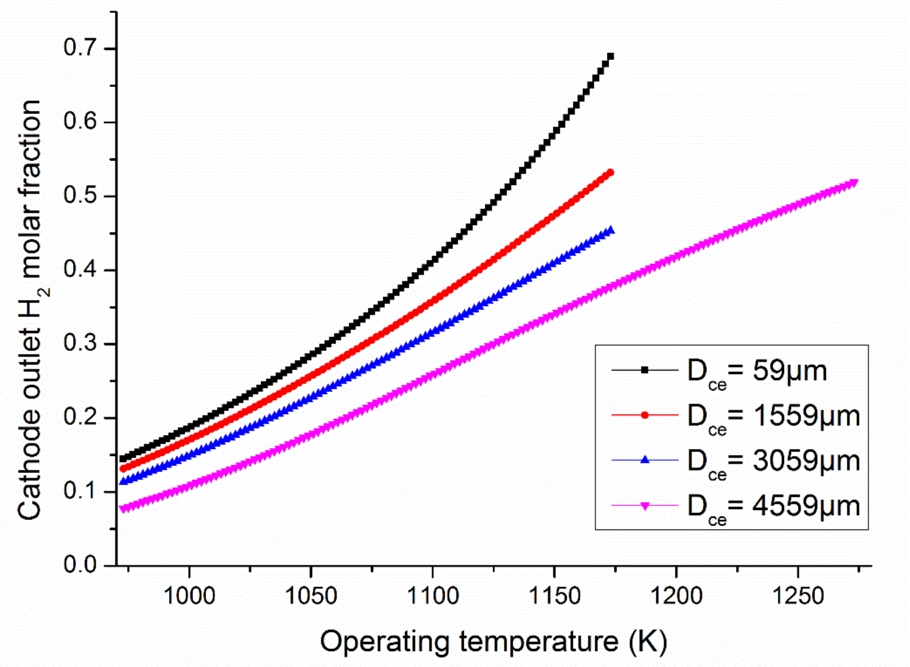

Figure 6.8 Effect of operating temperature on cathode outlet H_2 molar fraction at different D_{ce} situations.

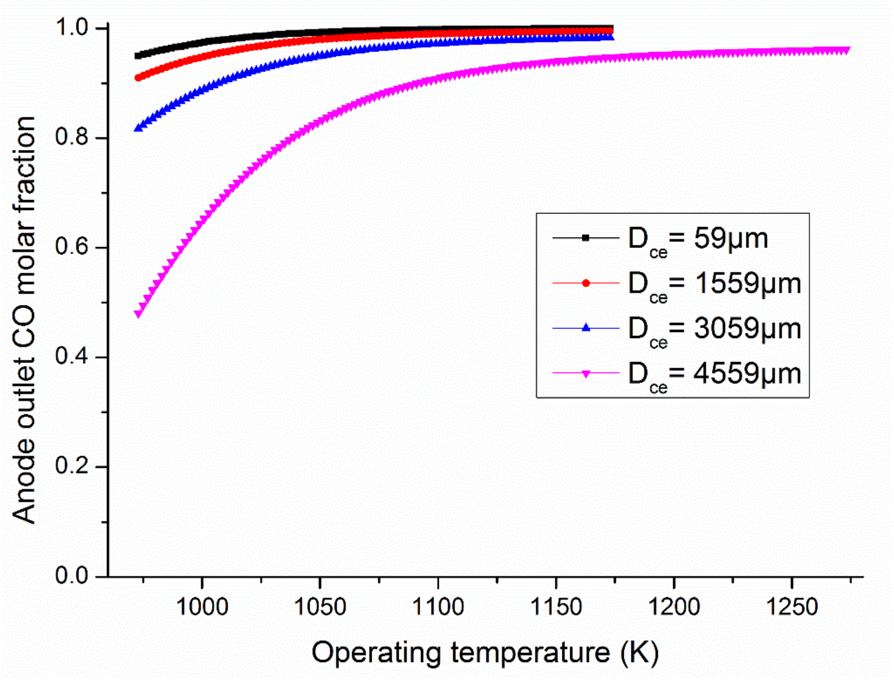

Figure 6.9 Effect of operating temperature on anode outlet CO molar fraction at different D_{ce} situations

6.4 Conclusions

A multi-physics FEM model including electrochemical reactions, chemical reactions, ion/electronic charge transport, mass transport and momentum transport is developed to characterize the performance of a CA-SOEC. The model is validated by comparing the simulation results with experimental date of Liu's group.

It is found that the performance of CA-SOEC is highly dependent on the operating temperature. At a higher temperature, CA-SOEC can co-generate electricity and CO simultaneously in a more efficient way. For comparison, the performance of CA-SOEC is greatly reduced at a low temperature due to the low Boudouard reaction rate. Compared with conventional H_2O/CO_2 co-electrolysis for syngas production, CA-

SOEC is advantageous as H_2 and CO are produced at two different electrodes. The separate generation of H_2 and CO allows easy control of syngas composition, which is critical for subsequent chemical or fuel production.

It is also found that the performance of CA-SOEC is largely affected by the distance between carbon chamber and anode electrode D_{ce}. With the increase of D_{ce}, the performance of CA-SOEC decreases, demonstrating that a smaller D_{ce} is recommended in the design of CA-SOEC in real applications for co-generation. Another point that should be noted is the choice of cathode inlet gas flow rate by considering the reactant utilization and pump work.

A new carbon deliver system need to be well designed for CA-SOEC's continuous operation. And the most efficient operation condition depends on the actual demand. If only CO and H_2 is needed, a short current operating condition is recommended. If both electricity and syngas are needed, then a more detailed energy/exergy analysis is also needed in the future.

CONCLUSION

Utilizing solid carbon in SOFCs not only improves the energy conversion efficiency from chemical energy to electricity of the solid carbon, but also decreases the fuel cost of the SOFC, which makes SOFCs more competitive in the market. This paper focused on the detailed analysis of chemical/physical processes in DC-SOFCs through validated numerical models. Experiments are also conducted to study the effects of different gasification agents on the performance of DC-SOFCs. Moreover, the concept of CA-SOEC is proposed to generate H_2 and CO at two different electrodes by electrolyzing H_2O.

1 Numerical models are developed for electricity and CO co-generation in DC-SOFC

(1) D_{ce} is an important factor to the performance of DC-SOFC. A large D_{ce} results in a low performance of DC-SOFC due to the limited transportation of CO from carbon layer to anode.

(2) Operating temperature is another key factor to DC-SOFC's performance. High temperature facilitates both chemical reaction (carbon gasification) and electrochemical reactions (fuel oxidation and oxygen reduction) as well as ion transport through the dense electrolyte, which maintains the large molar fraction of CO electrochemical reaction sites to get a better performance.

(3) The high molar fraction of CO at the outlet offer the promising potential for electricity and CO co-generation in DC-SOFCs.

(4) The current density of DC-SOFC is found to slightly increase along the cell length due to the generation of CO along the cell length, which is different from SOFCs fed with H_2 fuel.

(5) The anode-supported DC-SOFC has a much better electrical power output than that of an electrolyte-supported DC-SOFC. However, the anode-supported configuration is not favorable for CO generation, especially at a large D_{ce}.

2 Thermal effects in DC-SOFCs are investigated

(1) The operating potential has a great effect on the temperature distribution of the cell. The small operating potential results in the high overall cell temperature

(2) Most of the heat is generated from anode electrode, where heat generated from entropy change is the majority part compared with other processes.

(3) Cathode inlet gas temperature plays an important role on the temperature distribution of the cell. At high operating potential, cathode inlet gas functions as the outer heat source and it works as the outer heat sink at low operating potential.

(4) The temperature gradient increases quickly along the cell width with the increase of D_{ce} due to the small thermal conductivity of the gas.

3 Experiments and numerical models are conducted to systematically study the performance of the proposed new DC-SOFC with H_2O gasification agent

(1) H_2O-assisted DC-SOFCs has a much higher fuel concentration in anode than CO_2-assisted DC-SOFCs.

(2) Coupled with faster electrochemical reaction kinetics by H_2 fuel, using H_2O as agent significantly improves the performance of DC-SOFCs compared with CO_2 agent.

(3) H_2O-assisted DC-SOFC allows the operation at reduced operating temperature.

(4) A high anode inlet gas flow rate is not necessary for DC-SOFCs.

4 The effects of catalytical in-situ steam-carbon gasification on the performance of DC-SOFCs are studied.

(1) In-situ catalytic steam-carbon gasification largely increases the gas fuel production rate and significantly improves the performance of the DC-SOFC.

(2) The high fuel percentage in anode outlet gas can be obtained.

(3) The mole fraction of H_2 and CO in the outlet gas can be adjusted by controlling the inlet gas flow rate.

(4) The operating temperature significantly affects the fuel composition in outlet gas, and it is possible for fuel and electricity co-generation in DC-SOFC at high temperature.

5 Models are developed for syngas generation by H_2O electrolysis in a CA-SOEC.

(1) At high temperatures, the CA-SOEC can co-generate electricity and CO simultaneously.

(2) In CA-SOEC, H_2 and CO are produced at two different electrodes, which allows easy control of syngas composition.

(3) The performance of CA-SOEC is largely affected by D_{ce}. A smaller D_{ce} is recommended in the design of DC-SOFEC in real applications for co-generation.

Future Work

Based on the work in this paper, there are still several studied to be conducted in the future:

1. **Develop models for the study of thermal effects of DC-SOFCs with H_2O as gasification agent.**

   The thermal effects related to detailed temperature distribution are not considered in the previous numerical model of DC-SOFCs with H_2O as gasification agent due to the small size of the cell. In the future, the model should be extended to a larger size and related parametric studies should be conducted.

2. **Thermodynamic efficiency analysis of DC-SOFCs with H_2O as gasification agent.**

   With in-situ steam gasification reaction, the heat released from SOFC can be utilized by chemical reactions in the anode. The efficiency of DC-SOFC can thus be significantly higher than SOFC. Therefore, it is very important to develop numerical models for its thermodynamic analysis.

3. **Syngas production characteristics of CA-SOECs with H_2O as gasification agent.**

   In the CA-SOECs for steam electrolysis, H_2 can be generated in the cathode while both H_2 and CO are generated in the anode. Therefore, a higher H_2 ratio can hopefully be obtained in the syngas of SOEC outlet. Furthermore, most of H_2 in the outlet syngas is separated, which means the ratio of H_2 to CO can be more flexibly adjusted in CA-SOECs compared with H_2O and CO co-electrolysis in SOECs. It is very meaningful to develop such numerical models for the study of flexible syngas generation in CA-SOECs.

References

[1] Cao T, Huang K, Shi Y, Cai N. Recent advances in high-temperature carbon-air fuel cells. Energy & Environmental Science. 2017;10:460-90.

[2] Jiang C, Ma J, Corre G, Jain SL, Irvine JTS. Challenges in developing direct carbon fuel cells. Chemical Society Reviews. 2017.

[3] Gür TM. Comprehensive review of methane conversion in solid oxide fuel cells: Prospects for efficient electricity generation from natural gas. Progress in Energy and Combustion Science. 2016;54:1-64.

[4] Sharma M, N R, Dasappa S. Solid oxide fuel cell operating with biomass derived producer gas: Status and challenges. Renewable and Sustainable Energy Reviews. 2016;60:450-63.

[5] Rady AC, Giddey S, Badwal SPS, Ladewig BP, Bhattacharya S. Review of Fuels for Direct Carbon Fuel Cells. Energy & Fuels. 2012;26:1471-88.

[6] Xuan J, Leung MKH, Leung DYC, Ni M. A review of biomass-derived fuel processors for fuel cell systems. Renewable and Sustainable Energy Reviews. 2009;13:1301-13.

[7] Liu R, Zhao C, Li J, Zeng F, Wang S, Wen T, et al. A novel direct carbon fuel cell by approach of tubular solid oxide fuel cells. Journal of Power Sources. 2010;195:480-2.

[8] Fuente-Cuesta A, Jiang C, Arenillas A, Irvine JTS. Role of coal characteristics in the electrochemical behaviour of hybrid direct carbon fuel cells. Energy & Environmental Science. 2016;9:2868-80.

[9] Antunes R, Skrzypkiewicz M. Chronoamperometric investigations of electro-oxidation of lignite in direct carbon bed solid oxide fuel cell. International Journal of Hydrogen Energy. 2015;40:4357-69.

[10] Giddey S, Badwal SPS, Kulkarni A, Munnings C. A comprehensive review of direct carbon fuel cell technology. Progress in Energy and Combustion Science. 2012;38:360-99.

[11] Costamagna P, Costa P, Antonucci V. Micro-modelling of solid oxide fuel cell electrodes. Electrochimica Acta. 1998;43:375-94.

[12] Park S, Vohs JM, Gorte RJ. Direct oxidation of hydrocarbons in a solid-oxide fuel cell. Nature. 2000;404:265-7.

[13] Chan SH, Xia ZT. Anode Micro Model of Solid Oxide Fuel Cell. J Electrochem Soc. 2001;148:A388-A94.

[14] Lazzaretto A, Toffolo A, Zanon F. Parameter Setting for a Tubular SOFC Simulation Model. Journal of Energy Resources Technology. 2004;126:40-6.

[15] Klein JM, Bultel Y, Georges S, Pons M. Modeling of a SOFC fuelled by methane: From direct internal reforming to gradual internal reforming. Chemical Engineering Science. 2007;62:1636-49.

[16] Singhal SC. Advances in solid oxide fuel cell technology. Solid State Ionics. 2000;135:305-13.

[17] Ormerod RM. Solid oxide fuel cells. Chemical Society Reviews. 2003;32:17-28.

[18] Minh NQ. Solid oxide fuel cell technology—features and applications. Solid State Ionics. 2004;174:271-7.

[19] Andersson M, Yuan J, Sundén B. SOFC modeling considering hydrogen and carbon monoxide as electrochemical reactants. Journal of Power Sources. 2013;232:42-54.

[20] Ni M. Is steam addition necessary for the landfill gas fueled solid oxide fuel cells? International Journal of Hydrogen Energy. 2013;38:16373-86.

[21] Saunders JEA, Davy MH. In-situ studies of gas phase composition and anode surface temperature through a model DIR-SOFC steam–methane reformer at 973.15 K. International Journal of Hydrogen Energy. 2013;38:13762-73.

[22] Sun Q, Zheng K, Ni M. Thermodynamic Analysis of Methane-fueled Solid Oxide Fuel Cells Considering CO Electrochemical Oxidation. Chinese Journal of Chemical Engineering. 2014;22:1033-7.

[23] Bao C, Jiang Z, Zhang X. Mathematical modeling of synthesis gas fueled electrochemistry and transport including H2/CO co-oxidation and surface diffusion in solid oxide fuel cell. Journal of Power Sources. 2015;294:317-32.

[24] Hua B, Yan N, Li M, Zhang Y-q, Sun Y-f, Li J, et al. Novel layered solid oxide fuel cells with multiple-twinned Ni0.8Co0.2 nanoparticles: the key to thermally independent CO2 utilization and power-chemical cogeneration. Energy & Environmental Science. 2016.

[25] Huang H, Zhou X, Liu H. A CFD model for partial oxidation of methane over self-sustained electrochemical promotion catalyst. International Journal of Hydrogen Energy. 2016;41:208-18.

[26] Ni M. Modeling and parametric simulations of solid oxide fuel cells with methane carbon dioxide reforming. Energy Conversion and Management. 2013;70:116-29.

[27] Kee RJ, Zhu H, Goodwin DG. Solid-oxide fuel cells with hydrocarbon fuels. Proceedings of the Combustion Institute. 2005;30:2379-404.

[28] Zhu H, Kee RJ. Thermodynamics of SOFC efficiency and fuel utilization as functions of fuel mixtures and operating conditions. Journal of Power Sources. 2006;161:957-64.

[29] Gupta GK, Hecht ES, Zhu H, Dean AM, Kee RJ. Gas-phase reactions of methane and natural-gas with air and steam in non-catalytic regions of a solid-oxide fuel cell.

Journal of Power Sources. 2006;156:434-47.

[30] Zhan Z, Kobsiriphat W, Wilson JR, Pillai M, Kim I, Barnett SA. Syngas Production By Coelectrolysis of CO2/H2O: The Basis for a Renewable Energy Cycle. Energy & Fuels. 2009;23:3089-96.

[31] Chen B, Xu H, Chen L, Li Y, Xia C, Ni M. Modelling of One-Step Methanation Process Combining SOECs and Fischer-Tropsch-like Reactor. J Electrochem Soc. 2016;163:F3001-F8.

[32] Cinti G, Baldinelli A, Di Michele A, Desideri U. Integration of Solid Oxide Electrolyzer and Fischer-Tropsch: A sustainable pathway for synthetic fuel. Applied Energy. 2016;162:308-20.

[33] Lei L, Wang Y, Fang S, Ren C, Liu T, Chen F. Efficient syngas generation for electricity storage through carbon gasification assisted solid oxide co-electrolysis. Applied Energy. 2016;173:52-8.

[34] Pu T, Tan W, Shi H, Na Y, Lu J, Zhu B. Steam/CO2 electrolysis in symmetric solid oxide electrolysis cell with barium cerate-carbonate composite electrolyte. Electrochimica Acta. 2016;190:193-8.

[35] Zhang W, Yu B, Wang X, Chen J. Thermodynamic analysis of the efficiency of high temperature co-electrolysis system for syngas production. International Journal of Hydrogen Energy. 2016;41:15960-9.

[36] Chen B, Xu H, Ni M. Modelling of SOEC-FT reactor: Pressure effects on methanation process. Applied Energy. 2017;185, Part 1:814-24.

[37] Graves C, Ebbesen SD, Mogensen M. Co-electrolysis of CO2 and H2O in solid oxide cells: Performance and durability. Solid State Ionics. 2011;192:398-403.

[38] Li W, Wang H, Shi Y, Cai N. Performance and methane production characteristics of H2O–CO2 co-electrolysis in solid oxide electrolysis cells. International Journal of Hydrogen Energy. 2013;38:11104-9.

[39] Kazempoor P, Braun RJ. Hydrogen and synthetic fuel production using high temperature solid oxide electrolysis cells (SOECs). International Journal of Hydrogen Energy. 2015;40:3599-612.

[40] Ni M, Leung MKH, Leung DYC. Parametric study of solid oxide steam electrolyzer for hydrogen production. International Journal of Hydrogen Energy. 2007;32:2305-13.

[41] Ni M, Leung MKH, Leung DYC. Mathematical modeling of the coupled transport and electrochemical reactions in solid oxide steam electrolyzer for hydrogen production. Electrochimica Acta. 2007;52:6707-18.

[42] Udagawa J, Aguiar P, Brandon NP. Hydrogen production through steam electrolysis: Model-based steady state performance of a cathode-supported intermediate temperature solid oxide electrolysis cell. Journal of Power Sources. 2007;166:127-36.

[43] Luo Y, Li W, Shi Y, Cao T, Ye X, Wang S, et al. Experimental Characterization and Theoretical Modeling of Methane Production by H2O/CO2 Co-Electrolysis in a Tubular Solid Oxide Electrolysis Cell. J Electrochem Soc. 2015;162:F1129-F34.

[44] Ni M, Leung MKH, Leung DYC. Technological development of hydrogen production by solid oxide electrolyzer cell (SOEC). International Journal of Hydrogen Energy. 2008;33:2337-54.

[45] Ni M, Leung MKH, Leung DYC. Electrochemical modeling of hydrogen production by proton-conducting solid oxide steam electrolyzer. International Journal of Hydrogen Energy. 2008;33:4040-7.

[46] Ebbesen SD, Mogensen M. Electrolysis of carbon dioxide in Solid Oxide Electrolysis Cells. Journal of Power Sources. 2009;193:349-58.

[47] Ni M. Computational fluid dynamics modeling of a solid oxide electrolyzer cell for hydrogen production. International Journal of Hydrogen Energy. 2009;34:7795-806.

[48] Stoots C, O'Brien J, Hartvigsen J. Results of recent high temperature coelectrolysis studies at the Idaho National Laboratory. International Journal of Hydrogen Energy. 2009;34:4208-15.

[49] Ni M. Modeling of a solid oxide electrolysis cell for carbon dioxide electrolysis. Chemical Engineering Journal. 2010;164:246-54.

[50] Laguna-Bercero MA. Recent advances in high temperature electrolysis using solid oxide fuel cells: A review. Journal of Power Sources. 2012;203:4-16.

[51] Ni M. 2D thermal modeling of a solid oxide electrolyzer cell (SOEC) for syngas production by H2O/CO2 co-electrolysis. International Journal of Hydrogen Energy. 2012;37:6389-99.

[52] Ni M. An electrochemical model for syngas production by co-electrolysis of H2O and CO2. Journal of Power Sources. 2012;202:209-16.

[53] Ni M, Leung MKH, Leung DYC. Micro-scale modelling of solid oxide fuel cells with micro-structurally graded electrodes. Journal of Power Sources. 2007;168:369-78.

[54] Zhu H, Kee RJ. Two-dimensional model of distributed charge transfer and internal reforming within unit cells of segmented-in-series solid-oxide fuel cells. Journal of Power Sources. 2011;196:7654-64.

[55] Andersson M, Yuan J, Sundén B. Grading the Amount of Electrochemical Active Sites along the Main Flow Direction of an SOFC. J Electrochem Soc. 2013;160:F1-F12.

[56] Guo Y, Bessaa M, Aguado S, Steil MC, Rembelski D, Rieu M, et al. An all porous solid oxide fuel cell (SOFC): a bridging technology between dual and single chamber SOFCs. Energy & Environmental Science. 2013;6:2119-23.

[57] Hosseini S, Ahmed K, Tadé MO. CFD model of a methane fuelled single cell SOFC stack for analysing the combined effects of macro/micro structural parameters. Journal of Power Sources. 2013;234:180-96.

[58] Li W, Shi Y, Luo Y, Cai N. Theoretical modeling of air electrode operating in SOFC mode and SOEC mode: The effects of microstructure and thickness. International Journal of Hydrogen Energy. 2014;39:13738-50.

[59] Cui D, Tu B, Cheng M. Effects of cell geometries on performance of tubular solid oxide fuel cell. Journal of Power Sources. 2015;297:419-26.

[60] Guo YM, Largiller G, Guizard C, Tardivat C, Farrusseng D. Coke-free operation of an all porous solid oxide fuel cell (AP-SOFC) used as an O2 supply device. Journal of Materials Chemistry A. 2015;3:2684-9.

[61] Lin B, Shi Y, Ni M, Cai N. Numerical investigation on impacts on fuel velocity distribution nonuniformity among solid oxide fuel cell unit channels. International Journal of Hydrogen Energy. 2015;40:3035-47.

[62] Nelson GJ. An analytical approach for solid oxide cell electrode geometric design. Journal of Power Sources. 2015;300:365-75.

[63] Chen B, Xu H, Ni M. Modelling of finger-like channelled anode support for SOFCs application. Science Bulletin. 2016:1-9.

[64] Shimada H, Suzuki T, Yamaguchi T, Sumi H, Hamamoto K, Fujishiro Y. Challenge for lowering concentration polarization in solid oxide fuel cells. Journal of Power Sources. 2016;302:53-60.

[65] Shi Y, Luo Y, Cai N, Qian J, Wang S, Li W, et al. Experimental characterization and modeling of the electrochemical reduction of CO2 in solid oxide electrolysis cells. Electrochimica Acta. 2013;88:644-53.

[66] Zhang H, Wang J, Su S, Chen J. Electrochemical performance characteristics and optimum design strategies of a solid oxide electrolysis cell system for carbon dioxide reduction. International Journal of Hydrogen Energy. 2013;38:9609-18.

[67] Stempien JP, Liu Q, Ni M, Sun Q, Chan SH. Physical principles for the calculation of equilibrium potential for co-electrolysis of steam and carbon dioxide in a Solid Oxide Electrolyzer Cell (SOEC). Electrochimica Acta. 2014;147:490-7.

[68] Zhang J, Shi Y, Cai N. An approximate analytical model of reduction of carbon dioxide in solid oxide electrolysis cell by regular and singular perturbation methods. Electrochimica Acta. 2014;139:190-200.

[69] Luo Y, Li W, Shi Y, Ye X, Wang S, Cai N. Methane Synthesis Characteristics of H2O/CO2 Co-Electrolysis in Tubular Solid Oxide Electrolysis Cells. ECS Transactions. 2015;68:3465-74.

[70] Stempien JP, Ni M, Sun Q, Chan SH. Thermodynamic analysis of combined Solid Oxide Electrolyzer and Fischer–Tropsch processes. Energy. 2015;81:682-90.

[71] Stempien JP, Ni M, Sun Q, Chan SH. Production of sustainable methane from renewable energy and captured carbon dioxide with the use of Solid Oxide Electrolyzer: A thermodynamic assessment. Energy. 2015;82:714-21.

[72] Torrell M, Garcia-Rodriguez S, Morata A, Penelas G, Tarancon A. Co-electrolysis of steam and CO2 in full-ceramic symmetrical SOECs: a strategy for avoiding the use of hydrogen as a safe gas. Faraday Discussions. 2015.

[73] NETL. Fuel Cell Handbook, Seventh Edition. DOE/NETL; 2004. p. CD.

[74] Ni M, Leung DYC, Leung MKH. Thermodynamic analysis of ammonia fed solid oxide fuel cells: Comparison between proton-conducting electrolyte and oxygen ion-conducting electrolyte. Journal of Power Sources. 2008;183:682-6.

[75] Sun X, Chen M, Jensen SH, Ebbesen SD, Graves C, Mogensen M. Thermodynamic analysis of synthetic hydrocarbon fuel production in pressurized solid oxide electrolysis cells. International Journal of Hydrogen Energy. 2012;37:17101-10.

[76] Rokni LPM. Thermodynamic Analysis of an Integrated Gasification Solid Oxide Fuel Cell Plant with a Kalina Cycle. International Journal of Green Energy. 2015;12:610-9.

[77] Zhang X, Ni M, Dong F, He W, Chen B, Xu H. Thermodynamic analysis and performance optimization of solid oxide fuel cell and refrigerator hybrid system based on H2 and CO. Applied Thermal Engineering. 2016;108:347-52.

[78] Li W, Shi Y, Luo Y, Cai N. Elementary reaction modeling of solid oxide electrolysis cells: Main zones for heterogeneous chemical/electrochemical reactions. Journal of Power Sources. 2015;273:1-13.

[79] Xu H, Chen B, Ni M. Modeling of Direct Carbon-Assisted Solid Oxide Electrolysis Cell (SOEC) for Syngas Production at Two Different Electrodes. J Electrochem Soc. 2016;163:F3029-F35.

[80] Johnson DU, Mitchell RE, Gür TM. Modeling Power Production in a Tubular Carbon Fuel Cell. ECS Transactions. 2014;61:235-43.

[81] Yu X, Shi Y, Wang H, Cai N, Li C, Ghoniem AF. Using potassium catalytic gasification to improve the performance of solid oxide direct carbon fuel cells: Experimental characterization and elementary reaction modeling. Journal of Power Sources. 2014;252:130-7.

[82] Alexander BR, Mitchell RE, Gür TM. Modeling of experimental results for carbon utilization in a carbon fuel cell. Journal of Power Sources. 2013;228:132-40.

[83] Li W, Shi Y, Luo Y, Cai N. Elementary reaction modeling of CO2/H2O co-electrolysis cell considering effects of cathode thickness. Journal of Power Sources. 2013;243:118-30.

[84] Yu X, Shi Y, Wang H, Cai N, Li C, Tomov RI, et al. Experimental characterization and elementary reaction modeling of solid oxide electrolyte direct carbon fuel cell.

Journal of Power Sources. 2013;243:159-71.

[85] Alexander BR, Mitchell RE, Gür TM. Experimental and Modeling Study of Biomass Conversion in a Solid Carbon Fuel Cell. J Electrochem Soc. 2012;159:B347-B54.

[86] Andersson M, Yuan J, Sundén B. SOFC modeling considering electrochemical reactions at the active three phase boundaries. International Journal of Heat and Mass Transfer. 2012;55:773-88.

[87] Yurkiv V, Utz A, Weber A, Ivers-Tiffée E, Volpp H-R, Bessler WG. Elementary kinetic modeling and experimental validation of electrochemical CO oxidation on Ni/YSZ pattern anodes. Electrochimica Acta. 2012;59:573-80.

[88] Chen D, Bi W, Kong W, Lin Z. Combined micro-scale and macro-scale modeling of the composite electrode of a solid oxide fuel cell. Journal of Power Sources. 2010;195:6598-610.

[89] Dokmaingam P, Irvine JTS, Assabumrungrat S, Charojrochkul S, Laosiripojana N. Modeling of IT-SOFC with indirect internal reforming operation fueled by methane: Effect of oxygen adding as autothermal reforming. International Journal of Hydrogen Energy. 2010;35:13271-9.

[90] Ni M. Modeling of a planar solid oxide fuel cell based on proton-conducting electrolyte. International Journal of Energy Research. 2010;34:1027-41.

[91] Ni M. Thermo-electrochemical modeling of ammonia-fueled solid oxide fuel cells considering ammonia thermal decomposition in the anode. International Journal of Hydrogen Energy. 2011;36:3153-66.

[92] Shi Y, Li C, Cai N. Experimental characterization and mechanistic modeling of carbon monoxide fueled solid oxide fuel cell. Journal of Power Sources. 2011;196:5526-37.

[93] Ni M. 2D heat and mass transfer modeling of methane steam reforming for hydrogen production in a compact reformer. Energy Conversion and Management. 2013;65:155-63.

[94] Ni M. On the source terms of species equations in fuel cell modeling. International Journal of Hydrogen Energy. 2009;34:9543-4.

[95] Ni M, Leung DYC, Leung MKH. Erratum to “Modeling of methane fed solid oxide fuel cells: Comparison between proton conducting electrolyte and oxygen ion conducting electrolyte” [J. Power Sources 183 (2008) 133–142]. Journal of Power Sources. 2009;194:1226-7.

[96] Kakaç S, Pramuanjaroenkij A, Zhou XY. A review of numerical modeling of solid oxide fuel cells. International Journal of Hydrogen Energy. 2007;32:761-86.

[97] Zhang H, Chen J, Zhang J. Performance analysis and parametric study of a solid oxide fuel cell fueled by carbon monoxide. International Journal of Hydrogen Energy. 2013;38:16354-64.

[98] Chen B, Xu H, Zhang H, Tan P, Cai W, Ni M. A novel design of solid oxide electrolyser integrated with magnesium hydride bed for hydrogen generation and storage – A dynamic simulation study. Applied Energy. 2017;200:260-72.

[99] Xu H, Chen B, Tan P, Zhang H, Yuan J, Liu J, et al. Performance improvement of a direct carbon solid oxide fuel cell system by combining with a Stirling cycle. Energy. 2017.

[100] Lahijani P, Zainal ZA, Mohammadi M, Mohamed AR. Conversion of the greenhouse gas CO2 to the fuel gas CO via the Boudouard reaction: A review. Renewable and Sustainable Energy Reviews. 2015;41:615-32.

[101] Zhong Y, Su C, Cai R, Tadé MO, Shao Z. Process Investigation of a Solid Carbon-Fueled Solid Oxide Fuel Cell Integrated with a CO2-Permeating Membrane and a Sintering-Resistant Reverse Boudouard Reaction Catalyst. Energy & Fuels. 2016;30:1841-8.

[102] Kopyscinski J, Habibi R, Mims CA, Hill JM. K2CO3-Catalyzed CO2 Gasification of Ash-Free Coal: Kinetic Study. Energy & Fuels. 2013;27:4875-83.

[103] Colpan CO, Hamdullahpur F, Dincer I, Yoo Y. Effect of gasification agent on the performance of solid oxide fuel cell and biomass gasification systems. International Journal of Hydrogen Energy. 2010;35:5001-9.

[104] Karimi A, Semagina N, Gray MR. Kinetics of catalytic steam gasification of bitumen coke. Fuel. 2011;90:1285-91.

[105] Umemoto S, Kajitani S, Hara S. Modeling of coal char gasification in coexistence of CO2 and H2O considering sharing of active sites. Fuel. 2013;103:14-21.

[106] Smith R J B, Loganathan M, Shantha MS. A review of the water gas shift reaction kinetics. International Journal of Chemical Reactor Engineering. 2010;8.

[107] Lehnert W, Meusinger J, Thom F. Modelling of gas transport phenomena in SOFC anodes. Journal of Power Sources. 2000;87:57-63.

[108] Ackmann T, de Haart LGJ, Lehnert W, Stolten D. Modeling of Mass and Heat Transport in Planar Substrate Type SOFCs. J Electrochem Soc. 2003;150:A783-A9.

[109] Janardhanan VM, Deutschmann O. CFD analysis of a solid oxide fuel cell with internal reforming: Coupled interactions of transport, heterogeneous catalysis and electrochemical processes. Journal of Power Sources. 2006;162:1192-202.

[110] Kong W, Zhu H, Fei Z, Lin Z. A modified dusty gas model in the form of a Fick's model for the prediction of multicomponent mass transport in a solid oxide fuel cell anode. Journal of Power Sources. 2012;206:171-8.

[111] Sanders MD, Zhu H, Kee RJ, O'Hayre RP. Model-based characterization of charged-defect transport and apparent gas-phase permeation in mixed-conducting perovskite membranes. Solid State Ionics. 2013;249–250:6-16.

[112] Suwanwarangkul R, Croiset E, Fowler MW, Douglas PL, Entchev E, Douglas MA. Performance comparison of Fick's, dusty-gas and Stefan–Maxwell models to predict the concentration overpotential of a SOFC anode. Journal of Power Sources. 2003;122:9-18.

[113] Todd B, Young JB. Thermodynamic and transport properties of gases for use in solid oxide fuel cell modelling. Journal of Power Sources. 2002;110:186-200.

[114] Chan SH, Khor KA, Xia ZT. A complete polarization model of a solid oxide fuel cell and its sensitivity to the change of cell component thickness. Journal of Power Sources. 2001;93:130-40.

[115] Shi Y, Cai N. A General Mechanistic Model of Solid Oxide Fuel Cells. Tsinghua Science & Technology. 2006;11:701-11.

[116] Shi Y, Cai N, Li C. Numerical modeling of an anode-supported SOFC button cell considering anodic surface diffusion. Journal of Power Sources. 2007;164:639-48.

[117] Shi Y, Cai N, Mao Z. Simulation of EIS spectra and polarization curves based on Ni/YSZ patterned anode elementary reaction models. International Journal of Hydrogen Energy. 2012;37:1037-43.

[118] Shi Y, Wang H, Cai N. Direct two-dimensional electrochemical impedance spectra simulation for solid oxide fuel cell. Journal of Power Sources. 2012;208:24-34.

[119] Adam A, Fraga ES, Brett DJL. Options for residential building services design using fuel cell based micro-CHP and the potential for heat integration. Applied Energy. 2015;138:685-94.

[120] Zhang H, Kong W, Dong F, Xu H, Chen B, Ni M. Application of cascading thermoelectric generator and cooler for waste heat recovery from solid oxide fuel cells. Energy Conversion and Management. 2017;148:1382-90.

[121] Zhang H, Xu H, Chen B, Dong F, Ni M. Two-stage thermoelectric generators for waste heat recovery from solid oxide fuel cells. Energy. 2017;132:280-8.

[122] Nakagawa N, Ishida M. Performance of an internal direct-oxidation carbon fuel cell and its evaluation by graphic exergy analysis. Industrial & Engineering Chemistry Research. 1988;27:1181-5.

[123] Lee AC, Mitchell RE, Gür TM. Thermodynamic analysis of gasification-driven direct carbon fuel cells. Journal of Power Sources. 2009;194:774-85.

[124] Li S, Lee AC, Mitchell RE, Gür TM. Direct carbon conversion in a helium fluidized bed fuel cell. Solid State Ionics. 2008;179:1549-52.

[125] Wu Y, Su C, Zhang C, Ran R, Shao Z. A new carbon fuel cell with high power output by integrating with in situ catalytic reverse Boudouard reaction. Electrochemistry Communications. 2009;11:1265-8.

[126] Tang Y, Liu J. Effect of anode and Boudouard reaction catalysts on the

performance of direct carbon solid oxide fuel cells. International Journal of Hydrogen Energy. 2010;35:11188-93.

[127] Li C, Shi Y, Cai N. Performance improvement of direct carbon fuel cell by introducing catalytic gasification process. Journal of Power Sources. 2010;195:4660-6.

[128] Cantero-Tubilla B, Xu C, Zondlo JW, Sabolsky K, Sabolsky EM. Investigation of anode configurations and fuel mixtures on the performance of direct carbon fuel cells (DCFCs). Journal of Power Sources. 2013;238:227-35.

[129] Jiao Y, Zhao J, An W, Zhang L, Sha Y, Yang G, et al. Structurally modified coal char as a fuel for solid oxide-based carbon fuel cells with improved performance. Journal of Power Sources. 2015;288:106-14.

[130] Ong KM, Ghoniem AF. Modeling of indirect carbon fuel cell systems with steam and dry gasification. Journal of Power Sources. 2016;313:51-64.

[131] Xu H, Chen B, Zhang H, Sun Q, Yang G, Ni M. Modeling of direct carbon solid oxide fuel cells with H2O and CO2 as gasification agents. International Journal of Hydrogen Energy. 2017;42:15641-51.

[132] Luo Y, Shi Y, Li W, Ni M, Cai N. Elementary reaction modeling and experimental characterization of solid oxide fuel-assisted steam electrolysis cells. International Journal of Hydrogen Energy. 2014;39:10359-73.

[133] Xu H, Chen B, Irvine J, Ni M. Modeling of CH4-assisted SOEC for H2O/CO2 co-electrolysis. International Journal of Hydrogen Energy. 2016;41:21839-49.

[134] Wu Y, Shi Y, Luo Y, Cai N. Elementary reaction modeling and experimental characterization of solid oxide direct carbon-assisted steam electrolysis cells. Solid State Ionics. 2016;295:78-89.

[135] Mon E, Amundson NR. Diffusion and Reaction in a Stagnant Boundary Layer about a Carbon Particle. 2. An Extension. Industrial & Engineering Chemistry Fundamentals. 1978;17:313-21.

[136] Luo Y, Shi Y, Li W, Cai N. Dynamic electro-thermal modeling of co-electrolysis of steam and carbon dioxide in a tubular solid oxide electrolysis cell. Energy. 2015.

[137] Eguchi K. Ceramic materials containing rare earth oxides for solid oxide fuel cell. J Alloy Compd. 1997;250:486-91.

[138] Xie Y, Cai W, Xiao J, Tang Y, Liu J, Liu M. Electrochemical gas-electricity cogeneration through direct carbon solid oxide fuel cells. Journal of Power Sources. 2015;277:1-8.

[139] Luo Y, Shi Y, Li W, Cai N. Comprehensive modeling of tubular solid oxide electrolysis cell for co-electrolysis of steam and carbon dioxide. Energy. 2014;70:420-34.

[140] Xu H, Chen B, Liu J, Ni M. Modeling of direct carbon solid oxide fuel cell for

CO and electricity cogeneration. Applied Energy. 2016;178:353-62.

[141] Huang Z, Zhang J, Zhao Y, Zhang H, Yue G, Suda T, et al. Kinetic studies of char gasification by steam and CO2 in the presence of H2 and CO. Fuel Processing Technology. 2010;91:843-7.

[142] Ni M. Modeling of SOFC running on partially pre-reformed gas mixture. International Journal of Hydrogen Energy. 2012;37:1731-45.

[143] Shi Y, Cai N, Li C, Bao C, Croiset E, Qian J, et al. Modeling of an anode-supported Ni–YSZ|Ni–ScSZ|ScSZ|LSM–ScSZ multiple layers SOFC cell: Part I. Experiments, model development and validation. Journal of Power Sources. 2007;172:235-45.

[144] Fan B, Yan J, Yan X. The ionic conductivity, thermal expansion behavior, and chemical compatibility of La0.54Sr0.44Co0.2Fe0.8O3-δ as SOFC cathode material. Solid State Sciences. 2011;13:1835-9.

[145] Tai LW, Nasrallah MM, Anderson HU, Sparlin DM, Sehlin SR. Structure and electrical properties of La1 − xSrxCo1 − yFeyO3. Part 2. The system La1 − xSrxCo0.2Fe0.8O3. Solid State Ionics. 1995;76:273-83.

[146] Kopyscinski J, Lam J, Mims CA, Hill JM. K2CO3 catalyzed steam gasification of ash-free coal. Studying the effect of temperature on carbon conversion and gas production rate using a drop-down reactor. Fuel. 2014;128:210-9.

[147] Xu H, Chen B, Zhang H, Kong W, Liang B, Ni M. The thermal effect in direct carbon solid oxide fuel cells. Applied Thermal Engineering. 2017;118:652-62.

[148] Eguchi K, Setoguchi T, Inoue T, Arai H. Electrical-Properties of Ceria-Based Oxides and Their Application to Solid Oxide Fuel-Cells. Solid State Ionics. 1992;52:165-72.